REVIEW ARTICLE

Free-electron-laser-based biophysical and biomedical instrumentation

G. S. Edwards[a)]
Physics Department and FEL Laboratory, Duke University, Durham, North Carolina 27708

R. H. Austin
Department of Physics, Princeton University, Princeton, New Jersey 08544

F. E. Carroll
Department of Radiology and Radiological Sciences, Vanderbilt University, Nashville, Tennessee 37232

M. L. Copeland
Department of Neurosurgery, Vanderbilt University, Nashville, Tennessee 37232

M. E. Couprie
Universite de Paris-Sud and Laboratoire pour l'Utilisation du Rayonnement Électromagnétique, 91 898 Orsay, France

W. E. Gabella
W. M. Keck FEL Laboratory, Vanderbilt University, Nashville, Tennessee 37212

R. F. Haglund
Department of Physics and Astronomy, Vanderbilt University, Nashville, Tennessee 37235

B. A. Hooper
Department of Biomedical Engineering, Duke University, Durham, North Carolina 27708

M. S. Hutson
Physics Department and FEL Laboratory, Duke University, Durham, North Carolina 27708

E. D. Jansen
Department of Biomedical Engineering, Vanderbilt University, Nashville, Tennessee 37232

K. M. Joos
Department of Ophthalmology and Visual Sciences, Vanderbilt University, Nashville, Tennessee 37232

D. P. Kiehart
Department of Biology, Duke University, Durham, North Carolina 27708

I. Lindau and J. Miao
Stanford Synchrotron Radiation Laboratory, Stanford Linear Accelerator Center, Stanford University, Stanford, California 94309

H. S. Pratisto
Department of Biomedical Engineering, Vanderbilt University, Nashville, Tennessee 37232

J. H. Shen
Department of Ophthalmology and Visual Sciences, Vanderbilt University, Nashville, Tennessee 37232

Y. Tokutake
Physics Department and FEL Laboratory, Duke University, Durham, North Carolina 27708

A. F. G. van der Meer
FELIX, FOM Institute for Plasma Physics, NL-3439 MN Nieuwegein, The Netherlands

A. Xie
Department of Physics, Oklahoma State University, Stillwater, Oklahoma 74078

(Received 15 October 2002; accepted 6 April 2003)

A survey of biophysical and biomedical applications of free-electron lasers (FELs) is presented. FELs are pulsed light sources, collectively operating from the microwave through the x-ray range. This accelerator-based technology spans gaps in wavelength, pulse structure, and optical power left by conventional sources. FELs are continuously tunable and can produce high-average and high-peak power. Collectively, FEL pulses range from quasicontinuous to subpicosecond, in some cases with complex superpulse structures. Any given FEL, however, has a more restricted set of operational parameters. FELs with high-peak and high-average power are enabling biophysical and biomedical investigations of infrared tissue ablation. A midinfrared FEL has been upgraded to meet the standards of a medical laser and is serving as a surgical tool in ophthalmology and human neurosurgery. The ultrashort pulses produced by infrared or ultraviolet FELs are useful for biophysical investigations, both one-color time-resolved spectroscopy and when coupled with other light sources, for two-color time-resolved spectroscopy. FELs are being used to drive soft ionization processes in mass spectrometry. Certain FELs have high repetition rates that are beneficial for some biophysical and biomedical applications, but confound research for other applications. Infrared FELs have been used as sources for inverse Compton scattering to produce a pulsed, tunable, monochromatic x-ray source for medical imaging and structural biology. FEL research and FEL applications research have allowed the specification of spin-off technologies. On the horizon is the next generation of FELs, which is aimed at producing ultrashort, tunable x rays by self-amplified spontaneous emission with potential applications in biology.
[DOI: 10.1063/1.1584078]

I. INTRODUCTION

A free-electron laser (FEL) is a free beam of relativistic electrons that passes through a periodic magnetic field that results in the stimulated emission of light.[1] As such, these accelerator-based devices convert the kinetic energy of the electrons into light. In contrast, the medium for conventional lasers is bound electrons and the accompanying atomic nuclei, which restrict laser performance in some ways. FELs can be quasicontinuous or have high-peak and in some cases high-average optical power. They can produce long optical pulses, produce pulses with durations as short as subpicoseconds, or have a complex superpulse structure. The determining factors that establish the detailed characteristics of the light emitted by a FEL include the electron beam energy and electron pulse structure as well as the magnetic field characteristics. FELs are continuously tunable and have successfully operated in the microwave, far infrared, midinfrared, visible, ultraviolet and x-ray ranges. There are several excellent reviews of FELs.[2]

There are many FELs worldwide located in relatively large research facilities, each typically providing thousands of hours of beam time. Leading centers for biomedical and biophysical FEL applications include the far-infrared facility at the University of California, Santa Barbara (UCSB), midinfrared facilities at Duke, Stanford, and Vanderbilt Universities, The Jefferson Laboratory, FELIX in The Netherlands, and laboratories in France and Japan, and ultraviolet facilities at Duke and the LURE laboratory in France. Progress continues in FEL physics, in particular, the pursuit of ultrashort pulsed x-ray FELs.

Multidisciplinary research teams have pioneered the early applications experiments, taking advantage of the unique light source capabilities. As they have proved successful, experimental techniques have migrated between the physical, biological, and biomedical sciences. Here we will review research accomplishments in the biophysical and biomedical sciences as well as comment on future prospects. Naturally there have been numerous investigations of FEL applications in the physical sciences,[3] but they fall outside of the scope of this review.

FELs are versatile light sources that allow pioneering applications research by tuning to wavelengths of choice with relative ease. Many FEL laboratories are centers of excellence for interdisciplinary research where scientific phenomena have been discovered and characterized. This new understanding has allowed the specification of novel, dedicated technology to exploit these phenomena to improve the human condition. The spin-off technology is less complex and resource demanding than FELs, but indeed is a consequence of FEL development and FEL-applications research.

II. TISSUE ABLATION WITH THE MARK-III FEL

The argon ion, excimer, and CO_2 lasers are in routine medical use.[4] The visible argon ion laser has the advantage that it can be transmitted through the structures of the eye and focused to coagulate (remodel) and thus treat tissue. However, visible lasers are not effective tools for tissue ablation, i.e., removing a targeted volume of tissue such that the surrounding tissue is biologically viable. In contrast, the ultraviolet (UV) excimer has the advantage that it can etch tissue with essentially no collateral damage. Consequently, the excimer is a very effective tool for reshaping the cornea to correct its optical properties, i.e., laser vision correction. Typically, the outer surface of the cornea, a cellular tissue, is partially cut and lifted to expose the interior stroma, an acellular tissue, which is laser etched. Concerns about the potential mutagenic effects of ultraviolet radiation, i.e., photochemical effects mediated by excited electronic states, have

[a]Author to whom correspondence should be addressed; electronic mail: edwards@fel.duke.edu

largely prevented medical applications of the UV to cellular tissues. The infrared spectrum is typified by vibrational transitions, with far less concern about photochemistry. The infrared CO_2 laser is used for surface treatments of some tissue types, where the ablated volume is surrounded by a zone of denatured and possibly charred tissue, useful for controlling bleeding. In these applications the collateral damage is acceptable since the overall tissue remains biologically viable. However, there are many potential medical applications where such a zone of collateral damage is unacceptable. Consequently, there has been great interest in the biomedical community to explore the ablative properties of infrared lasers[5] to see if they can mimic the clean cutting of the excimer.

The Mark-III FEL is a tunable, infrared source in the 2–10 μm range with high-peak and high-average power.[6] The Mark-III produces a superpulse: the ''micropulse'' is about a picosecond in duration and contains tens of microjoules; the ''macropulse'' is a train of tens of thousands of picosecond pulses with a duration of about 5 ms and delivers tens of millijoules; the repetition rate of the macropulse is up to 30 Hz.

A. Infrared wavelengths and thermodynamics

Tissue typically is about 75% water, which is strongly absorbed in the infrared. So strongly absorbed that transmission infrared spectroscopy is not a viable option for investigating tissue in its native state of hydration. However, attenuated total reflectance (ATR) is a near-field or evanescent wave technique ideal for strongly absorbing samples. The ATR sampling technique is particularly powerful when coupled with Fourier transform infrared (FTIR) spectroscopy. In practice, the hydrated tissue is placed on the surface of an infrared material with a relatively high refractive index. Broadband infrared light propagates in the material such that it reflects from the material/tissue interface under the condition of total internal reflection, i.e., the tissue is only exposed to the evanescent wave. Consequently, the highly absorbing sample is optically sampled in the near field and we gain all of the advantages of FTIR spectroscopy.[7]

Figure 1 presents a midinfrared spectrum of cornea, neural tissue, and dermis. To first order, the midinfrared measures the localized vibrational modes of tissue components. Thus these spectra are similar because the midinfrared is not particularly sensitive to higher structural organization. Consequently, the results summarized below can be generalized to many tissues. These spectra serve as guides for selecting FEL wavelengths for investigating tissue ablation as well as providing a biophysical foundation for interpreting the results.

A series of experimental investigations have demonstrated that targeting a midinfrared Mark-III FEL to wavelengths near 6.45 μm results in tissue ablation at a substantial ablation rate with minimal and at times undetectable collateral damage. The seminal study reported investigations of FEL ablation in ocular, neural, and dermal tissues and proposed a thermodynamic model to account for these experimental observations.[8] Wavelengths near 6.45 μm couple into the spectral wing of the bending mode of water centered

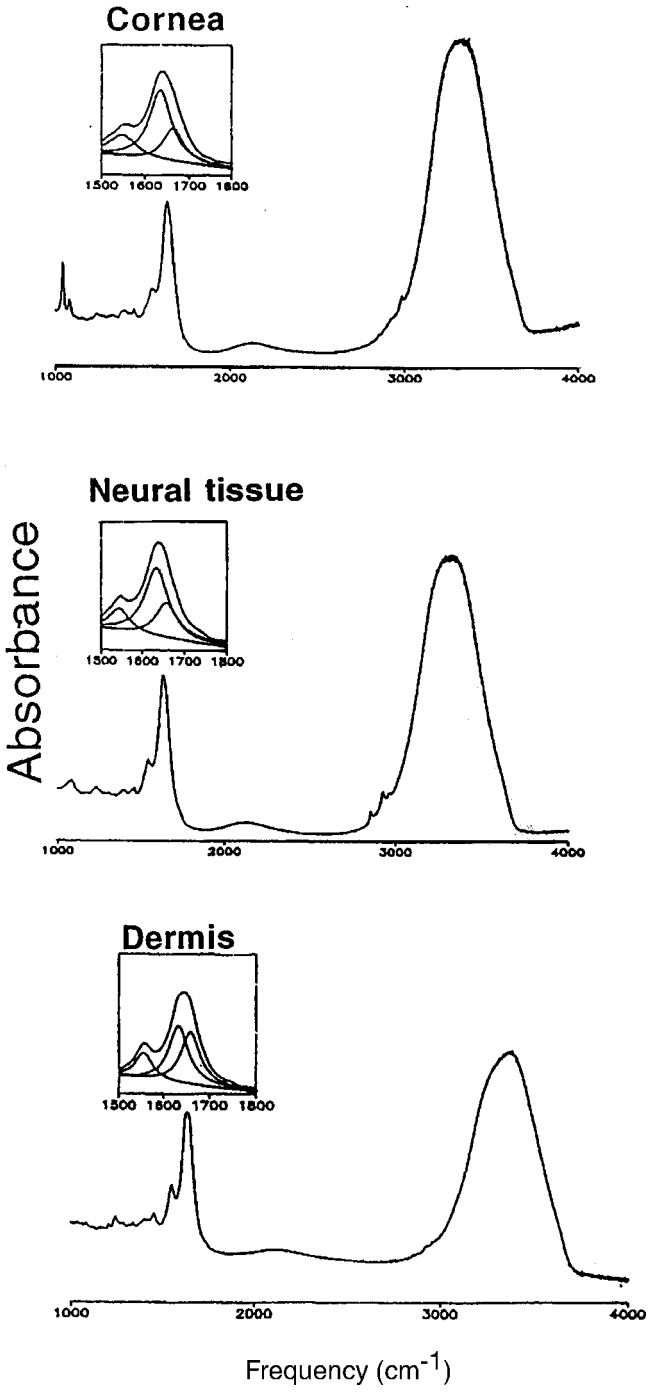

FIG. 1. ATR-FTIR spectra of cornea, neural tissue, and dermis in nearly native states of hydration. The dominant feature is the OH-stretch mode of water near 3300 cm^{-1} (3 μm). The partially resolved spectral band near 1650 cm^{-1} is deconvolved in the inset. Three modes are found to contribute: the amide I vibrational mode of protein at 1665 cm^{-1} (6.0 μm), the OH bending mode of water at 1640 cm^{-1}, and amide II vibrational mode of protein at 1550 (6.45 μm).

at 6.1 μm as well as the amide-II vibrational mode centered at 6.45 μm, both relatively broad spectral features. Thermodynamic reasoning suggested that the reduction in collateral damage is due to differential absorption; more specifically, tissue integrity is compromised due to laser heating of the nonaqueous components of tissue prior to explosive vaporization due to laser heating of the aqueous components.

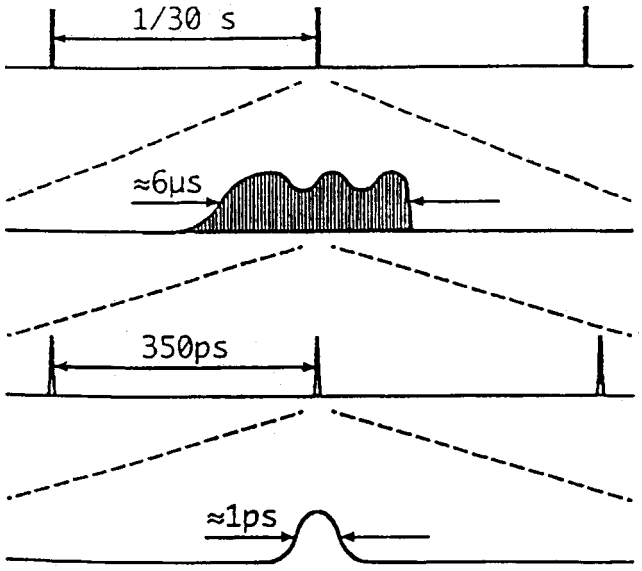

FIG. 2. Superpulse structure from a Mark-III FEL. From top to bottom, a train of three macropulses, a single macropulse, three micropulses, and a single micropulse.

These observations laid the groundwork to pursue human surgery with a Mark-III FEL.

Experiments that investigate the ablation of bone with the Mark-III FEL demonstrate that the 6.1–6.45 μm range is efficient in cutting cortical bone.[9] There is relatively little collateral damage and the healing response proceeds at a faster rate during the first two to four weeks compared to cutting with a bone saw. The investigators concluded that infrared ablation in bone is due to explosive vaporization and that ablation is enhanced by targeting the protein matrix of cortical bone via the overlapping amide I and amide II modes in the unresolved spectral band in the 6.1–6.45 μm range. Experiments that investigate the ablation of dental hard substances between 5 and 12 μm, including phosphate bands at 9.5 μm associated with hydroxyapatite, exhibit wavelength dependent surface modifications ranging from partial vitrification to surface roughening.[10] Additional investigations of Mark-III FEL ablation of other soft tissues and materials have been reported.[11]

B. Pulse structure and dynamics

While the thermodynamic model accounts for the wavelength dependence of infrared tissue ablation, it lacks details of the dynamics. The time constants of the Mark-III superpulse (Fig. 2) are 1 ps, 350 ps, 2–6 μs, and tens of ms and correspond to the micropulse duration, micropulse separation, macropulse duration, and macropulse repetition rate, respectively. In principle, these time constants correspond to multiple dynamic processes that need to be sorted out experimentally.

A full macropulse that delivers tens of millijoules drives multiple dynamic processes. In an effort to reduce the number of processes, a broadband infrared Pockel's cell was developed based on a CdTe crystal.[12] The Pockel's cell switches out a train of micropulses as short as 60 ns, delivering hundreds of microjoules, and as long as 2 ms, delivering 1 mJ, enabling pulse duration and wavelength dependent measurements of the FEL-induced stress transients and ablation plumes.[13] The back surface of a gelatin sample readily adheres to the surface of a 9 μm thick PVDF piezoelectric film that measures stress transients induced by FEL irradiation. The stress transients were measured with 500 MHz bandwidth electronics. For fluences below the ablation threshold, the superposition of asymmetric thermoelastic waves is detected. A continuous HeNe beam that is parallel to and 10 μm above the front surface of the gelatin is focused on a silicon photodiode with a 25 ns response time to monitor the ablation plume. For fluences above the ablation threshold, the superposition of an asymmetric thermoelastic wave with momentum recoil is detected. Furthermore, the wavelength dependence of the duration of the ablation plume indicates that 6.45 μm radiation compromises the mechanical properties of the gelatin, as do measurements of the particle size distribution in the ablated material.[14]

Dynamic light scattering has been used to monitor FEL-induced denaturation of cartilage and cornea.[15] The tissue samples are about 1 mm thick and initially in a state of nearly native hydration. Light of 600–700 nm passes through a sample from the back surface, such that the light is focused on the front surface. Nearly forward scattered light is collected with a photodiode array, where the capture rate was 1–4 Hz, while the front surface is radiated by the FEL. Nineteen wavelengths between 2.2 and 8.5 μm were investigated to determine the threshold energy and kinetic coefficients for denaturation. The signature for structural alteration is an increase in the distribution of visible light scattering. The minimum threshold was observed at 6.45 μm. For most FEL wavelengths, there is an inverse correlation between the denaturation threshold and the absorption coefficient. However, for wavelengths near 3 and 6 μm, the denaturation threshold does not obey this inverse correlation and instead is governed by heating kinetics.

Experimental attempts to ablate tissue with a kHz repetition rate, picosecond optical parametric amplifier (OPA), where peak intensities and total energy delivered were comparable to those typically used in Mark-III FEL tissue ablation, were unsuccessful.[16] Consequently, a detailed theoretical investigation of the role of nanosecond dynamics of thermal diffusion in infrared tissue ablation was carried out.[17] It was found that the temperatures of the surface layers of tissue water reached many hundreds of degrees in several nanoseconds: at this rate the outer saline layers become superheated and lead to explosive vaporization. During this time, the temperature of the surface layers of protein may either exceed or trail the water temperatures by tens to hundreds of degrees, depending upon the wavelength-dependent differential absorption of water and protein. At 6.45 μm the protein temperatures uniformly exceed the water temperatures and a Arrhenius treatment of protein dynamics indicates that ductile, native protein begins to convert into brittle, denatured protein. Apparently the brittle fracture at the onset of explosive vaporization leads to the confinement of collateral damage.

C. Future prospects

A key to the dynamics governing infrared tissue ablation is the differential heating rates for protein and saline. The dynamics are not established by the superpulse structure per se. Instead, the heating rates must be rapid enough to drive the separation in temperature between protein and water layers to achieve both protein denaturation and the superheating of water. This observation leads to reconsideration of the role of the Mark-III FEL superpulse structure in tissue ablation. In particular, theoretical calculations indicate that pulse duration of tens of nanoseconds with the same average energy as the superpulse should achieve similar ablative results.

Little is known about the polymer dynamics that lead to brittle fracture. In particular, what is the wavelength dependence for achieving mechanical confinement in addition to thermal confinement on such short length and time scales? It seems evident that linear and nonlinear pressure waves may play a role in the onset of nonthermal collateral damage. In addition, it has been proposed that the Mark-III FEL, for fluences below the ablative threshold, can operate as a stress wave generator.[18] Since the pressure waves alter membrane permeability, there may be drug delivery applications.

Within the macropulse, the Mark-III FEL is a GHz repetition rate picosecond laser with high-peak and high-average power.[19] This is the consequence of the pulse power system, including the long-pulse *S*-band klystron, the modulator, and the pulse-forming network.[20] FELs are light sources with unique capabilities that are typically complex and expensive. Relaxing the constraint from a GHz repetition rate, tunable infrared laser to a single wavelength, lower repetition rate, infrared laser with a pulse duration of tens of nanoseconds is technologically much more forgiving. This analysis suggests the feasibility of a nonaccelerator-based medical laser, with a pulse duration of 10 ns, operating near 6.45 μm.

III. MARK-III FEL AS A SURGICAL LASER

The Vanderbilt Mark-III FEL first lased in 1991 and initially served as a research tool for five years. The advent of human medical applications necessitated upgrading the Mark-III to meet the operational standards of a medical laser, which are quite different from the standards of a research laser. In 1996, a major effort commenced to upgrade this Mark-III FEL to the status of a medical laser for human surgery.[20]

A. Failure analysis

The types of failures for the FEL and its subsystems run the gamut from those that self-correct, like an arc in the klystron tube, to those that are nearly catastrophic and may require days to weeks to repair, e.g., vacuum leaks or the failure of high voltage components in the pulsed power subsystem. The failures fall into the following categories:

(1) major, planned shutdowns scheduled typically more than one month in advance and extending over more than a few days;
(2) routine maintenance, scheduled typically at least a week in advance and extending over a few hours;
(3) nonroutine maintenance that requires the FEL to be shut down for more than 1 h or so, but that can be scheduled at the beginning of the next running day;
(4) repair of minor, immediate failures that may require minutes to an hour;
(5) repair of medium size failures that may require a few hours to a day;
(6) repair of major failures that requires many days to weeks;
(7) self-correcting faults such as klystron arcs which interrupt the operation for seconds or minutes.

Obviously the impact on surgeons using the FEL depends on the category of failure. Interruptions of a few minutes have negligible impact for a surgeon performing a 3 h procedure, whereas catastrophic failure would disrupt patient care. Predictability is essential for human surgery. Predicting FEL performance one day into the future based on current behavior and accumulated diagnostics was one of the main goals of the reliability upgrades.

The reliability plan included (1) stocking spare parts, especially klystrons, (2) upgrading the control system for both better robustness and for more and better diagnostics, and (3) following sound engineering practices in the high-voltage, pulsed-power systems.

B. Subsystem upgrades

The klystron is a long pulse, 30 MW *S*-band microwave amplifier manufactured by Triton ETD. One such klystron had provided eight years of operation, but was beginning to show poor high-power performance. Klystrons have relatively high infant mortality and require several weeks to commission. Consequently at least one fully conditioned spare is now kept on hand. The modulator includes a 40 kV, 6 A dc power supply that charges up a bank of capacitors [pulse-forming network (PFN)] and switches the PFN across a transformer that drives an electron beam through the klystron. The environment of the modulator is quite inhospitable: there are high voltages with the resulting corona and ozone effects and the high voltage is switched quickly with a high-power thyratron, resulting in large electromagnetic interference throughout its cabinet and in adjacent equipment.

The most important upgrades to the modulator were power regulation using Sola ferromagnetic resonant power conditioners. Previously both the thyratron and the klystron filament power would vary during the day and need constant adjusting to maintain performance. For the thyratron, a nicely isolated, discrete box was custom built by Northstar Research, rebuilt by FEL Center personnel, and used to drive all the connections of the thyratron including the trigger pulse. The upgraded power regulation dramatically improved the operation of the modulator.

Other modifications can be characterized as sound engineering practices. Air cooling was increased to the cabinet that houses all the modulator components. The circulation, cooling, and filtering of the insulating oil was improved. This oil blackens over time, presumably due to corona and infrequent arcing: filtering the oil keeps it clean and a full oil change is done annually.

Another key step towards reaching the desired operational standards was addressing the technical limitations present throughout the building. For example, air conditioning the room that contains the modulator as well as other power supplies and electronics also turned out to be problematic. A system typically used as a computer room air conditioning system was installed. The system is highly redundant, which has proved invaluable when one of its components requires service. In addition, a special chilled water system for cooling the linear accelerator (linac) was installed. It was designed and built by Innoventor Engineering Inc. and replaced an aging passive system that was unable to maintain the linac temperature especially during the summer months. The design specifications met by the cooling system were that the linac would be maintained at ± 0.05 F while running the modulator and all the other systems on the cooling loop in steady state. It also keeps the temperature steady at ± 0.15 F during interruption of the modulator for as long as 2 min. It has a variable temperature setpoint of 75–105 F. It also can expel up to 80 kW of heat, although at our present operating maximum of 30 as opposed to 60 Hz it rarely expels more than 30 kW of heat. The system performs as designed and has led directly to better spectral stability and power stability in the FEL.

The original control system was based on two eight year old 8086-compatible STD-Bus PCs used to perform real-time data acquisition and control. EMIs from the nearby modulator periodically rebooted these computers due to noise on the backplane, attributed to aging connectors in the computers and to increased EMI from the modulator. These two 8086 computers were replaced with a dedicated Macintosh PowerPC connected over a general purpose interface bus (GPIB) network to several devices, one of which is an HP VXI-bus data conditioning and acquisition system. This directly improved operations and increased the amount and quality of the diagnostic information from the FEL subsystems. The program on the Macintosh was written and is maintained by center personnel and is the first, fastest software safety check of the subsystems. This Macintosh is networked to another Macintosh running LABVIEW, which is the operator interface to the control system.

The optics of the laser cavity and the laser beam transport system were upgraded. The output mirror of the cavity is a dielectric coated ZnSe mirror. There are five sets for different wavelength bands: 2–3, 2.8–4.2, 4–6, and 6–9 μm, as well as a special mirror with 15% transmission in two bands, at 2.8–3.2 and 5.8–6.8 μm. A three-mirror and later four-mirror carrousel replaced a single mirror mount in the laser cavity. Before the upgrade, mirrors were only changed once or twice a week because of the interruption to FEL operation and because of the radiation hazard in accessing the laser cavity midweek. With the four-mirror carrousel the full wavelength range can be scanned with only modest interruption to lasing while the new mirror is put into position and aligned.

It is necessary to keep the infrared beam transport system at rough vacuum pressures because several bands in the FEL wavelength range are highly attenuated in air. There are 7 mirrors between the laser cavity and the laser diagnostics room, and 14 mirrors between the cavity and the operating room. With so many mirrors even a few percent of scattering loss per mirror results in large loss of power from the laser. The beam transport system degrades slowly over time both from exposure to the FEL and from exposure to air or oil from the vacuum pumps. Mirrors are checked several times a year to determine if the losses at any given wavelength have increased. It is of interest that one mirror typically has been found to be the cause of the problem.

There were several important lessons learned during operation and maintenance of the Mark-III FEL. One is that running the FEL 72 h a week nearly every week, allowing some time Monday morning for routine maintenance and startup, is beneficial for two reasons. First, an operator or engineer likely will be monitoring the control system when problems develop, making identification of the problem easier and quicker. Second, there is a lot of time to investigate, at least via the computer diagnostics, intermittent problems and plan shutdowns for more invasive diagnostics at times that are least disruptive.

C. Results

These upgrades substantially improved the operation of the Mark-III FEL in general, and benefited both the medical and nonmedical user communities. The predictability exceeded 95% and serious failures have been limited to two weeks per year. As a consequence, this Mark-III FEL readily satisfies the requirements for investigational human surgery. Furthermore, the spectral and power stability of the Mark-III is greatly improved, as well as the ease of scanning the full range of infrared wavelengths.

IV. MEDICAL BEAM DELIVERY FOR THE MARK-III FEL

Establishing a stable, reliable, user-friendly delivery system at the W. M. Keck FEL Center at Vanderbilt University that transports the infrared beam from the FEL to the surgical suite approximately 90 m away is a challenging task. Standards established for medical laser technology need to be achieved to satisfy the strict requirements necessary for human surgery. Operating in the wavelength range beyond 2.5 μm requires unconventional beam delivery techniques due to the broad tunability of the FEL, the strong atmospheric absorption, high peak intensity of the micropulses, and long distance between the laser source and operating field. Alignment, pointing stability, reproducibility, and safety concerns of the beam transport system are addressed in the design.

A. Beam alignment

The laser cavity, electron accelerator, and power supply of the Mark-III FEL are located in the basement of the four-floor building.[20] The fourth floor houses a fully equipped surgical facility, which includes two operating rooms (ORs) (OR1 and OR2), patient preparation rooms, and a recovery ward. Due to atmospheric absorption, the beam transport system is evacuated and terminates in the OR. The beam is either matched to the entrance aperture of an articulated mirror arm using a two-lens telescope or it is refocused using a

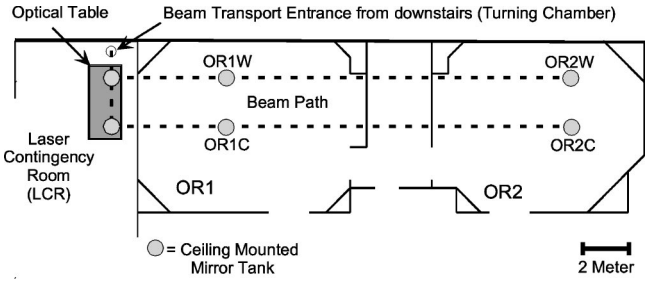

FIG. 3. Partial floor plan showing the beam path from the laser contingency room (LCR) to the operating rooms (OR1 and OR2).

single lens into a hollow waveguide based, handheld delivery probe. Figure 3 shows part of the surgical floor plan with the laser contingency room (LCR) and the two ORs. The laser parameters (spectrum, energy, repetition rate, and macro- and micropulse durations) are monitored on an optical table in the LCR where the beam path can be switched to either OR.

Each OR has two ceiling mounted beam ports (OR1C, OR1W, OR2C, and OR2W). Beam transport from the LCR to the ORs is achieved by directing the beam upward in the LCR onto a mirror at 45°, then horizontally (above the ceiling) to the OR. In the ceiling mounted mirror tanks, a 45° angled mirror reflects the beam downward into the OR to a reference point marked by a crosshair. The crosshair in the center of the optical beam path is monitored with a camera (mounted in the ceiling mirror tank) and displayed in the LCR. These crosshairs are the reference points for mounting the articulated mirror arm or launching into a waveguide or possibly a fiber device. The maximum energy per macropulse delivered to the beam ports is about 70 mJ and depends on the gain curve of the Mark-III FEL. Consequently, the average output power is up to 2 W. Mirrors with a diameter of 76 mm (3 in.) (protected silver coated Si, II-VI, Inc., Saxonburg, PA) are mounted in the turning chambers of the beam transport system and are equipped with motorized adjustment screws (8301-MRA picomotors, New Focus, Santa Clara, CA) under remote control (a 8732 picomotor multiaxis driver, New Focus, Santa Clara, CA). Part of the laser beam (~10%) is split off using a CaF_2 beamsplitter (ISP, Tarrytown, NY) and directed through a CaF_2 window out of the transport system and onto the optical table in the LCR and is used for diagnostic and alignment purposes. The output from two pyroelectric quadrant detectors (PQD-220, Molectron Detector, Inc., Portland, OR) is analyzed and used as feedback signals for the automated alignment system.

Figure 4 shows a simplified schematic of the system that delivers the FEL beam to any one of the four ports in the two ORs. The FEL beam enters the fourth floor on the left side. M0 and M1 are the main alignment mirrors used to guide the FEL beam to the ports near the wall (OR1W and OR2W). Mirror M1 can be moved out of the beam path by means of a vacuum feed-through lever (MDC Vacuum Products Corp., Hayward, CA), so that the FEL beam can pass to mirror M2. Mirrors M0 and M2 reflect and align the beam to the ports near the center of the ORs (OR1C and OR2C). Each of the ceiling mounted mirror tanks in the LCR contains two mirrors that direct the beam either to OR1 or OR2. The mirrors (OR1W, OR2W, OR1C, and OR2C) are drawn elliptically in Fig. 4 to represent the fact that the beam is reflected perpendicular to the plane of the page toward the ORs. A photograph of this system in the LCR is shown in Fig. 5.

The alignment procedure coaligns the infrared beam of the FEL with the visible beam of a HeNe laser, which is initially aligned to the beam ports in the ORs (Fig. 4). In brief, the alignment procedure consists of (1) aligning the HeNe beam to the crosshair in the OR; (2) aligning the two quad cells, QD1 and QD2 (PQD-220, Molectron Detector Inc., Portland, Oregon), to the split off part of the aiming beam such that the centroid of the HeNe beam hits the quad cell in the center; and (3) using mirrors M0 and M1 to align the FEL beam to the center of the quad cells.[21] A computer code was written in LABVIEW (National Instruments, Austin, TX) that uses the signals of the quadrant detectors as feed-

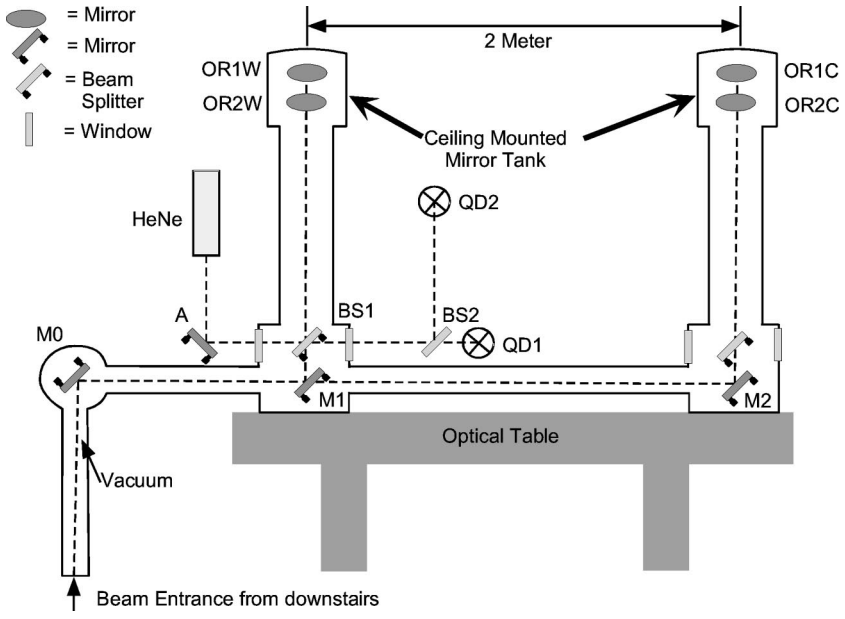

FIG. 4. Schematic of the beam switching and alignment system on the optical table in the laser contingency room.

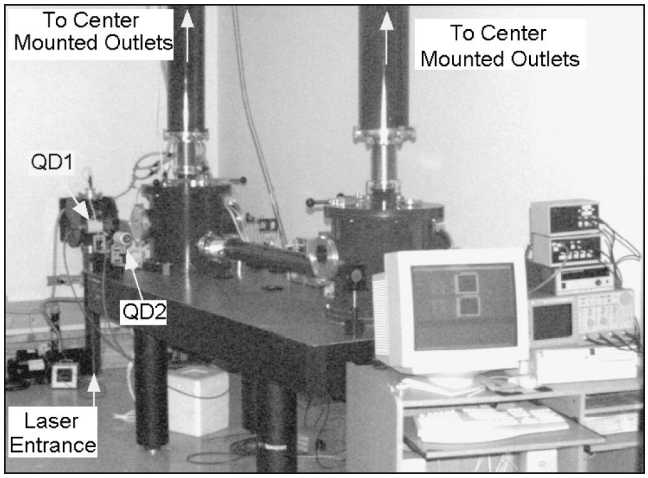

FIG. 5. Photograph of the laser contingency room showing the optical table with the capability for the beam switching and alignment. QD1 and QD2 are the quadrant detectors outside the evacuated beam transport system.

back to align the mirrors (M0 and M1), thereby controlling the picomotors on the mirror mounts as actuators. The algorithm aligns the FEL beam with M0 to the center of QD1 and that with M1 to the center of QD2 in an iterative loop. After the infrared FEL beam is aligned to the center of the beam port, beam splitter BS1 can be moved out of the beam path to maximize the power of the FEL to the OR. This is done by means of a vacuum feed-through lever. Considering the sensitivity of the quadrant detectors, parallelism of the windows and the beam splitters, accuracy of the mirror mounts and the piezoelectric screws, and proportional feedback control of the computer code, the current setup can coalign the HeNe beam and the infrared beam within a divergence of about 0.1 mrad, that is, the center of the beams can be displaced up to 2 mm over the 20 m path length between the LCR and furthest OR port.

In the ceiling mounted mirror tanks in the OR, a 45° angled mirror reflects the IR beam down into the OR where it transmits through a 10 cm diam, 1 cm thick BaF_2 window that serves as the final window in the evacuated transport system. The beam ports in each of the ORs are equipped with precision optic mounts to adjust the waveguide or fiber coupling device or the articulated mirror arm to its final optimal position. Figure 6 shows the delivery handheld probe and the articulated mirror arm connected to the ceiling mounted mirror tanks in the ORs, and gives a good overall impression of the actual design. The optomechanical mounts and a photodiode connected to a pulse counting unit are inside the white enclosure hanging from the ceiling. This enclosure is purged with nitrogen in order to avoid atmospheric losses. An additional nitrogen port is provided as a purge line for the surgical beam delivery device. The surgeon controls a shutter in the beam path by a foot switch (pedal). This shutter defaults to its closed position.

B. Beam stability

We investigated the stability of the delivery system over the 90 m path length; in particular, we were concerned about variations in temperature in the building. We measured the beam stability in the OR over the course of 1 h, at a time typical for a surgical procedure. The resolution for angular drift of the beam was 0.06 mrad, i.e., the beam drift was $<5\%$ of the beam diameter while the temporal energy output varied $\approx 5\%$. However, if the FEL needs to be retuned during a procedure, the infrared beam typically becomes misaligned and the transmission of energy can be unacceptably reduced. In this case, realignment with the current system can be accomplished within 5 min.

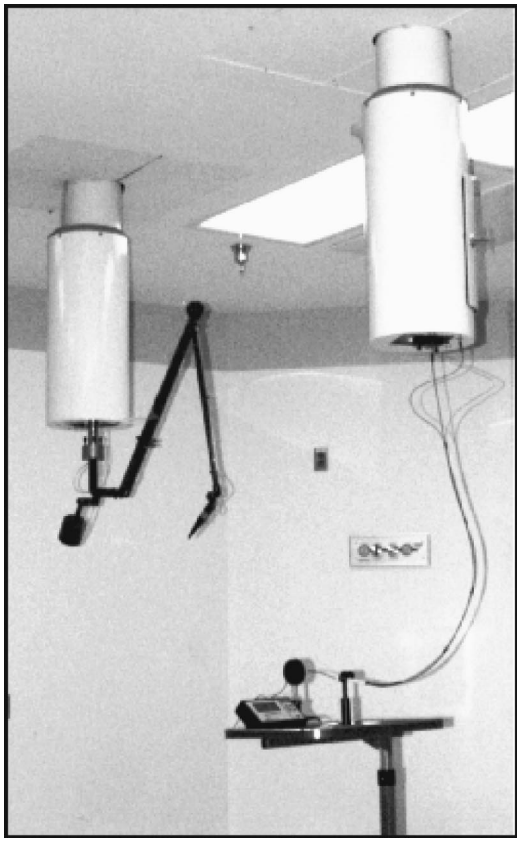

FIG. 6. Photograph of the two beam ports in OR2: The articulated mirror arm is mounted on the left and the handheld probe based on the hollow wave guide is mounted on the right.

C. Surgical delivery device

The final stage of the beam delivery system needs to be a flexible, maneuverable device that terminates in a handheld probe amenable to the surgeon to use as a precision surgical instrument. The key specifications for this device are flexibility, maneuverability, ruggedness, and ability to be sterilized. In addition, depending on the clinical application, as much as 30 mJ per macropulse needs to be delivered while focusing onto a spot size of 300 μm diameter. Due to wavelength range and peak irradiance constraints, fiber optic delivery is at the present time not feasible.[22] We have implemented two alternative strategies for surgical beam delivery. First, a modified articulated arm was outfitted with infrared mirrors and terminated with a focusing lens ($f=125$ mm). This proven technology gives six degrees of freedom, has relatively low losses, and is robust. We have delivered as much as 50 mJ/macropulse to tissue in a 300 μm spot size with this articulated arm. The major disadvantage is the mass

(even though it is counterweighted) and relatively large size. Nevertheless, this was the delivery system of choice for neurosurgery. As an alternative, delivery systems based on hollow waveguides (HWGs) have been developed.[23] The numerical aperture (NA) equivalent of the waveguide was measured to be 0.06 at $\lambda = 6.4\ \mu$m (which corresponds to an acceptance angle of 3.4°).[22,24–26] The final design of the probe[22,24] has a sealed tip, contains a CaF_2 microlens to focus the beam to a spot size of $\sim 200\ \mu$m, and has a working distance (focal length) of approximately 3 mm. The limitations of the HWG-based delivery device are significant losses ($>50\%$), variable losses depending on bending of the waveguide, and the potential of damage to the interior wall of the waveguide. Nevertheless, this device has been used in ophthalmic applications where delivery of only 3 mJ per macropulse was sufficient. Investigations of stretching of the micropulse duration due to transmission through a HWG are described elsewhere.[22,24]

D. Loss analysis

The total energy loss in the beam delivery system is the sum of the losses of the optical elements and in addition the absorption in the atmosphere for certain infrared wavelengths. There are seven mirrors located between the outcoupling mirror of the Mark-III FEL and the Laser Control room (located on the second floor). Four more mirrors direct the beam onto the optical table in the fourth floor LCR. Thus, M0 is the 11th mirror in the beam transport system. From there three more mirrors are used to direct the beam to any of the OR output ports. While single elements have low losses (typically 98%–99% reflectance, 92% transmission in a lens or window), the cumulative loss totals 30%–35% from the control room to the point of launching into the delivery device (hollow waveguide or articulated arm). The optical elements that contribute to this loss are seven mirrors, one BaF_2 window (the output window and the seal of the vacuum system), and one lens ($f = 300$ mm, in the case of the waveguide) or two lenses ($f = 300$ and 75 mm, in the case of the beam reducing telescope needed to couple to the articulated arm). In addition, the delivery device itself causes significant losses. Coupling losses for the hollow waveguide are 30%–40% and attenuation is 1dB/m, for a typical net loss of greater than 50%. In contrast, losses in the articulated arm due to the seven mirrors and the final focusing lens total approximately 20%.

E. Power stability

The macropulse energy of the Mark-III FEL is wavelength dependent, with a maximum at approximately 6 μm that falls off at wavelengths below 2.5 or above 8.5 μm.[6,20] The output near 6 μm often exceeds the requirement for human surgery, necessitating the capability for beam attenuation. A double Brewster plate polarizer made of ZnSe (PAZ30mm-AC, II-VI Inc., Saxonburg, PA) is installed inside the vacuum beam line, upstream of the first mirror (M0) in the LCR. This polarizer is mounted to a motorized rotational picomotor stage (8401, New Focus, Santa Clara, CA) and interfaced to a multistage controller (the 8732 picomotor multiaxis driver, New Focus, Santa Clara, CA), as are all the controls for the picomotor-driven mirrors. Since the FEL beam is linearly polarized, rotating the polarizer reduces the power delivered to the target (polarization extinction is 1:3000). The position of the polarizer was chosen such that it can be used regardless of the surgical output port that is selected and is in front of the final alignment in the LCR. Rotation of the polarizer results in negligible misalignment of 0.01 mrad.

F. Results

The design and implementation of the medical beam delivery system for the Keck FEL Center met the safety and performance standards required for human surgery. However, further improvements of the resolution and reproducibility of the alignment system will be necessary for clinical use on a regular basis.

V. NEUROSURGICAL APPLICATIONS OF THE MARK-III FEL

Previous investigations of neural tissues demonstrated the preferred ablation properties of the Mark-III FEL when tuned to wavelengths near 6.45 μm.[8] Survival studies of FEL incisions of canine brain tissue[27] as well as of survival rat and isolated rat brains[8] showed a marked reduction of collateral thermal injury using FEL wavelengths near 6.45 μm. In the case of brain tissue, the damage to adjacent tissue, or collateral thermal injury, measured by histology was approximately one cell width deep to the laser incision and typically undetectable on the sides of the incision. Because of the promise shown by this series of studies, a protocol was identified for human surgery which met with the approval of both the FDA's Investigational Device Exemption (IDE) and Vanderbilt's Investigational Review Board (IRB).

The protocol called specifically for the partial FEL excision of an extra-axial brain tumor.[28] In other words, a small external portion of a tumor would be laser excised, and then the rest of the tumor would be removed using traditional methods. Patients with an *extra-axial* tumor, or tumor that originated inside the skull but outside the brain, were chosen because no normal brain tissue would have to be traversed to have access to the tumor. In this way, the number of possible sources of brain injury for the procedure is reduced and thus interpretation of any poor neurologic outcomes postoperatively is greatly simplified. Extra-axial tumors, such as a specific type called meningiomas, also are characteristically nearly always benign. Therefore, long term survival of the patient is much more likely, should long term side effects become an issue. Finally, such tumors can usually be removed *en bloc*, or intact, so that the tissue adjacent to the ablative volume will likely be spared from being lost in the removal of the remaining tumor mass and can thus be studied histologically without having to fit pieces of a tumor puzzle together. While these tumors in general are ultimately not good candidates for laser resection because of their typical ease of resection with traditional nonlaser based methods, they proved to have many qualities that are desirable for an initial study.

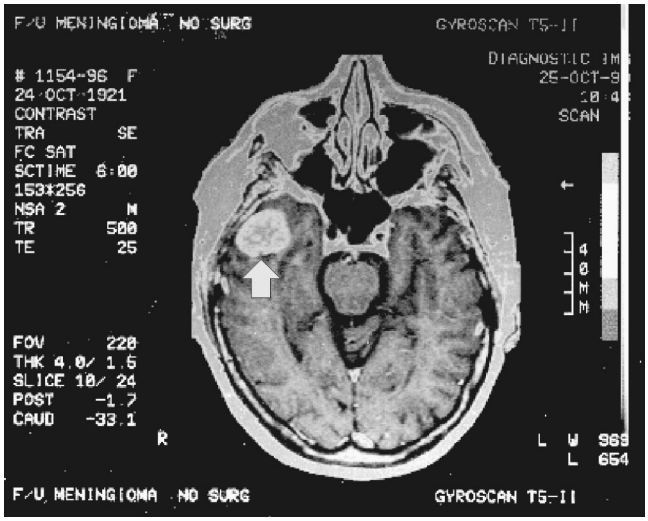

FIG. 7. Preoperative MRI scan (axial *T*1 weighting with gadolinium contrast). The arrow points to the tumor and its compression of the right temporal lobe.

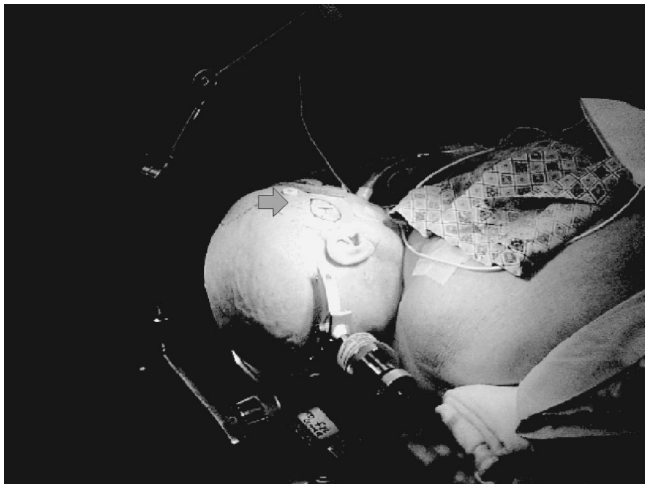

FIG. 8. Position of the patient prior to incision. The arrow shows location of the tumor (circled ''T'') based on data from the neuronavigational system.

A. Human neurosurgery

The first patient had a suspected meningioma of at least 3 cm in size, as shown in Fig. 7, and was neurologically stable prior to the procedure. The patient was operated on by an experienced neurosurgical team in Vanderbilt's Keck FEL Center. While this was the first human operation in this facility utilizing the Mark-III FEL, the facility had been performing both conventional laser and nonlaser human surgery (primarily orthopedic procedures) on a daily basis for several months prior to this operation. There are extraordinary needs for a neurosurgical operation of this complexity. It became clear early on in the design of these operating rooms that great care was required to minimize the likelihood of forgetting a seemingly insignificant device, medicine, supply, or part. Thus a track record was established of successful, routine cases using these operating rooms prior to the first FEL case.

The patient was brought to a holding area from the main hospital, where anesthesiologists prepared the patient for general anesthesia. The patient was prepped and brought into one of the two operating rooms fitted for use of the FEL. Once under anesthesia, the patient was positioned in a supine position with a shoulder roll under her right shoulder, thus allowing her head to be easily positioned nearly horizontally (Fig. 8).

A standard neurosurgical approach was used in the right temporal area, guided by a Pickar® neuronavigational system which utilized a computer topography (CT) scan that showed contrast obtained the day prior to the procedure. This system enables a computer in the operating room to show the location and position of our instruments with respect to the patient's anatomic features by viewing a computer monitor loaded with the preoperative CT images. This is accomplished using a system of infrared emitters on the patient and our instruments, and a series of infrared cameras within the room all of which feed back to the computer. Using a neuronavigational system thus allowed the creation of a comparatively small 6 cm curvilinear incision over the right temple to expose the skull over the tumor, rather than the typically large skin flap one uses just to ensure that the tumor is within the exposed area. A 5 cm bone flap was raised, exposing the underlying dura, which lines the inside of the skull. The tumor, attached to the deep, or brain side, of the dura, was easily located using the wand of the neuronavigational system. A 1 cm cuff of dura was cut around the border of the tumor and then folded back to expose the tumor. The surrounding normal brain was protected from any possible stray laser energy by moistened cottonoids (Fig. 9).

Once surgically exposed, about 1500 macropulses of 6.45 μm radiation averaging 32 mJ/macropulse were delivered through an articulated arm to the outer surface of the tumor. The articulated arm terminates in a hand piece, where a calcium fluoride lens with a focal length of 12.5 cm focused the FEL beam to a spot size of 310 ± 20 μm. A helium–neon pilot beam was used to guide the excision. By practicing one final time with some sterile paper on a side table, the surgeon was able to then position the hand piece with the visible pilot beam to keep the focus on the tumor surface, controlling FEL-beam delivery with a foot-pedal-actuated beam block. In the first operation, total FEL exposure administered in multiple passes took about 50 s, ablating approximately a cubic centimeter ''divot'' from the outer surface of the tumor. The remainder of the tumor was resected *en bloc* (Fig. 10).

Once removed, the tumor was divided and a portion of the tumor that did not include the defect was sent for neuro-

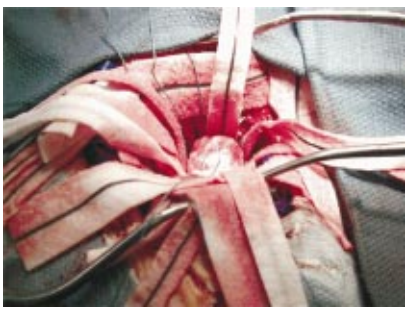

FIG. 9. (Color) Exposed tumor just prior to lasing.

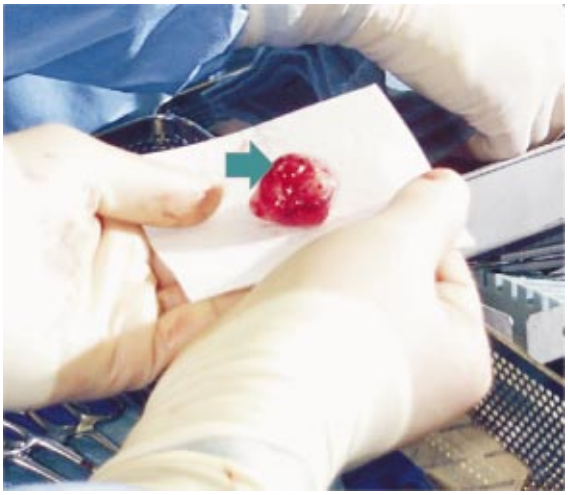

FIG. 10. (Color) Excised tumor. The arrow points to a vaporized defect.

pathologic examination to confirm the diagnosis. The remainder was processed, stained, and mounted on slides and inspected under the microscope. The width and depth of the divot were measured for each of the sections. The adjacent tissue was then inspected at a minimum of five locations and coagulation necrosis was measured at approximately the 4, 5:30, 6:30, and 8 o'clock position of the section (shown by black arrows, Fig. 11).

B. Postsurgical assessment

The laser performed extremely well and was indistinguishable from previous animal experiments. The tumor tissue was ablated quickly and effortlessly. The surgeon noted a significant subjective advantage of this type of resection with respect to effort and speed in comparison to other common methods of resection used for meningiomas, specifically ultrasonic aspiration, bovie loop resection, or mechanical removal with scalpel or forceps. Each macropulse ablated a portion of tumor approximately 0.5 mm wide and 0.07 mm deep and the articulated arm was easily and predictably controlled with the foot pedal. An estimate of the rate of ablation was approximately 1.8 mm^3 per second, depending on hand speed. There were no limitations in terms of angle of exposure of the laser to the tumor. There was no char. There was a smoke evacuation apparatus for safety, but no smoke was visualized. On one subsequent patient, the meningioma was clearly calcified preoperatively, as evidenced on a CT scan and by its texture at the time of surgery. The ablation rate was noted to be much slower in that case and calcific lesions may be more efficiently resected at another wavelength.

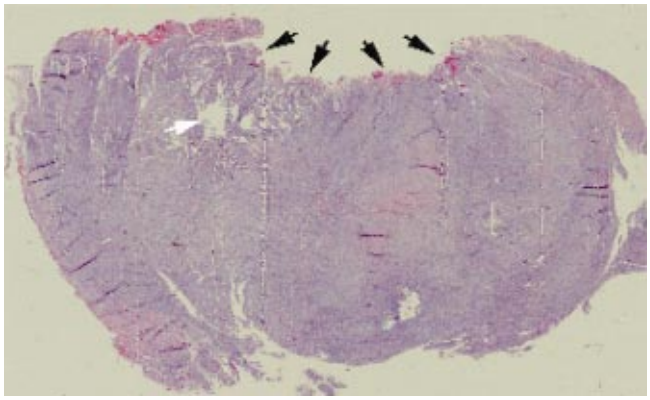

FIG. 11. (Color) 10 μm section of meningioma, stained with H&E. Ablated "divot" indicated by black arrows, at approximate sites for measuring possible coagulation necrosis. The white arrow points to the area of the tissue processing artifact.

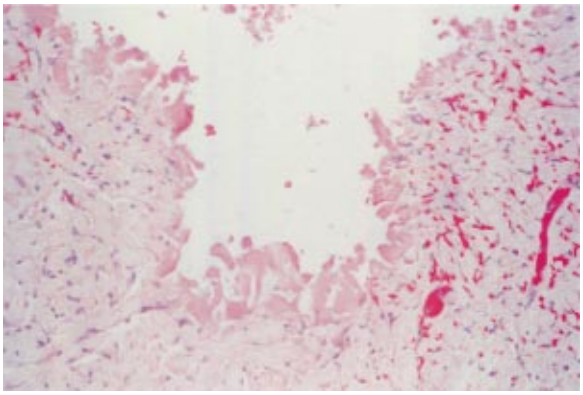

FIG. 12. (Color) Closeup of the 5:30 o'clock position in Fig. 5 (magnified 20×). Note the squared off appearance of what looks to be a divot due to a single pass of the FEL beam. Also note the presence of the intact nuclear morphology (small purple dots) near the edge of the divot, with cellular morphology lost only in cells adjacent to laser exposure that appears to be consistent more with cellular edema rather than with true coagulation necrosis traditionally found in collateral thermal injury.

The gross histologic examination of the slides (Figs. 11 and 12) showed remarkably sharp, square edges at the laser–tissue interface with minimal hemorrhagic deposition (showing as small magenta colored blobs) at the base and sides of the lesion. Adjacent tissue injury typically ranged from undetectable to one cell width and at no time was found to be greater than three cell widths. This finding is similar to results found in previous animal experiments in our labs. Unlike CO_2 laser lesions, there was no char on any of the sections.[29] There was also no discernable "pale zone" like that described around lesions made by other surgical lasers.[29] The presence of well defined nuclear morphology, typically lost in tissue coagulation necrosis from collateral thermal injury, is evident next to the very edge cells adjoining the divot throughout, suggesting that much of the adjacent tissue injury could be attributed to nonthermal processes. Coagulation necrosis, or heat damaged tissue next to the lesion, was judged as minimal to none. Other such processes could include mechanical injury due to the pulsed nature of the laser, simple perioperative tissue hemorrhage, as well as tissue processing artifact.

From a clinical standpoint, there were no complications from any of the first three patients involved in this study. The FEL has been shown previously not to have significant hemostatic properties,[27] however there was no significant hemorrhaging during laser ablation. The neuropathogy of each of the tumors resected was consistent with meningioma, as predicted by preoperative scan characteristics. Postoperatively, the patients woke up quickly and continued to have an exam that was unchanged neurologically. A postoperative magnetic resonance imaging (MRI) scan one week postop showed no residual tumor, nor any evidence of "punch through" of the

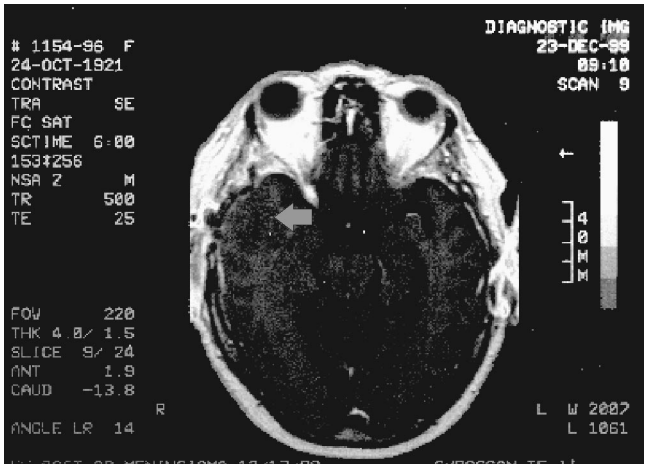

FIG. 13. One week postoperative MRI scan of the first patient (axial $T1$ weighting with gadolinium contrast). The arrow points to the previous location of the tumor. There is no abnormal enhancement and the temporal lobe has filled the tumor void.

laser (Fig. 13). Follow-up examinations found no clinical evidence of adjacent or distant brain injury from the procedure.

The first human application of a free-electron laser was safe and successful, with the initial results consistent with previous animal data. With respect to ease of use, efficacy of tumor resection, and minimization of collateral thermal injury, the FEL was judged to be superb in this neurosurgical application and compares very favorably to conventional surgical lasers. These findings support continuing clinical studies with the FEL and suggest that the FEL tuned to 6.45 μm has potential as a clinical surgical tool with significant advantages over conventional surgical lasers for use in the resection of certain tumors in the brain.

C. Future applications

Computer driven mirrors have already been well established both in science and industry to give very intricate control of lasers in making even very complex patterns, and with much more speed and accuracy than control by a human hand. Using a laser with such control and also the apparent accuracy for removing tissue demonstrated above, one could easily imagine an automated system for resecting tumors, such as that already being done with vision correction procedures.

While a surgeon would still likely need to provide exposure, or a pathway to the tumor, an image-guided resection certainly has the potential to be faster and more accurate. Several image guided systems have reported submillimetric accuracy, including the one used in this study to localize the tumor. Most would agree this compares very favorably with human knowledge and intuition-based navigation. What would be needed that does not yet exist in proper form is an accurate system of real-time image feedback, so that the system can be ''aware'' of what tissue has been resected and thus the anatomy of the changing target.

There are a number of ways one could envision introducing a feedback loop. A few medical centers already have intraoperative CT or MRI scanners constructed within their operating room facilities. A rescan would likely be time consuming, but accurate. Ultrasound has already been utilized for navigation systems and many tumors would likely be good candidates for that modality. Interpretation of the ultrasound information can be a bit fuzzy at times, however, since images can be less than crisp depending on the sound reflection qualities of the tissue. Attenuated total reflectance infrared spectroscopy also shows diagnostic potential for this task, and thus we may be able to use the infrared itself to help gather the information needed for reconstructing the changing environment.

While certainly much testing would be required, and a well-trained surgeon would be needed for both exposure and supervision of all such cases, the ease and speed of resection demonstrated by the Mark-III FEL in this study suggest that an automated system for resecting tumors is not only conceivable, but could likely be accomplished with existing technology within five years.

VI. OPHTHALMIC APPLICATIONS OF THE MARK-III FEL

A. Delivery system

Ophthalmic surgical procedures using the Mark-III FEL have been performed at the Keck FEL Center at Vanderbilt University. The infrared beam is transmitted under vacuum from the FEL vault to the surgical suite, where it is directed into a nitrogen-purged gantry. Then the FEL beam is focused into a hollow-glass waveguide to obtain a flexible delivery system in the surgical field (Fig. 14).[30] An adjustable diaphragm is placed in front of the focusing lens to regulate the transmission of the single-mode, Gaussian FEL beam. A 150 mm CaF_2 lens then focuses the beam into a 550 μm spot. The beam then passes through a 500 μm diam pinhole that protects the walls of the waveguide during alignment. The 530 μm inner diam waveguide is attached with a SMA connector and protected with Teflon tubing. The surgical handpiece ends in a 20 gauge thin-wall cannula. A CaF_2 lens with a focal length of 2 mm is placed at the tip of the cannula for final focusing and to protect the waveguide from moisture.

The hollow-glass waveguides are fabricated by a liquid-phase deposition technique that coats the inner surface with a silver film and then with a AgI film.[31] The thickness of the AgI coating will alter the wavelength optimization. Marcatili and Schmeltzer theoretically accounted for the low losses associated with these waveguides in 1964.[32] Bending losses for hollow-glass waveguides were calculated in 1990 by Miyagi and Karasawa[33] where the key dependencies of the attenuation coefficient α were

$$\alpha \propto \frac{\lambda^2}{a^3} \quad \text{and} \quad \alpha \propto \frac{1}{R}, \tag{1}$$

where a is the inner diameter and R is the bending radius. Thus there are losses with bending and a decrease in bore size.

For our surgical purposes, waveguides optimized for amide bands I, II, or III were selected and assembled into probes. At amide II (6.45 μm), losses were determined by measuring input and output energies through two different

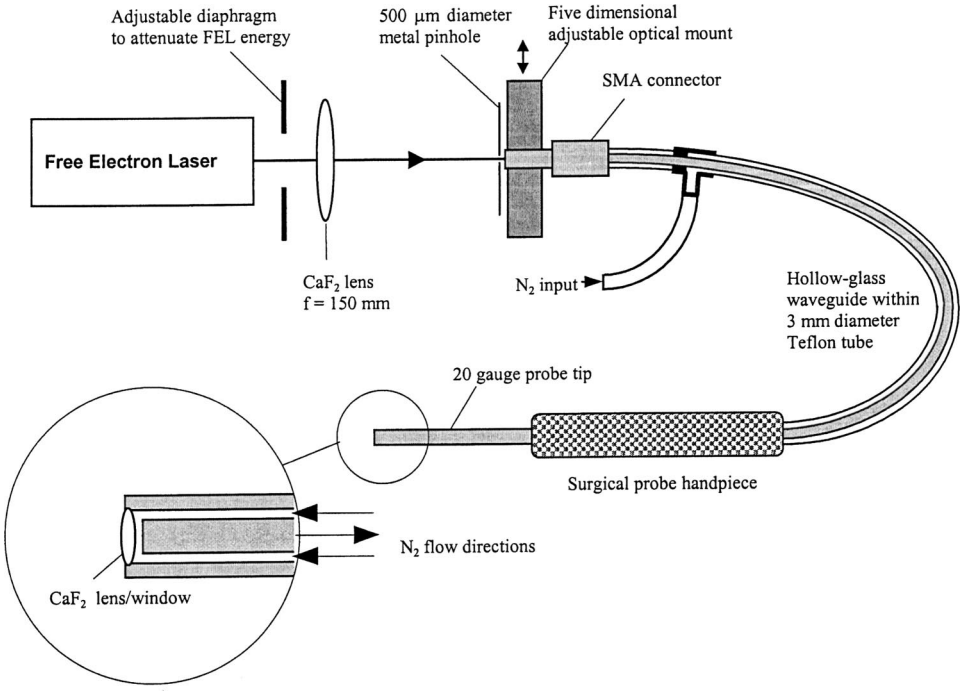

FIG. 14. Schematic of the FEL hollow-glass waveguide delivery system. The FEL beam passes through an adjustable diaphragm to attenuate the beam, and through a 150 mm focal length lens and a 500 μm diam pinhole to couple the beam to the hollow waveguide. The waveguide is within a surgical probe and is protected with a CaF_2 lens at the tip. (Reproduced with permission from the Optical Society of America; see Ref. 30.)

waveguide lengths, as well as by a 360° 25 cm radius curve. The coupling loss was 1 ± 0.3 dB ($20\pm5\%$), the transmission loss was 2.1 ± 0.15 dB/m (16.5%), and the loss in curvature was 0.7 ± 0.25 dB ($15\pm5\%$).[30]

A surgical probe was sterilized with ethylene oxide multiple times to permit sterile surgery on animals (Fig. 15) over a year without significant degradation. A waveguide probe delivering a 6.45 μm infrared beam with a fluence of 2.8 J/cm^2 and a spot size of 300 μm in diameter were used to ablate cadaver retina (Fig. 16).[30]

B. FEL optic nerve sheath fenestration

Optic nerve sheath fenestration has been successful in preventing vision loss in patients with pseudotumor cerebri.[34] This is a disease where abnormally elevated pressure of the cerebral spinal fluid surrounding the nerve compresses and damages the fibers. This procedure involves cutting a window in the thick coverings surrounding the nerve transmitting vision to the brain. It is technically challenging to expose and cut a window in the sheath to relieve pressure without damaging the underlying optic nerve. This waveguide system was used to perform optic nerve sheath fenestration in rabbits, promising a technically less challenging protocol.[35] Routine histological tissue data analysis showed that the 6.45 μm FEL beam at 10 Hz macropulse repetition rate and 2 mJ/macropulse were able to cut the optic nerve sheath without cutting the underlying nerve.[36]

Anesthetized rabbits received optic nerve sheath fenestrations with the FEL or with a knife. The conjunctiva was opened and the superior rectus muscle was disinserted. The

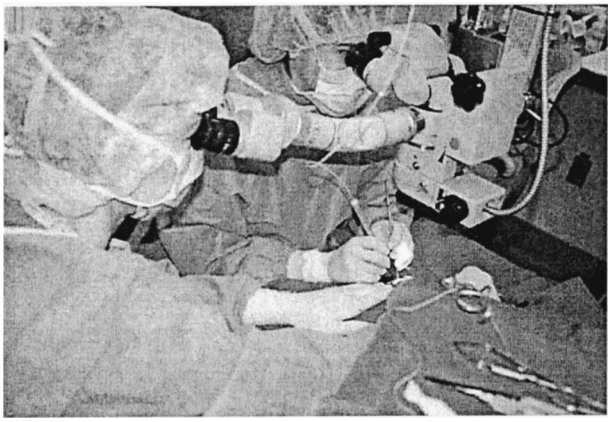

FIG. 15. Surgeons using a hollow-glass waveguide FEL surgical probe to perform an animal experiment. (Reproduced with permission from the Optical Society of America; see Ref. 30.)

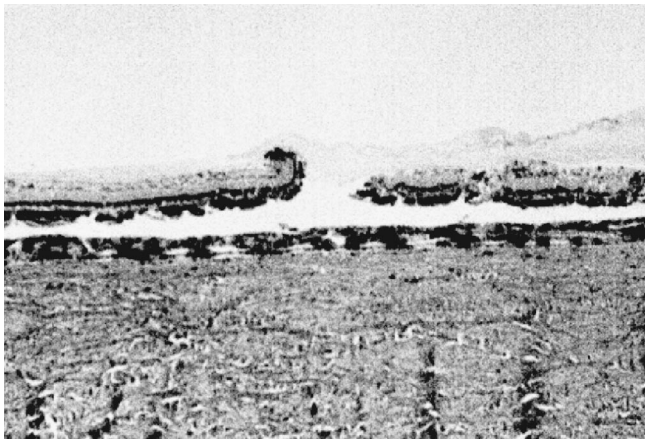

FIG. 16. Histologic results showing the ablated incision in the retina. No collateral damage was found. (Reproduced with permission from the Optical Society of America; see Ref. 30.)

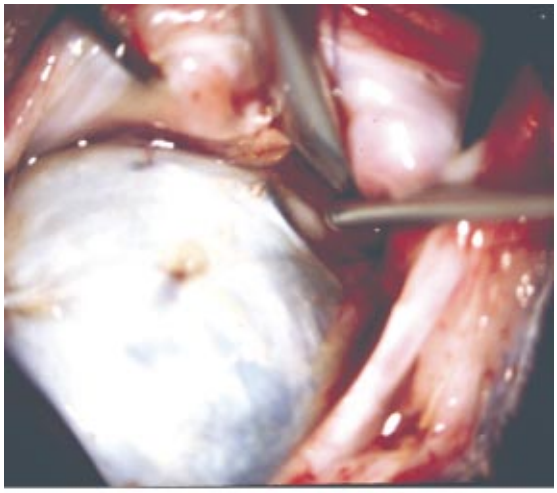

(a)

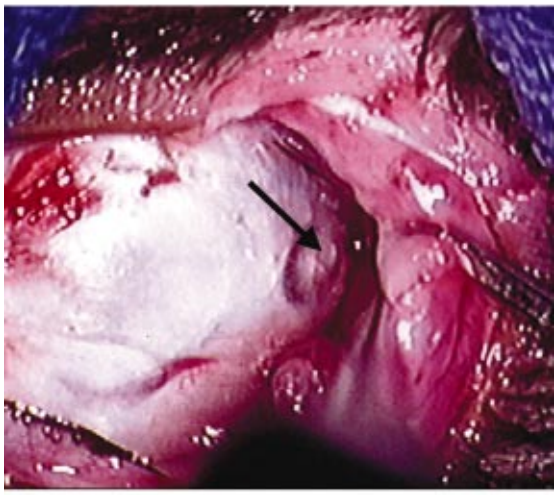

(b)

FIG. 17. (Color) (A) Sterile hollow waveguide probe that delivers FEL energy to the optic nerve sheath. (B) Window over the optic nerve is visible after removal of the incised sheath (shown by the arrow). (Reproduced with permission from Ref. 35.)

optic nerve could be observed with extensive retraction. A 2 mm diam window was produced by incising the optic nerve sheath either with a knife or with the FEL beam (6.45 μm, 10 Hz macropulse repetition rate, <2.5 mJ/macropulse, 300 μm spot size, 5 μs macropulse) using a 530 μm diam waveguide probe [Fig. 17(A)]. Then using a small hook we carefully removed the dura and arachnoid to create the fenestration window [Fig. 17(B)]. The superior rectus muscle and conjunctiva were repaired. The rabbits survived for one month or were sacrificed immediately following surgery with their optic nerves prepared for histologic analysis.[35]

Aiming the FEL probe was found to be technically easier and relatively efficient at cutting the circumference of the 2 mm diam circle in the small space between tissues compared to positioning the knife. One or on rare occasions two circular treatments with the FEL lasing an average of 2.0 mJ per macropulse were adequate to incise the dura.[35]

Both 6.45 μm FEL incisions at <2.5 mJ/macropulse and

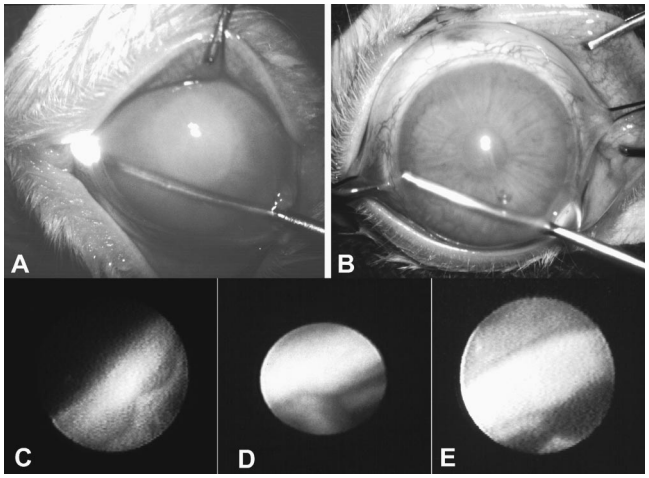

FIG. 18. (A) 0.8 mm diam endoscope coaxially coupled to a goniotomy needle placed in the anterior chamber. (B) 0.8 mm diam endoscope coaxially coupled to a 250 μm diam hollow waveguide for intraocular delivery of FEL energy placed in the anterior chamber. (C)–(E) Anterior chamber structures viewed through the endoscope since the corneas are extremely cloudy. (C) The needle tip is placed into the angle. (D) The laser probe is aimed at the trabecular beams. (E) An area of incised angle is visible. (Reproduced with permission from Ref. 38.)

knife incisions showed a lack of optic nerve damage with hematoxylin and eosin (H&E) staining. Near the fenestration site, glial fibrillary acidic protein (GFAP) (a histological marker of astrocyte activation) was increased within a few hours after incision with the FEL or the knife to demonstrate the sensitivity of these cells to manipulation. Hypertrophy of these glial cells was also evident after one month of healing equally in both treatment groups. Extensive nerve damage was observed when a macropulse energy of 7.5 mJ was applied to one nerve sheath, but optic nerve sheath fenestration appeared safe with macropulse energies less than 2.5 mJ.[35] Additional studies are ongoing.

C. Endoscopic FEL goniotomy

Goniotomy is a surgical treatment for infantile glaucoma. In goniotomy, a fine needle is inserted into the anterior chamber through a peripheral corneal incision to cut thickened trabecular beams to allow the iris to move posteriorly.[37] This may reduce intraocular pressure by decreasing the resistance to aqueous outflow. A 250 μm inner diam waveguide system was combined with a 0.8 mm diam ocular endoscope to perform FEL laser goniotomy and to compare to needle goniotomy in anesthetized congenital glaucoma rabbits.[38]

Goniotomy was performed with either the needle [Fig. 18(A)] or the FEL [Fig. 18(B)] at 6.45 μm, 30 Hz macropulse repetition rate, and 2.2–3.5 mJ/macropulse coupled to an endoscope. The rabbits' corneal edema prevented adequate visualization of the anterior chamber angle structures through the cornea [Figs. 18(A) and 18(B)].[38] The image of the angle was viewed on a video monitor [Figs. 18(C)–18(E)] as the angle was incised 100°–120°. Intraocular pressures were measured postoperatively. The animals survived three weeks and then underwent goniotomy on the contralat-

eral eye immediately prior to euthanasia. Both eyes were preserved for histologic evaluation.[38]

This FEL surgery successfully lowered the postoperative intraocular pressure for three weeks in the rabbits and was comparable histologically to endoscopic goniotomy performed with the needle. No collateral thermal damage was observed.[38]

D. Future prospects

The Mark-III FEL beam delivered through a hollow-glass waveguide has the potential for surgical applications in ophthalmology. It has been delivered successfully to small surgical targets in and around the eye. A clinical comparison trial of optic nerve sheath fenestration with the FEL or scissors on blind eyes prior to enucleation is ongoing. In order to become clinically useful and acceptable for surgical procedures, smaller more economical lasers that mimic the key operating characteristics of the Mark-III FEL must be developed.

VII. FEL BEAM DELIVERY VIA EVANESCENT WAVE COUPLING AT OPTIC–TISSUE INTERFACES

Historically, precise laser surgery has targeted wavelengths where the optical absorption in the tissue is high. For micron-scale surgical precision using normally incident laser pulses, high tissue absorption coefficients in the ultraviolet, below 220 nm,[39] and the infrared, near 2.94 μm,[40] are typically targeted with conventional lasers. However, micron-scale precision can be obtained using evanescent waves, even at wavelengths where optical absorption is weak. Using evanescent optical waves, laser energy can be confined to a layer less than one wavelength thick at the surface of high-refractive-index devices.[41,42] Optical energy outside of the device is present only within a few micrometers of the device's surface, rather than freely propagating as a laser ''beam'' into the tissue. The Mark-III FEL is ideal for achieving efficient ablation rates because of its wavelength tunability, short pulse duration, and high average power. For efficient ablation of tissue with minimal thermal damage, short pulse durations that achieve thermal confinement[43,44] on this micron scale is necessary. Each short laser pulse of sufficient incident energy removes a layer of thickness approximately δ and thermally denatures a layer of several times δ.[45] The optical penetration depth δ is important not only for determining the amount of tissue removed and the residual thermal damage, but also for choosing the optimal laser wavelength and pulse duration. For example, for a 1 μm depth of penetration the estimated ideal pulse has a duration of about 1 μs and an energy of at least tens of millijoules. A Mark-III FEL is well suited to these requirements. The pulse duration is variable over the desired range and the wavelength can be tuned through the midinfrared tissue absorption bands to study the deposition of energy, cavitation (vaporization of water), and tissue ablation arising from evanescent wave interactions.

Maxwell's wave equations can be applied to describe the evanescent optical fields in water (a good approximation for wet tissues) for all angles of incidence and polarizations at interfaces with rugged visible-infrared optical materials such as silica, sapphire, zinc sulfide, silicon, and germanium. Based on this analysis, the useful evanescent field depth is on the order of 0.1–2 μm.[42] Here in Sec. VI we will describe how evanescent optical waves are generated at optic–tissue interfaces, and how these evanescent waves can be used diagnostically to sense, monitor, and measure the tissue, and therapeutically to thermally injure or ablate the tissue.

A. Evanescent optical waves

Electromagnetic radiation is totally reflected from an interface defined by a high-refractive-index medium n_1 and a low-refractive-index medium $n_2 (n_1 > n_2)$ when the angle of incidence exceeds the critical angle. The critical angle θ_c for total internal reflection is defined by Snell's law, $\sin\theta_c = n_2/n_1$. The boundary conditions require that the electric field, and hence the energy, be present in a layer somewhat less than one wavelength thick on the n_2 side of the interface. The waves in this layer are called evanescent waves because they decay rapidly to zero away from the interface. The plane wave evanescent electric field amplitude in a transparent medium is given by[46]

$$E_e(x,y,t) = E_e \exp[i(k_x x - \omega t)]\exp(-\gamma k_y y), \tag{2}$$

where $\gamma = (n_1^2 \sin^2\theta_i - n_2^2)^{1/2}$, and k_y and k_x are the wave vectors in the planes perpendicular and parallel to the interface. Since the wave fronts or surfaces of constant phase (parallel to the yz plane) are perpendicular to the surfaces of constant amplitude (parallel to the xz plane), Eq. (2) is a inhomogeneous wave. The power (irradiance) is proportional to $E_e^2 \exp(-2\gamma k_y y)$. The penetration depth δ_e of the evanescent wave in a absorbing external medium is

$$\delta_e = 1/(2\gamma k_y) = \lambda/[4\pi(n_1^2 \sin^2\theta_i - \mathbf{n}_2^2)^{1/2}]. \tag{3}$$

The amplitude of the evanescent wave decays rapidly in the y direction and becomes negligible at a distance of only a few wavelengths of light. When the lower refractive index medium has absorption, the index n_2 is replaced by the magnitude of the complex refractive index, $|\mathbf{n}_2| = n_{2,r} - i n_{2,i}$, where $n_{2,i}$ is the absorption index and is defined as $n_{2,i} = \lambda\mu_a/4\pi$. This introduces the absorption coefficient of the external medium (e.g., tissue) into the solution of Eq. (2) and describes the loss of ''total'' internal reflection due to absorption within the evanescent wave. The reflectance at the optic–tissue interface $R_{\perp,\parallel}$ can be written according to Fresnel relations where $\perp$ and $\parallel$ are the polarizations perpendicular and parallel to the plane of incidence, respectively. The fraction of absorbed incident energy in water (mimicking wet tissue absorption in the infrared spectrum) is given by $(1 - R_{\perp,\parallel})$. The required incident energy is obtained by multiplying the latent heat of vaporization of water by the penetration depth δ_e and the laser beam area, and dividing by the absorbed fraction $[2500\ \mathrm{J/cm^3} \times \delta_e \times (\pi\omega_0^2)/2/1 - R_{\perp,\parallel}]$, and may be a factor of 8 less if the partial vaporization model holds for $E_v \approx 330\ \mathrm{J/cm^3}$.[44]

Figure 19 shows evanescent optical waves at an interface between sapphire and water. The leftmost part of each curve corresponds to the critical angle for that wavelength, for in-

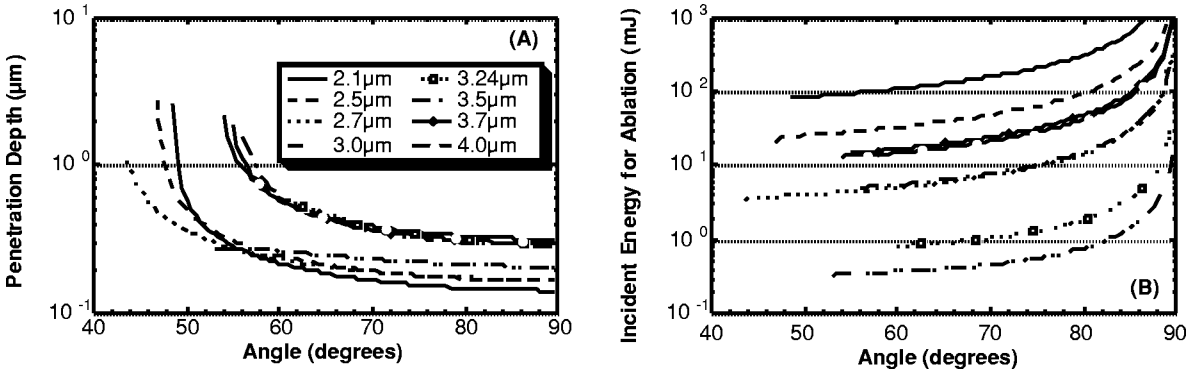

FIG. 19. Evanescent optical waves at an interface between sapphire and water. (A) The penetration depth of the evanescent wave and (B) the incident energy required for the vaporization of water by laser energy for perpendicular polarization as a function of the incident angle for wavelengths from 2 to 4 μm.

stance, $\theta_c \sim 48°$ at 2.1 μm. Note the variation in the order of magnitude in the evanescent wave's depth of penetration. The laser beam area calculation assumes a 500 μm Gaussian beam waist, ω_0. The input energy required to induce ablation in water at a sapphire–water interface using a 500 μm Gaussian beam waist is less than about 30 mJ for all wavelengths except 2.1 μm, where the input energy required is roughly 100 mJ. These are modest energy per pulse requirements for a Mark-III FEL. The practicality of evanescent-wave-driven tissue ablation is apparent from this analysis. Evanescent wave ablation occurs at modest power densities ($\sim 10^5$ W/cm^2), well below the threshold for optical breakdown ($\sim 10^9$ W/cm^2).[42]

Figure 20 shows tissue ablation using normally incident (0°) and evanescent (65°) optical waves at a sapphire–porcine aorta interface with Mark-III FEL light at a wavelength of 3.24 μm ($\perp$ polarization). The images are toluidine blue-stained histology sections [bar=100 μm in Fig. 20(B) and bar=20 μm, ablation to the left of the arrow in Fig. 20(B)]. The image in Fig. 20(A) shows an ablation depth of about 500 μm, and that in Fig. 20(B) shows an ablation depth of about 4 μm. Also visible are the black elastic layers and the smooth gray muscle cell layers that underlie the endothelial cells at the surface.

Evanescent waves have long been used in ATR spectroscopy in the infrared (IR),[47] in which the evanescent wave field is used to measure absorption spectra at surfaces in contact with high-refractive-index crystals. Evanescent waves at the boundary of fiber optics have also been used for spectroscopy and diagnostic applications.[48] Now suppose that we design a catheter that launches evanescent waves for both diagnostic and therapeutic procedures. The same catheter can deliver low level diagnostic light, say, from FTIR, and therapeutic light from an IR FEL, for instance.

Our preliminary work on the spectral signatures of different tissues in the IR shows promise for diagnostic imaging. Figure 21(A) shows IR reflectance spectra R of porcine aorta and fat tissue taken with an ATR cell from 2–10 μm. Note the differences in the spectra near 3.4, 5.7, and 8.5 μm. These spectra give a nice qualitative picture of tissue differences as a function of the wavelength. In order to model the therapeutic interaction of the evanescent wave at the interface, though, it would be much better if we had quantitative data for the optical properties of the tissue, for instance, the complex refractive index $\mathbf{n}_2$. This can be done by taking the reflectance data set R from the ATR FTIR, input it into a Kramers–Kronig algorithm to obtain the phase, and compare the Fresnel reflection at the interface to calculate $n_{2,r}$ and $n_{2,i}$ parts of the complex refractive index $\mathbf{n}_2$.[49] Figures 21(B) and 21(C) show our calculation of the complex refractive index of the tissues from Fig. 21(A). This now allows more precise modeling of the light–tissue interaction at these optic–tissue interfaces.

It is also possible to launch an optical probe beam at the interface to sense and monitor the dynamics of a tissue ablation process.[50] This probe is capable of measuring the en-

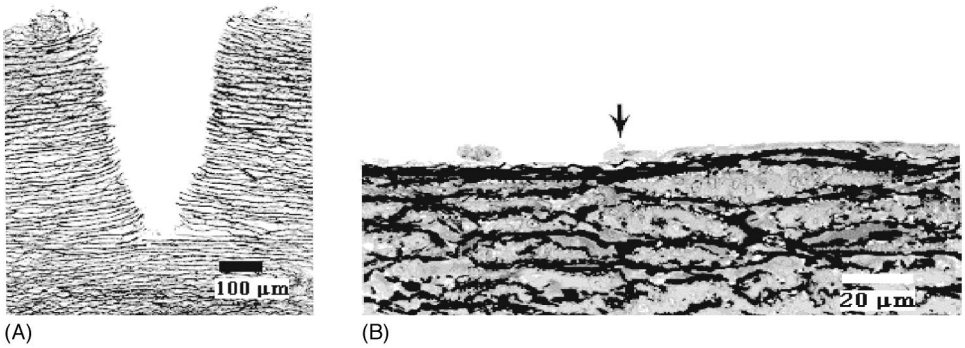

FIG. 20. Tissue ablation using (A) normal incident (0°) and (B) evanscent (65°) optical waves at a sapphire–porcine aorta interface with FEL light at a wavelength of 3.24 μm with perpendicular polarization.

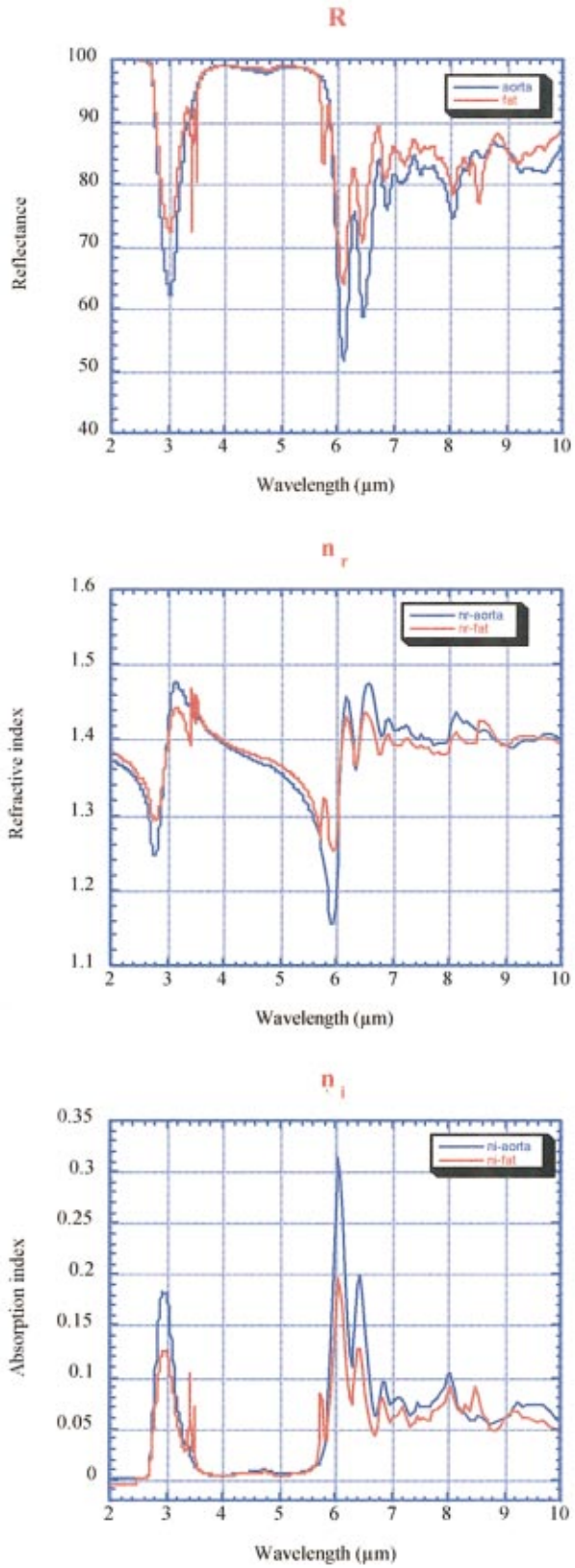

FIG. 21. (Color) (A) IR reflectance spectra of porcine aorta and fat from 2 to 10 μm. Note the differences in the spectra near 3.4, 5.7, and 8.5 μm. The calculated (B) real and (C) imaginary parts of the complex refractive index $\mathbf{n}_2$.

ergy deposition at a dielectric–tissue interface. The transient rise in temperature of the laser-heated layer at the interface can be measured using this calibrated probe and the onset of ablation can also be detected.

B. Future prospects

We are presently investigating the uses of these evanescent optical waves for applications in cardiology, neurosurgery, and laparoscopy. The IR catheter we are developing would allow spectroscopic feedback at the time of surgery to better determine the margin between healthy and diseased tissue. In cardiology, identification and modification of atherosclerotic plaque using IR evanescent light delivered through a catheter[51] may allow selective ablation of plaque at the unique wavelengths of fatty tissue absorption shown in Fig. 21. Preliminary data for neural tissue hold promise for identification of brain tumors, and the precise, controlled delivery of evanescent waves for ablation may allow better resection of these tumors with less damage to the surrounding healthy neural tissue. The ability to dissect through the fatty tissue surrounding many of the organs of the abdomen without transecting the blood vessels would be a major advance in laparoscopy. The unique spectral signatures of these fatty tissues in the IR may make controlled, selective ablation of fatty tissue in the brain, blood vessels, abdomen, and spinal cord possible.

In contact geometry, for instance, an optic–tissue interface, evanescent waves have a unique capability in diagnosis and therapy, where precision and control of light is important. Laser-generated evanescent waves can achieve extremely precise superficial ablation of tissue. Compared with normal-incidence exposure, the depth of ablation is limited by the evanescent wave penetration depth, independent of the number of laser pulses, and can be orders of magnitude less than the normal-incidence ablation depth. The practical implication is that high-precision, endoscopic laser surgical devices can now be realized, with the added advantage of control of the laser energy. Unlike free-beam laser surgery, only tissue in contact with the optical interface of an evanescent wave device is ablated, thereby allowing safe infrared beam delivery in the operating room. These tools may allow the diagnosis (spectroscopy) and therapy (ablation) to be performed in one catheter.

VIII. MICROBEAM TO INVESTIGATE TISSUE DYNAMICS

The application of molecular genetic strategies has resulted in major advances in developmental biology, in particular, our understanding of how specific genes influence the patterned movement of tissue.[52] Nevertheless, these extraordinarily powerful strategies fall short when probes for cellular function need to be applied with high spatial (diffraction limited) and temporal ($\ll$s) resolution. Laser microbeams[53] have been used to surgically investigate the forces responsible for morphogenesis[54,55] as well as to locally activate gene expression.[56] An infrared, near-field microscope that combines spectroscopic and imaging capabilities has been used to investigate biological tissue as well as subcellular structures at the superconducting accelerator (SCA) FEL facility at Stanford.[57] Here we describe methods that optimize beam delivery to thick biological specimens while monitoring tissue response at high spatial and temporal resolution.

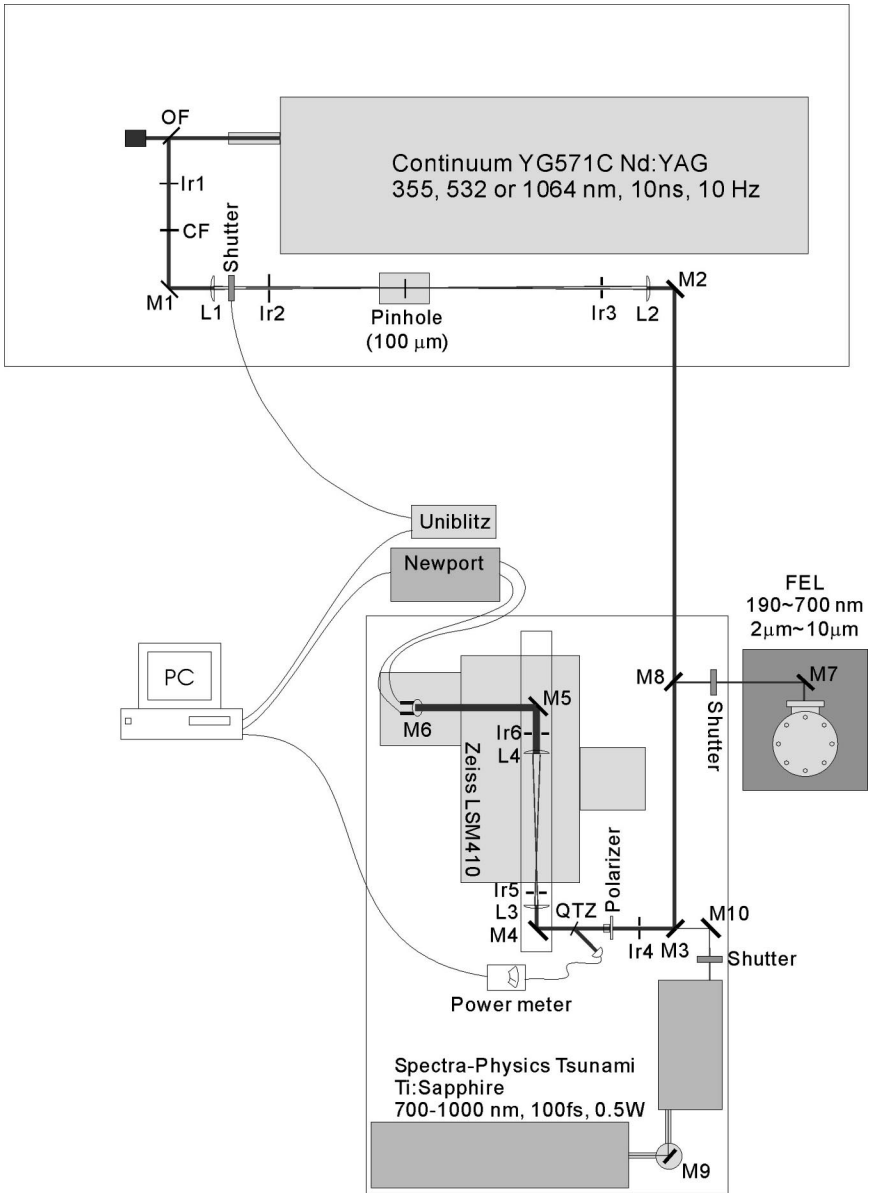

FIG. 22. Optical layout of the laser microbeam facility. OF—optical flat, M—mirror, L—lens, Ir—iris, QTZ—quartz flat.

We have developed a laser-based microbeam to investigate tissue dynamics *in vivo* at the Duke FEL Laboratory. The system has been planned to accommodate numerous light sources, including the UV OK-4 FEL and the infrared Mark-III FEL as well as commercial laser systems. The microbeam can be used to perturb the tissue, cells, and their constituent biological molecules while monitoring in real time with confocal microscopy. High-resolution imaging is achieved with laser confocal microscopy to visualize green fluorescent protein (GFP) labeling of the cytoskeleton in transgenic animals.

A. Microbeam

The microbeam is shown schematically in Fig. 22, where the perturbing beam can be the IR or UV FEL, a *Q*-switched Nd:YAG laser system (Continuum YG571, 10 ns pulsewidth, 10 Hz) or a mode-locked Ti:sapphire laser system (Spectra-Physics Tsunamai, 100 fs pulse width at 80 MHz). In the near future the Nd:YAG will be replaced with the more compact Continuum MiniLite II. The layout of the confocal microscope is shown in Fig. 22 as well as in Fig. 23, which considers the optical path of the perturbing beam within the microscope. Much of the early research has concentrated on making precise, user-defined incisions of fruit flies in early stages of development.[55] For this, the commercial Nd:YAG laser system allows progress in biological/biophysical research while at the same time highlighting technical issues that can be generalized to FEL microbeams.

To minimize the spot size of the biological specimen, each perturbing beam must be of high optical quality when it enters the rear aperture of the imaging objective. In the following, we describe the optical system used with either the second (532 nm) or third (355 nm) harmonics of the Nd:YAG laser system. The first stage of the optical train filters unwanted wavelengths from the ablating beam and provides fixed attenuation of the power. The beam first reflects from a fused silica optical flat (Janos Technology

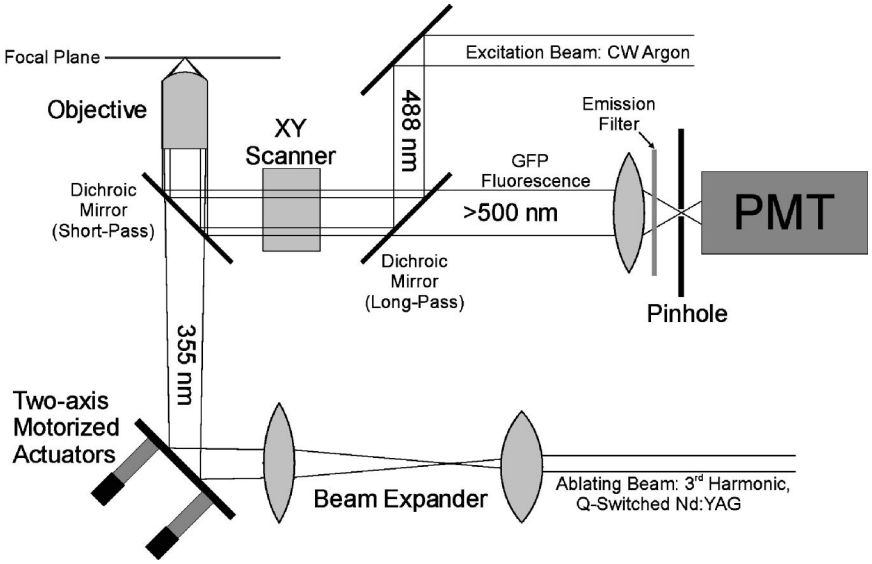

FIG. 23. Schematic diagram of the microscope's interior showing how the internal excitation beam and the external ablating beam are combined with a dichroic mirror to simultaneously direct both onto the sample. Note that the ablating beam diverges slightly to compensate for longitudinal chromatic aberration of the microscope objective in the UV. A second dichroic mirror is used to separate sample fluorescence from light scattered by the excitation and ablating beams. The fluorescence is then focused through a pinhole (conjugate to the objective's focal plane) before impinging upon a photomultiplier for detection.

A1805-358) 45° in the plane of the optical table. The second harmonic is *s* polarized and the third harmonic is *p* polarized with respect to this optical flat. Thus the second harmonic is attenuated to ~1/20 and the third harmonic to ~1/100 of the incident power. The beam then passes through a colored glass band pass filter (for 532 nm the Newport FSR-UG11, for 355 nm, Thermo Oriel No. 51970) that cuts out any residual light from the fundamental and unwanted harmonics of the laser. For operation at 532 nm, the beam is then reflected from a second optical flat, providing total attenuation to ~1/400 of the incident power. For operation at 355 nm, the optical flat is replaced with a dichroic mirror optimized for reflection at 355 nm (CVI PAUV-PM-1037-C) to eliminate further attenuation at this wavelength.

The remainder of the optical train is used for either 532 or 355 nm light. The ablating beam is passed through a spatial filter to clean up the mode content. The spatial filter consists of two convex lenses (each with a focal length of 75.7 cm for 532 nm light, CVI PLCX-25.4-360.6-UV) and a 100 μm pinhole. We chose these long focal length lenses to minimize the power density at the focus and thus avoid damage to the pinhole. The pinhole is held in a positioning mount (Melles Griot 07HPI501) on a small optical rail to minimize the time required to reoptimize transmission through the spatial filter when changing wavelengths. The size of the pinhole was chosen so it would pass only the center fringe of the incident beam at the focus of the first lens. The second lens is used to recollimate the beam. This setup provides a Gaussian beam profile at both 532 and 355 nm.

To this point, the optical train has provided gross attenuation of power and cleaned up the mode structure of the beam. The beam is then transmitted to the optical table on which the microscope rests for fine tuning. As discussed above, the output of the Nd:YAG laser is polarized. We use a calcite polarizer (Newport 10GL08) mounted on a rotation stage (Newport RSP-1T) to provide continuously varying attenuation of the ablating beam. Immediately after the polarizer, a glass coverslip is used to redirect a fraction of the ablating beam to an energy meter for online monitoring of the energy per pulse. For the final conditioning stage, the ablating beam is then passed through a pair of lenses, $f_1 = 20.0$ cm (Newport SPX028) and $f_2 = 27.0$ cm (CVI PLCX-25.4-128.8-UV), on an optical rail. This pair of lenses is designed to expand the ablating beam to fill the back aperture of the microscope objective and to provide fine control of the divergence properties of the beam. The ablating beam is now ready to be introduced into the microscope with precise user control over its four critical parameters: power, spatial mode, beam diameter, and divergence. It turns out that some divergence is necessary to compensate for the wavelength dependence of the refractive index of the microscope objective.

We bring the ablating beam in through the Keller port of the Zeiss axiovert microscope of the 410 confocal system. To allow simultaneous imaging and laser ablation, the first surface mirror that is mounted in the fluorescent filter slider is replaced with a short pass dichroic mirror without loss of image intensity. The ablating beam passes through the dichroic mirror and becomes coaxial with the scanning laser beam (argon, 488 nm) of the confocal system. Both beams are then transmitted through the objective and onto the sample. Different sets of dichroic mirrors are used to optimize the confocal fluorescent imaging performance while ablating at either the second or third harmonic of the Nd:YAG laser.

Two elements of the optical train are under computer control: a fast shutter (UNIBLITZ US25S2ZM0) just prior to the spatial filter and the actuators (Newport CMA-12PP) on the mirror underneath the microscope that steers the ablating beam towards the objective. Custom programs have been

written as Java plugins to IMAGEJ [National Institute of Health (NIH)] and executed on a PC. The shutter is controlled through an RS-232 connection to a UNIBLITZ D122 driver. In a similar way, the mirror actuators are controlled through a second RS-232 connection to a Newport controller (ESP300-11N11N). The shutter is used to control sample exposure to a defined number of pulses from the ablating laser. The mirror actuators are used to scan the ablating beam in the two dimensions of the plane of focus.

We use confocal fluorescence microscopy to observe fruit fly embryos during laser microsurgery. The argon laser, which is internal to the microscope housing, is focused onto the sample, exciting a cone of GFP molecules both above and below the focal plane of the objective. Fluorescence from these molecules is collected by the objective and separated from scattered excitation light with a long-pass dichroic mirror. The fluorescence collected is then focused through a pinhole that is conjugate to the focal point of the objective. This configuration largely rejects fluorescence from regions of the sample outside the focal plane. To build an image, the detector signal from the photomultiplier is compiled as the excitation source is raster scanned.[58]

At the beginning of each set of experiments, the alignment of the ablating beam is carefully checked with a rhodamine B dye in an agarose gel. The confocal microscope is first adjusted to image the bottom surface of the gel. Then with the ablating beam blocked from the entrance to the microscope, the spatial filter is optimized and the polarizer set to pass ~ 200 nJ per pulse to the sample. While imaging the surface of the gel, the shutter is transiently opened to allow single shots from the ablating beam to reach the sample. The lesions produced in the agarose gel are used to position the ablating beam in the center of the image plane. The divergence of the ablating beam at the rear aperture of the microscope objective is then finely adjusted through the separation of the final two lenses in order to minimize the lesion size observed. As shown in Fig. 24, our ability to measure the absolute size of the lesion in soft biological tissues is limited because such tissues retract from the margins of the ablated spot. However, the lesions may be as small as 0.5 μm in diameter when a metal film is targeted.

Once the ablating beam has been optimized, we can begin a set of experiments. Typically one fly embryo is used to finely adjust the energy per pulse in the ablating beam so that it is just above the single-pulse ablation threshold. For a typical experiment, we then take a single confocal fluorescent image of a fly embryo and open this image in IMAGEJ.[59] The user then begins taking a time-lapse series of images of the embryo and selects the desired cutting trajectory on the embryo in IMAGEJ. On command, the system will then move the two mirror actuators in order to position the ablating beam focus in the image plane at the start of the user-defined cut, open the shutter, move the ablating beam along the user-defined trajectory, and close the shutter when complete. The tasks of imaging and directing the ablating beam are controlled by two separate PCs. An example of real-time confocal imaging during laser microsurgery of a fruit fly embryo is shown in Fig. 24(C).

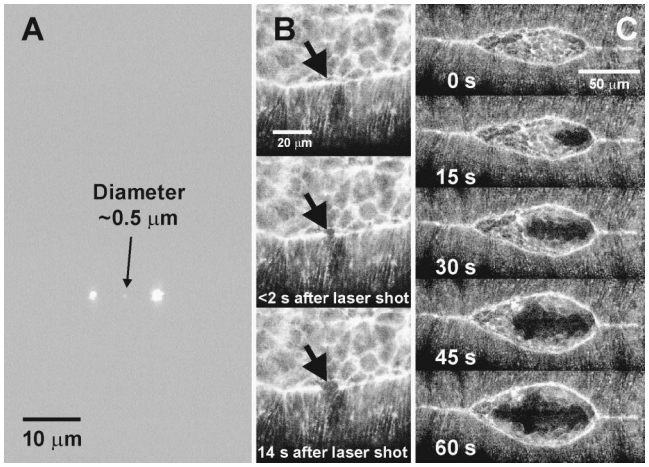

FIG. 24. Examples of laser microsurgery using the third harmonic (355 nm) of a *Q*-switched Nd:YAG laser. (A) By selecting a per pulse energy that lies just above threshold, the ablating microbeam can create lesions as small as 0.5 μm in diameter on solid samples like a metal film. Larger energies result in larger lesions. (B) A single pulse is delivered to the boundary between tissues in a living fruit fly embryo. The three panels are a time-lapse progression of confocal fluorescent images from before the laser pulse, <2 s after the pulse, and 14 s after the pulse. Within 2 s the lesion has expanded to a diameter of ~ 2 μm. It continues to expand for tens of seconds following the laser pulse. (C) The ablating beam is steered so it cuts a linear incision (~ 75 μm in length) across the entire width of an embryonic tissue known as the amnioserosa. The panels are a time-lapse series of images collected during this incision. The amnioserosa tissue retracts strongly as it is cut.

B. Future prospects

We will need to have similar control of the power, spatial mode, beam diameter, and divergence when adapting the microbeam system to either FEL source. Since we are already using UV optics for the third harmonic of the Nd:YAG, only small adjustments will be needed to use the OK-4 FEL as the ablating beam. Many more significant modifications will be necessary to adapt the microbeam apparatus to take advantage of the preferential ablative properties of infrared radiation.[8] We can simply replace the lenses and calcite polarizer with similar IR-transparent optics. However, special care must be taken in the selection of microscope objectives. We could compensate for the chromatic aberrations in the objectives over the small wavelength ranges involved in the tripled Nd:YAG microbeam apparatus. To match the focal planes for a visible imaging system and an IR ablating beam we will need to use a reflective Cassegrain objective on the microscope, which has already been tested in our laboratory. With these modifications, the laser microbeam apparatus can be extended to take advantage of available FEL sources.

IX. MARK-III FEL APPLICATIONS IN MASS SPECTROMETRY

Mass spectrometry (MS) is an indispensable analytical tool in biological, environmental, medical and polymer sciences and technology because of its high mass resolution ($\sim 10^{-4}$), wide mass range (up to 10^6 Da), and efficiency.[60] A major challenge in MS is developing ''soft'' ionization techniques that leave large, thermally labile analyte molecules intact. Two competing complementary ''soft ioniza-

tion'' techniques are widely used in MS, electrospray ionization (ESI)[61] and matrix-assisted laser desorption ionization (MALDI).[62] In MALDI, the analyte is encapsulated at low concentration in a matrix that absorbs laser light. As the matrix is ablated, the analyte molecules are entrained in the plume of ablated material, cooled by free-jet-like expansion and also, to some extent, shielded from collisions until ionization occurs.

The Mark-III FEL—with its combination of high intensity, high pulse repetition frequency, tunability, and ultrashort pulse duration—offers two significant opportunities for exploring and improving the soft ionization process. First, any spectroscopic effect, such as ion yield Y, is proportional to the energy E deposited per unit volume V:

$$Y \propto (E/V) \cong F_{\text{laser}} \alpha(\omega, I)_{\text{matrix}}, \tag{4}$$

where F is the laser fluence, α is the absorption coefficient, and ω and I are, respectively, the laser frequency and intensity. Since many matrix materials have rich vibrational spectra in the midinfrared, the local density of vibrational excitation and the ability to initiate specific processes, such as ionization, can be varied according to the wavelength and intensity. Second, the ionization *rate* scales with the intensity, rather than the fluence

$$\frac{dN^+}{dt} = \eta \cdot N_0 \sigma_{(k)} (I/\hbar\omega)^k, \tag{5}$$

where N^+ is the number of ions, η is the quantum efficiency (which can be taken to include all ion loss processes, such as collisional neutralization), $\sigma_{(k)}$ is the kth-order cross section for ionization, and I is the laser intensity. Thus in principle, the ionization rates associated with ns-laser-induced desorption and ionization *should be* lower than those for ps or fs pulses; whether or not this is true in a practical laser ionization source for MALDI MS remains to be demonstrated conclusively; early FEL MALDI-MS studies showed clear evidence of intensity, rather than fluence, dependence;[63] but more recent experiments reveal a more complex picture.[64]

A. Reflectron time-of-flight mass spectrometry with the FEL

The Vanderbilt University FEL has been used to demonstrate soft ablation and ionization of proteins with masses up to 66 kDa from a variety of matrix crystals,[65] so work has now been expanded to include such biologically relevant matrices as water and gels, *without* adding any exogenous matrix materials. The Vanderbilt FEL has 1 ps micropulses spaced 350 ps apart in a macropulse lasting up to 4 μs, with an average power of up to 3 W.[6] Individual macropulses from the free-electron laser are routed through a broad-band Pockel's cell[12] to slice out a shorter segment that ranges from 100 to 400 ns, typically containing 50–300 μJ in a few hundred to a thousand micropulses; the pulse energy is adjusted by crossed polarizers. The laser spot size at the surface of the MALDI target, measured with a reticle under an optical microscope, is typically 2×10^{-4} cm^2, producing micropulse intensities of $10^9-6\times10^9$ W/cm^2. Laser energies are measured directly in front of the final focusing lens (BaF_2, EFL = 10.6 cm) using a Molectron J25-110 energy meter and an EPM1000 controller. The readings are then corrected for the measured transmission of the lens and ZnSe window of the vacuum chamber to arrive at the total energy deposited in the target.

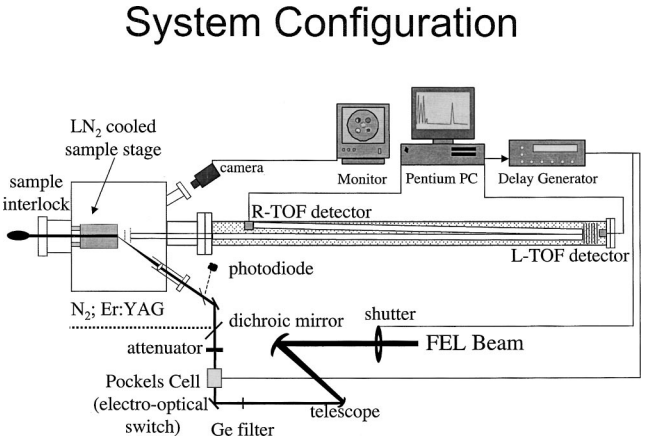

FIG. 25. Schematic of the reflectron time-of-flight mass spectrometer experiment located at the Vanderbilt W. M. Keck Free-Electron Laser Center. The ion source is located in a large cubical vacuum chamber; different sample holders, equipped, for example, with cryocooling or movable microtiter plates, are mounted by interchanging the rear access plate of the vacuum chamber. The FEL beam transport system, including the electro-optic switch, as well as other lasers (Er:YAG, N_2, KrF/ArF, and Nd:YAG) can be used interchangeably to provide laser ablation and ionization of the samples.

Mass spectra are acquired with a custom-built, laboratory-modified 3 m reflectron time-of-flight mass spectrometer[66] (Comstock, Oak Ridge, TN), equipped with delayed extraction, a dual-chevron microchannel plate (MCP) detector (Galileo Electro-Optics), and either a 96-well movable microtiter plate stage or a cryogenic sample stage maintained near liquid nitrogen temperatures. In the cryostage, the probe is slightly off the ion-optical axis of the mass spectrometer, so that one can ablate multiple spots on the target by rotating the probe. The temperature of the stage is monitored by a resistive thermal device attached to the front of the cryostage by thermally conducting epoxy. Voltage of 5 kV is applied 300 ns after laser irradiation to accelerate ions generated in the evolving ablation plume; focusing is achieved by an Einzel lens near the front end of the flight tube. At the end of the ToF tube, ions are accelerated to 4 kV just in front of the MCP. Ion signals are detected by a 500 MHz data acquisition card (Signatec DA 500A) and processed by custom software based on LABWINDOWS CVI. The apparatus is shown in Fig. 25.

A recent experiment showed the utility of the FEL in desorbing and ionizing small proteins directly from a polyacrylamide gel of the type used in electrophoresis separations. Angiotensin II (1160 Da) and bovine insulin (5637 Da) were dissolved in de-ionized water (high pressure liquid chromatography grade) containing 0.1% trifluoroacetic acid at concentrations of 5 and 3 mM, respectively; equal parts (v:v) of the two analyte solutions were then combined. A 5 mm diam disk of the gel was cut out using a small punch and placed in the sample probe. Approximately 4 μl of the combined analyte solution was pipetted onto the gel disk; after 10 min, the gel section was rinsed with de-ionized water and

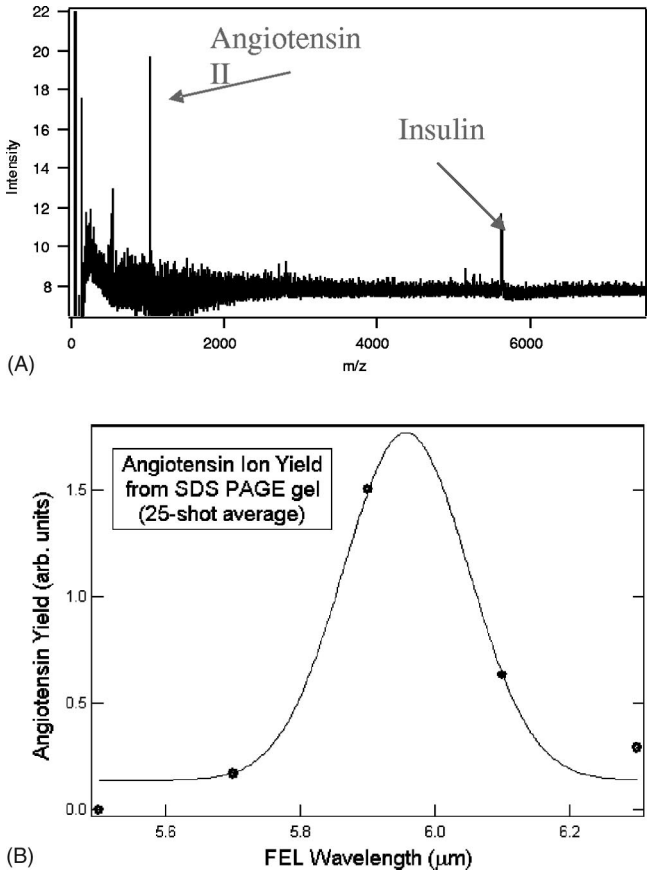

FIG. 26. (A) Mass spectrum of angiotensin and bovine insulin obtained at 5.9 μm from a polyacrylamide gel. (B) Wavelength dependence of the yield of angiotensin from the same polyacrylamide gel.

blotted. The gel disk, mounted in the probe tip, was then submerged into liquid nitrogen for approximately 30 s and placed in the cryostage.

Figure 26 shows a typical mass spectrum and the relative yields of the angiotensin as a function of wavelength near the 5.9 μm vibrational resonance that includes both the bending mode of water and the first overtone of 12 μm libration. The dependence of the ionization yield on the wavelength is an unambiguous signature of a resonant absorption process. More interesting, however, is the fact that the 10-fold stronger absorption resonance at 2.94 μm produces no ions whatever.[67] While this null result agrees with previous MALDI studies using the Er:YAG laser at the same wavelength, no satisfactory explanation has been forthcoming to date. This result is particularly vexing since irradiation of water ice using the FEL at 2.94 μm *does* produce ion signals for small proteins.[68]

B. Single-ion measurements of ion velocities

While the efficacy of IR MALDI MS has been clearly demonstrated using Er:YAG lasers,[69] the mechanism of ionization remains a puzzle.[70] To elucidate the mechanisms of infrared laser-induced desorption and ionization,[71] we measured the flight times of single ions produced by ablation of a conventional MALDI sample preparation that incorporated angiotensin into microcrystallites of 2,5-dihydroxybenzoic acid (DHB).

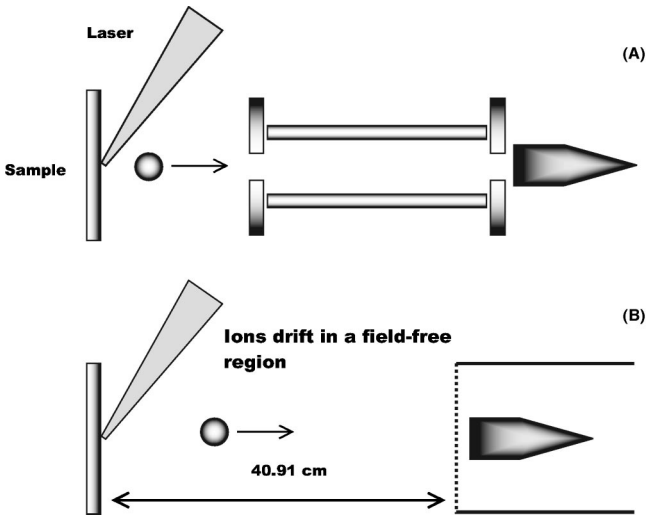

FIG. 27. (A) Experimental geometry for mass selected ion detection. The setup was used to determine the mass and energy distribution of cation ions emitted by FEL irradiation of DHB microcrystallites at 2.94 μm. (B) Experimental geometry for higher sensitivity TOF measurements made without mass selection.

Samples of 2,5-DHB both with and without dilute concentrations of angiotensin were mounted on a translatable sample manipulator in a small turbopumped ultrahigh vacuum chamber (Kimball Ion Physics); base vacuum was 10^{-7} Torr. The FEL was tuned to 2.94 μm, and 100 ns FEL macropulses were allowed to strike the MALDI target. Two experiments were then performed. First, a Stanford Research Systems RGA300 residual gas analyzer (RGA) was operated as a quadrupole mass spectrometer (QMS) to identify unambiguously the mass-to-charge ratio of the ions and ion fragments from the laser ablation. Second, nonmass-selected time-of-flight experiments were carried out by allowing the charged particles to drift in a field free region for 41 cm before passing through a grounded grid and being accelerated towards the channeltron (Burle 4730G) detector surface. The negligible effect of small axial fields in the quadrupole mass spectrometer on the velocity of the ions was confirmed by these time-of-flight (TOF) measurements. Single ion pulses generated when an ion strikes the detector surface were measured in pulse-counting mode. This is an extremely sensitive technique, since it avoids the dead-time effects in a typical MCP; however, the small apertures at the entrance and exit of the QMS, shown in Fig. 27(a), keep a large percentage of the ions from reaching the detector. Thus, measurements made using only the shielded detector are much more sensitive because of a higher signal to noise ratio.

Detector signals are routed through a CLC401AJP operational amplifier (National Semiconductor) into the Signatec PDA500 500 MHz wave form digitizer, and then processed by custom LABVIEW software, which controls the RGA, the PDA500, and an $X-Y$ sample translation stage. The arrival time of each ion was recorded and was used to generate a TOF distribution (dN/dt), from which the energy (dN/dE) and velocity (dN/dv) distributions are calculated by

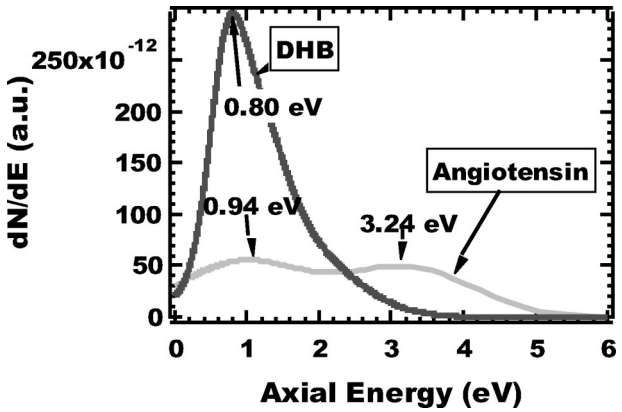

FIG. 28. Axial kinetic energy distributions of DHB and angiotensin derived from the TOF signals in Fig. 27. DHB has a relatively narrow distribution whereas the angiotensin distribution is relatively constant from 0 to 3 eV, where it gradually decays to 0 at 6 eV. The broken line represents the energy distribution of mass selected DHB+ generated by the full FEL macropulse (4 μs, 1.6 J/cm^2).

$$\frac{dN}{dv}=\frac{dN}{dE}\frac{dE}{dv}=mv\frac{dN}{dE} \quad \text{and} \quad \frac{dN}{dt}=\frac{dN}{dE}\frac{dE}{dt}=\frac{md^2}{t^3}\frac{dN}{dE}, \tag{6}$$

where m is the mass, d is the distance from the target to the detector, t is the detection time, and $E=mv^2/2$. Appropriate distribution functions are then used to fit the experimental data.

Figure 28 shows several features observed in the velocity distributions produced in this extremely sensitive TOF measurement.[71] First, the velocity distributions of the DHB matrix ions clearly reveal a fast and a slow component, both of which are too energetic to be explained by a thermal mechanism. The fact that the velocity distribution is also insensitive to the duration of the pulse, as shown by the dotted line that indicates the DHB ion velocities for the full 4 μs macropulse, also indicates a nonthermal process at work.

C. Future prospects

While the small, inexpensive N_2 laser (337 nm) is ubiquitous in commercial MALDI spectrometers, the possibility of controlling the soft ionization process by appropriate choice of the laser wavelength and pulse duration can in principle open up many new applications. For example, in our laboratory we have shown that mass spectrometry of organic compounds in waste-storage tanks can be accomplished by tuning the FEL to an absorption resonance of a nonorganic crystal, $NaNO_3$, already present in the mixture, thus avoiding the necessity of adding an exogenous matrix.

In particular, the increasing interest in imaging mass spectrometry with high spatial resolution—on biochips, in gels and other separation technologies, and in biological tissues—is likely to force reappraisal of the lasers now used for MALDI technology. In clinical applications, for example, a chemical map of tissue or cells that provides the location of specific biomolecules is clearly more useful than the mass spectrum at an isolated point. Imaging techniques, however, require high pulse repetition frequencies to be useful, with 1 kHz being a convenient benchmark. Therefore, it is likely that future analytical mass spectrometers will incorporate solid-state, high repetition-rate lasers, in spite of the added cost. Higher quality data acquired at higher speeds implies correspondingly higher throughput and more sophisticated data interpretation, thus justifying the cost differential.

While free-electron lasers are too complex and costly to use in routine analytical applications, research on soft ionization processes using FELs can help to develop the specifications for solid-state coherent sources that produce tunable, ultrashort-pulse, high repetition-rate output needed for future applications in mass spectrometry.

X. PUMP–PROBE TECHNIQUES FOR PROTEIN DYNAMICS

Here in Sec. X we review techniques to carry out time-resolved pump–probe experiments in the infrared region of protein absorption. The infrared is viewed in the broad sense, from 3 to 100 μm. Time resolved is meant to apply to the time domain where direct vibrational relaxation rates can be observed after excitation up an anharmonic vibrational ladder due to an intense burst of ''pump'' IR photons. This time range is typically 0.1–100 ps, times far too fast for many infrared detectors. Since these times are so fast, the classical way by which to obtain time resolution is via pump–probe techniques, which use optical delay lines to stagger the pump pulse relative to the probe pulse.

There are substantial concerns regarding pump–probe experiments with proteins, however, due to the fact that (1) the sample is typically dissolved in water, a highly absorptive liquid in the infrared, and (2) proteins have very small nonlinearity in the infrared region and thus need very large intensities to achieve measurable pump–probe signals.[72]

We will not discuss the biological physics that can be learned from pump–probe experiments using the far-infrared FEL at UCSB, the midinfrared SCA FEL at Stanford, and linac-based FELs,[3,72–74] but, rather, will discuss some experimental methods that have helped to solve the problems faced when carrying out pump–probe experiments using FELs. In particular we will discuss how one can use a time-delayed probe pulse (the ''reference pulse'') to decrease the common mode power fluctuations that are endemic to FELs and the problems associated with sample heating during a FEL macropulse.

A. Differential measurements

A typical FEL is not an externally seeded or regeneratively amplified laser, but instead relies on amplified power fluctuations in the electron beam to seed the subsequent IR output. Not unexpectedly, the output of a FEL is subject to large energy fluctuations both within the profile of a single macropulse and from macropulse to macropulse. As a rough rule of thumb, one can expect the fluctuations to be at best on the order of 10% of the mean. The maximum transmission change one can expect from a protein is at best 1% in a pump–probe experiment, so extensive signal averaging clearly is necessary. However, for copper-based linac FELs it is difficult to get repetition rates higher than tens of Hertz so

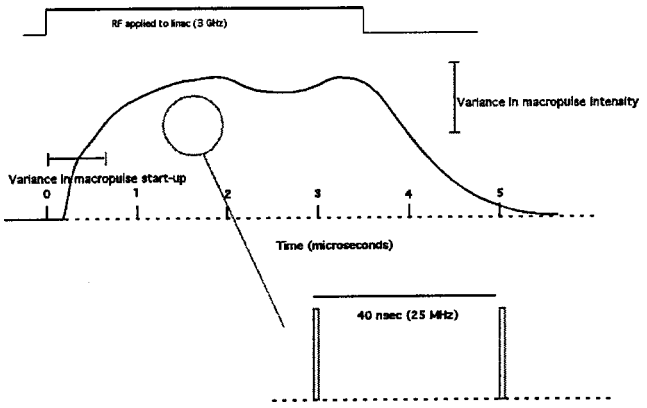

FIG. 29. Basic shape of a macropulse from FELIX.

without some sort of common mode noise rejection technique deep signal averaging is simply not time efficient.

Figure 29 shows a schematic of a free electron laser for infrared experiments macropulse. The amplitude of the macropulse can vary and there can be jitter in the start of the macropulse from variances in the self-seeding of the IR in the optical cavity. A way has been devised to get around this problem, and the core of the idea is to optically delay a reference pulse so that it falls in between the (nominally coincident in time) pump and probe pulses. This reference pulse (in the case of FELIX it is delayed 20 ns since the micropulses come every 40 ns) has no corresponding pump pulse, but is identical to the micropulse that preceded it. Figure 30 shows a possible configuration that produces a delayed optical pulse. There are two key aspects of this optical layout: (1) the reference pulse is delayed 20 ns relative

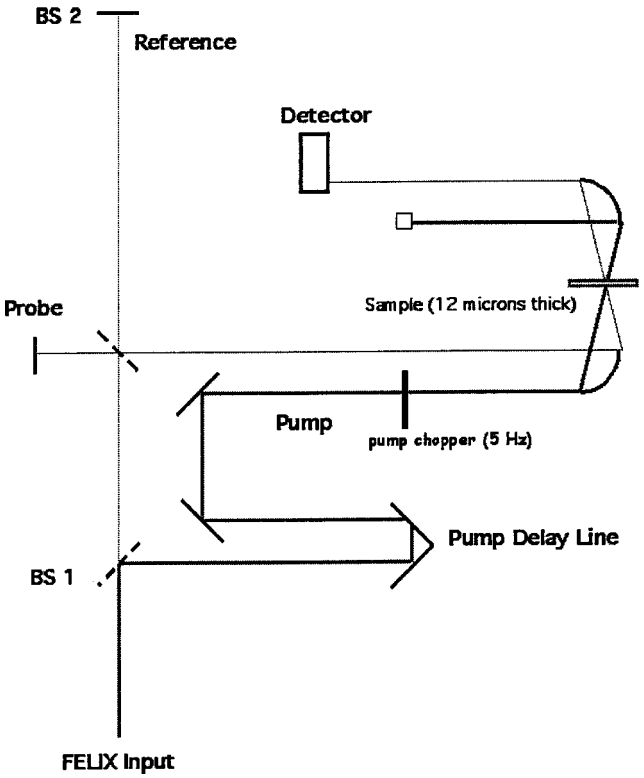

FIG. 30. Basic layout of a pump–probe experimental table with a delayed reference pulse.

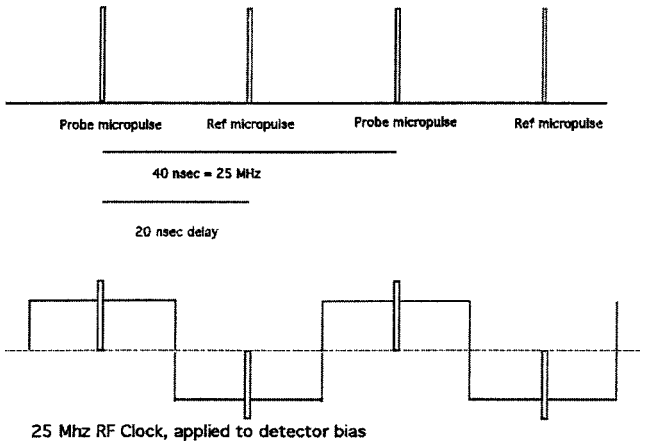

FIG. 31. Use of bias current oscillation to decrease common mode noise.

to the probe pulse, and (2) the spot size at the off-axis focal plane is 50 μm full width at half maximum (FWHM). This was accomplished by the use of a $1\times$ telescope in the reference beam arm so that the reference spot size is the same as the probe spot size. All the optical elements are reflecting, and no refractive optics were used anywhere so a He:Ne laser accurately gave beam overlaps and focal points.

Once a comb of probe and reference pulses is obtained, it is then necessary to invert and subtract the reference pulse from the probe pulse to eliminate common mode noise. In the case of HgCdTe photoconductive liquid nitrogen cooled detectors with bandwidths on the order of 20 MHz, this can be accomplished by simply inverting the sign of the bias current for the reference pulse. Then the detector output is low pass filtered, typically at a cutoff frequency of 1 MHz. Figure 31 shows a schematic diagram of how this was accomplished. Figure 32 shows the dramatic effect of subtracting the reference pulse from the probe pulse using this electronic scheme. The advantage of this technology is that it works for any photoconductive detector of sufficiently fast bandwidth, even in the far-infrared.[73]

There are, however, newer ways to achieve high common mode rejection by using the new magnetically poled detectors which offer subnanosecond resolution at wavelengths out to 12 μm. These photovoltaic detectors are very fast and quiet, with detectivity (D^*) greater than 10^8 cm $(\mathrm{Hz})^{1/2}/\mathrm{W}$ (Vigo Systems Ltd., http://www.psplc.com/). Since these detectors are so fast, it is pos-

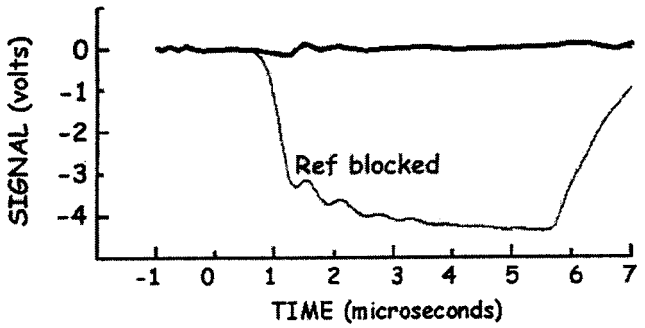

FIG. 32. Digitized traces of detector output with and without (labeled "Ref blocked") the reference beam with bias properly phased to subtract the reference pulse from the probe pulse.

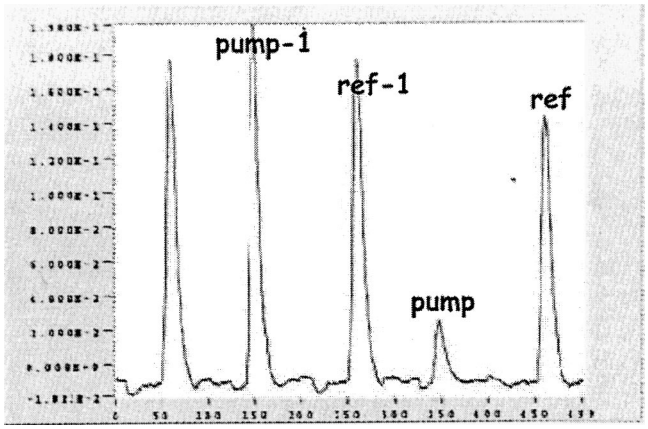

FIG. 33. Time-resolved pulse structure using magnetically poled detectors. The probe and reference pulse before a single pump pulse are shown. The sample in this case was a silicon wafer, and the pump pulse was a 530 nm pulse of visible light. The photogenerated carriers increase the reflectivity of the silicon.

sible to easily resolve individual micropulses within the macropulse train. Modern digital scopes such as the Tektronix 3052 offer 5 gigasamples/s, 500 MHz bandwidths, and GPIB transfer rates of 100 000 bytes/s with a 9 bit analog to digital converter (ADC) and can be used to capture at 10 Hz pulse trains in the detectors. A ''digital boxcar'' has been developed at FELIX using the fast signal averaging and fast transfer rates of the 3052, the high speed response of the VIGO detector, and a delayed reference pulse to do very fast boxcar averaging of *single* micropulses, normalized to a reference pulse to compensate for fluctuations in intensity of the FEL. Figure 33 shows how the pulse train looks in a time-resolved manner for a single pump pulse, pump–probe experiment using this new technology. The reason for doing single pump–pulse experiments is discussed in Sec. X B.

B. Energy and power considerations

One of the principal problems in performing biological IR pump–probe experiments is the fact that the sample usually must be contained in water that strongly absorbs in IR, and that large amounts of power are necessary to accomplish a significant nonlinear response in a protein. We should mention here that the IR absorption of water vapor is also a major problem in IR pump–probe dynamics, but we have discussed this previously[75] and assume that the experimenter has gone to great lengths to purge water vapor from all parts of the IR transport system. In the case of liquid water, the absorption length of water at 6 μm is 4.6 μm,[76] so it is necessary to keep the sample thickness to 20 μm or less. Further, in order to deliver the highest power for a given pulse energy it is important to keep the focused area of the pump pulse as small as possible. Fifty μm is an achievable spot size at 6 μm with high f/number off-axis parabolic optics. This then means that the illuminated volume is quite small, on the order of 5×10^{-8} cm^3. For a micropulse energy of 10 μJ, the rise in temperature is 200 K!

For 0.1 μJ per micropulse, we observe a more reasonable temperature rise of 2 K per micropulse. However, at least for copper linac FELs the IR pulses occur in a train of micropulses called a macropulse, and the rate at which these micropulses occur is between 2 GHz and 25 MHz. Even at the lowest repetition rate of 25 MHz that we have used there is an accumulation of thermal energy in the focal region due to the finite rate at which heat can diffuse. There are many misconceptions about thermal decay times. A common one is that heat is carried away at the speed of sound. This cannot be true except in the case of shock waves, otherwise if you touch a hot object your feet would feel warm in a millisecond. In fact, heat dissipation is a diffusive process and the decay times are related to the diffusion times in liquids of solvent molecules. The equation for heat flow yields

$$\nabla^2 T = (C_p/\kappa)\partial T/\partial t, \tag{7}$$

where C_p is the specific heat at constant pressure of the material and κ is the thermal conductivity. In our experiments, we have essentially one-dimensional heat flow, since the sample thickness (12 μm) is small compared with the IR beam diameter (50 μm). For analytical simplicity, we assume that the initial jump in temperature caused by the laser is a Gaussian distribution like that expected for a TEM_{00} beam. Cooling of the sample is roughly exponential in time, and the time constant τ for cooling of the sample under these conditions is

$$\tau = L^2 C_p/4\kappa, \tag{8}$$

where L is the thickness of the sample. Table I gives cooling times for various materials used in our sample construction, assuming a 12 μm sample thickness. We have added a column labeled t_c, the time required for the sample to return to 5% of the original temperature. This time basically sets the maximum repetition rate for which no appreciable rise in temperature will be observed in steady state.

TABLE I. Time constants of thermal relaxation in selected materials.

Material	C_p (J/cm^3/K)	κ (W/m K)	τ (μs)	t_c (ms)
H_2O	4.18	0.57	126	50
$CDCl_3$	0.96	0.12	144	58
CaF_2	2.67	10.0	3.5	1.4
BaF_2	1.97	11.0	4.4	1.8

Typically a macropulse from a copper linac FEL has a macropulse duration of about 4 ms. Therefore, there is limited heat dissipation during a macropulse. The heat generated from repetitive IR FEL micropulses is accumulated over a macropulse. With 1 μJ energy per micropulse and 20% sample absorption, the jump in temperature from a single micropulse is 2 °C in H_2O. With over 100 micropulses in one FELIX macropulse, this heat leads to an extremely large rise in temperature of about 200 °C in H_2O! This analysis shows that sample heating is a serious problem in pump–probe experiments. In order to measure *true* signals without contamination due to sample heating, it is essential to use a small number of micropulses at the beginning of each macropulse.

Another, more subtle, effect is due to the fact that in a pump–probe experiment the pump and probe beams are coherent with one another because they have been split from

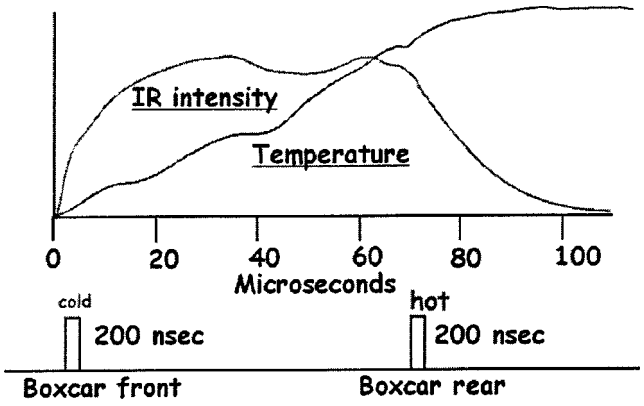

FIG. 34. Schematic of the rise in heat during a macropulse from FELIX. The lines are drawn with noise to try to indicate the typical variances in power that occur in a FEL macropulse. The boxcar gates show how pump–probe signals can be extracted at the beginning and end of a macropulse.

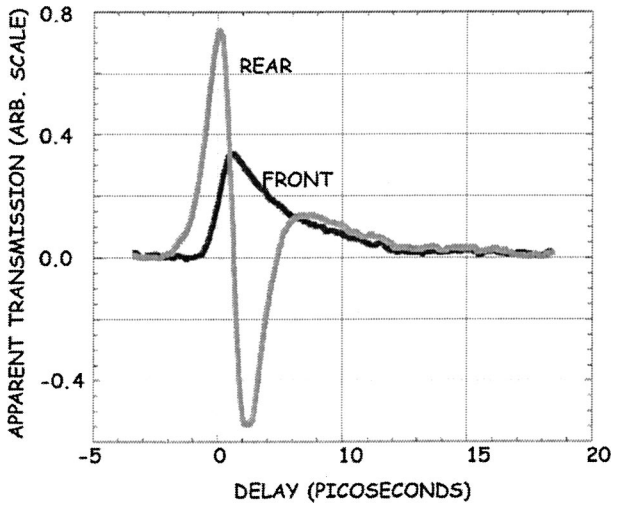

FIG. 35. Difference in pump–probe signal between the front and rear of the macropulse. Oscillations in the apparent pump–probe signal seen with movement of the delay line for the rear signal are presumably an artifact of the temperature-grating signal.

the initially coherent light beam coming from the FEL. This means that the temperature pattern across the focal region is not uniform but instead is modulated in a sinusoidal manner. This thermal grating can diffract pump energy into the probe beam in a constructive or a destructive manner, giving rise to oscillations in the apparent response of the sample to the pump energy which have very little to do with the actual picosecond relaxation of the vibrational levels.

It is easiest to see and document all of these purely temperature related phenomena by using a pair of boxcar integrators timed to look at the pump–probe signal at the beginning of the macropulse when the sample is ''cool'' and at the end of the macropulse when the sample is thermodynamically ''hot'' due to deposition of energy into the sample. Figure 34 is a schematic of the rise in temperature that can be seen through a macropulse and the placement of boxcar integrating gates that can be used to extract the cold and hot temperature signals. Technically we should only use the leading signal from the macropulse signal, but it is interesting to observe the very strange effects that occur as the delay line moves the pump pulse relative to the probe pulse: the heat-grating diffracted signal from the pump pulse is observed to oscillate in phase relative to the probe pulse, resulting in constructive and destructive interference. Figure 35 shows the dramatic difference in signal seen at the front and rear of a macropulse in pump–probe signals. Note that we do not believe these signals to be true picosecond phenomena since they do not occur at the cold front of the macropulse, only at the rear. Clearly, single pulse pump/probe experiments are more preferable due to the sample heating problem.

We hope that in this review we have highlighted some of the techniques that make pump–probe experiments possible on biological samples, and that discussion of the severe heating problem that must be understood and controlled in order to extract meaningful data was useful.

XI. APPLICATIONS IN TIME-RESOLVED FLUORESCENCE AND TRANSIENT ABSORPTION USING THE SUPER-ACO FEL

The Super-ACO is a tunable, coherent source in the UV based on a storage ring FEL.[77] It produces 350 mW at 350 nm for the user community with 15–50 ps FWHM pulse at a repetition rate of 8 MHz. The first applications experiments occurred in 1993 with a study of the anisotropy decay of the coenzyme NADH.[78] Anisotropy decay results from perturbation of the initial distribution of moments of electronic transition due to Brownian reorientation and consequently describes the rotational dynamics of the system. The goal is to understand the thermodynamical equilibrium of different conformational states of the molecule and their hydrodynamical volume in solution.

After the first one-color experiment using time-resolved fluorescence, a transient absorption experiment was developed where the system is excited with the UV FEL and is probed by visible-UV absorption using synchrotron radiation.[79] From microsecond flash photolysis to femtosecond laser photolysis, the principle of transient absorption spectroscopy is based on powerful optical excitation that promotes a large fraction of the molecules into the excited state, which is then probed by a second white/tunable light source. The transient absorption detection method is particularly useful for the study of relaxation dynamics and direct identification of the associated excited states and/or transient species via their spectral signature. A novel approach is two-photon spectroscopy based on the combined use of the storage ring FEL and synchrotron radiation to study the electronic states of various biological chromophores. From the beginning of the development of microsecond flash photolysis, biologists have investigated the chemistry of exogenous or endogenous molecules of biological interest at different time scales. These methods allow the investigation of fundamental processes of chemical reactivity in the liquid phase at new wavelengths and over short time scales. For example, charge transfer (electrons, protons, radicals) or the relaxation of structure (isomerization, dissociation and recombination, torsion, movements of great amplitude, intramolecular movements) is involved in significant biological phenomena such as photosynthesis, vision, structural modifications of

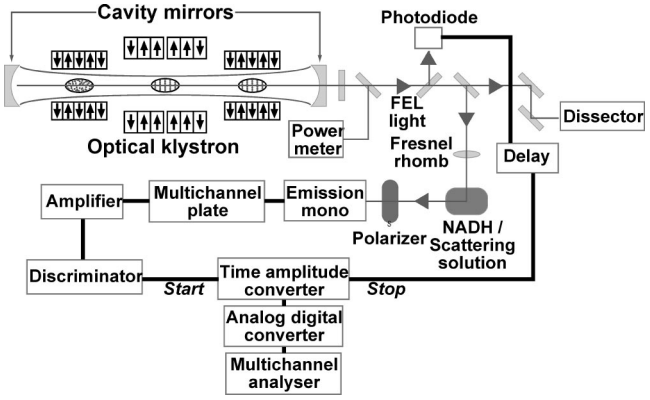

FIG. 36. Schematic diagram of the photon counting fluorescence experiment. A Hamamatsu R1564U-06 microchannel plate photomultiplier was used for fluorescence detection, and a fast Hamamatsu S4753 silicon photodiode with homemade amplification was used for synchronization. The polarization of the incident light is rotated to the vertical direction by a Fresnel rhomb for detection at 90° in the horizontal plane of independent components $I_{\parallel}$ and $I_{\perp}$ of the fluorescence. The polarized components $I_{vv}(t)$ and $I_{vh}(t)$ are obtained by orienting the emission polarizer to vertical and horizontal positions, respectively. The apparatus function $g(t)$ was recorded at the excitation wavelength with a scattering solution of Ludox® (DuPont Co.) in place of the sample.

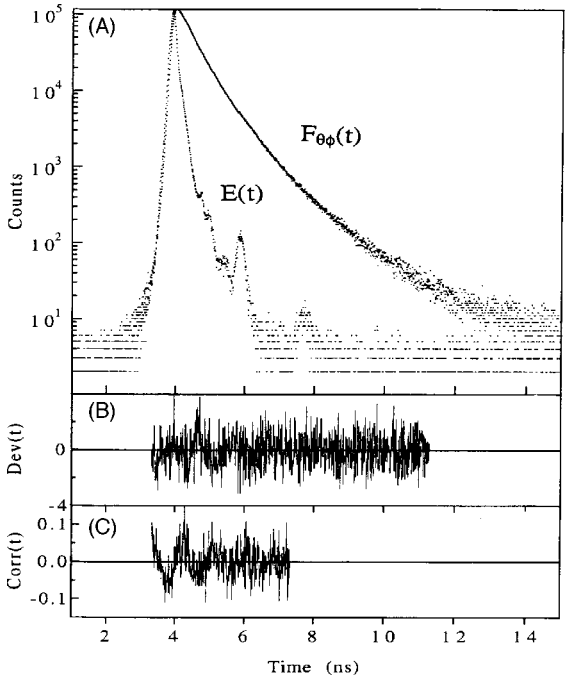

FIG. 37. Single photon counting data obtained with the Super-ACO SR FEL: (A) Total fluorescence decay $F(t)$ of NADH at pH 8, 10 °C, λ_{exc} 350 nm, λ_{em} 460 nm, and corresponding instrumental function $g(t)$; (B) residuals obtained from maximum entropy method analysis of the decay in (A); (C) autocorrelation of the residuals.

DNA or proteins, enzymatic reactions, mechanisms of transport, and photochemotherapy.

A. Time-resolved fluorescence experiments

The experimental layout of the time-resolved fluorescence experiments is shown in Fig. 36. The sample under study is irradiated by a short FEL pulse, and its fluorescence decay $F(t)$ is recorded by measuring the arrival time of single photons of fluorescence versus a synchronization signal (Fig. 37). The photons must be selected randomly, not more than one per excitation pulse, to avoid pile-up effects. For each fluorescence decay curve, about 10 million total counts were stored, giving approximately 10^5 counts at the peak (Fig. 37). The counting rate should be maintained at approximately 10 kHz for optimum time response. Thus a measurement is completed in approximately half an hour. The excitation wavelength was 350 nm ($\Delta\lambda_{exc}=1$ Å being the linewidth of the FEL emission) and the emission wavelength was 460 nm ($\Delta\lambda_{em}=8$ nm), selected by a H10 Jobin-Yvon monochromator.

NADH (β-nicotinamide adenine dinucleotide, reduced form) from Sigma Chemical Co. was studied in a 10 mM tris-(hydroxymethyl)-aminomethane buffer at pH 8, and contained 0.02% sodium azide as an antibacterial agent. The final concentration of NADH in fluorescence measurements was 18 μmol/l, giving an optical density of about 0.1 at 350 nm in the 1 cm path of a quartz cuvette. NADH can bind to a large variety of enzymes, and provide the H^+ ions or electrons for chemical reactions, which are catalyzed by the dehydrogenase. It constitutes an *in vitro* natural probe of the active sites of these enzymes. In addition, it is used as an indicator of the metabolic state of organisms and tissues in imaging techniques. In its reduced form, NADH shows an absorption band at 340 nm and an emission band in the visible, centered around 460 nm, with a quantum efficiency of 2%. The oxided form (NAD+) neither absorbs nor emits in this spectral range.

The temperature dependence of the measured lifetime distributions of NADH fluorescence decay is shown in Table II. The decay is described well in all cases by three to four clearly separated relaxation processes, only two of which make a significant contribution to the kinetics (0.28 and 0.62 ns). The temperature dependence of the nonradiative rate is described by an Arrhenius law, the frequency factor A and the activation energy E_a characterizing the dynamic quenching process. A linear fit, $\ln(1/\tau_f - k_R) = \ln A - E_a/RT$ assuming[79] $k_R = 5\times10^7$ s^{-1} leads to an activation energy of 2.6 ± 0.3 kcal/mol and a frequency factor of $2\pm1\times10^{11}$ s^{-1}. We observe a shift of the lifetime amplitudes from the long to the short component when the temperature is increased, and Arrhenius dependence of both components with similar activation energies of about 1.5 kcal/mol. The amplitudes c_i of the different components in Table II can, to first approximation, be identified as the relative populations of chromophores that have the corresponding fluorescence lifetime, with the equilibrium constant being $K = c_2/c_1$. The thermodynamic parameters (Table II) governing this equilibrium are obtained by the linear fit

$$\ln K = -\frac{\Delta H}{R}\left(\frac{1}{T}\right) + \frac{\Delta S}{R}, \tag{9}$$

assuming that these parameters are approximately constant in the temperature range studied. These data are in good agreement with data obtained by other techniques.[80]

Polarization of the fluorescence depends on the distribution of moments of the electronic transitions responsible for

TABLE II. Fluorescence measurements of NADH performed with the super-ACO FEL.

Temperature (°C)	c_1 ±1%	τ_1, ns ±0.01	c_2 ±1%	τ_2, ns ±0.02	c_3	τ_3, ns ±0.2	$\overline{\tau}$, ns ±0.01	χ^2
10	61%	0.30	38%	0.70	1%	1.7	0.47	1.30
20	68%	0.28	32%	0.62	<0.1%	1.8	0.39	1.20
40	78%	0.24	22%	0.55	<0.01%	2.1	0.31	1.24

Arrhenius fits for different fluorescence decays.

	τ_1	τ_2	$\overline{\tau}$
E_a	1.4±0.3 kcal/mole	1.5±0.1 kcal/mole	2.6±0.3 kcal/mole
A	$4\pm3\times10^{10}$ s^{-1}	$2\pm1\times10^{10}$ s^{-1}	$2\pm1\times10^{11}$ s^{-1}

Thermodynamical parameter $K=c_2/c_1=\exp(-\Delta G/RT)$ with others techniques.

Technique	ΔH (kcal/mole)	ΔS (cal/K mole)	$G^{0\,°C}$ (kcal/mole)
Fluorescence	−5.0±0.2	−18.5±0.7	+0.1±0.4
NMR	(−5.6±0.2)	(−17.5±1)	(−0.8±0.2) (+0.4±0.1)

the emissions process, which is related to rotational Brownian motion of the molecules in solution. The decay of anisotropy of a chromophore rigidly attached to a sphere can be described by $r(t)=r_0\exp(-t/\tau)$ where r_0 is the static anisotropy related to the angles between the moments associated to absorption and to emission and τ is the relaxation coefficient, which is inversely proportional to the rotational diffusion coefficient of a sphere. The measurements of fluorescence anisotropy decay lead to very fast depolarization of the nicotinamide ring, independent of the rest of the NADH molecule. We find an average hydrodynamic volume of 1000 ±100 Å^3 for NADH, which would correspond to a sphere with radius of 6.2 Å. This is in good agreement with the volume of a folded configuration (836 Å^3) given by a van der Waals model. The spatial conformations deduced are shown in Fig. 38 in folded and open conformations. These results are in agreement with those obtained from previous nuclear magnetic resonance (NMR) studies of aqueous NAD.[81]

B. Transient absorption experiments

Figure 39 shows the transient absorption experimental setup employed at Super-ACO. Control of the spatial overlap between the pulses is critical. To monitor this, we mounted a quartz lens, which was used to focus the pump beam onto the sample, on an $X-Y-Z$ manipulator. The pump beam can then be moved and focused precisely in the region where the probe beam intersects the sample. This region where the two photon beams intersect is optimized with the signal obtained by a charge coupled device (CCD) camera in steady-state operation. The time-resolved experiment was performed at a lower repetition rate, i.e., 83.2 kHz, than the normal one (8.32 MHz) using a Pockel's cell.

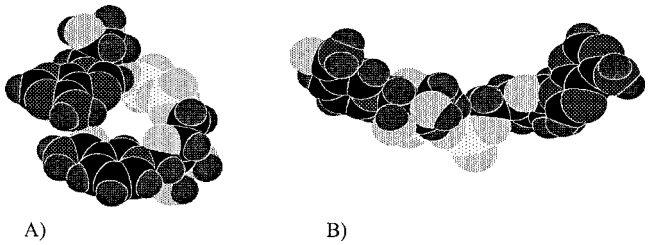

FIG. 38. Possible conformations of aqueous NADH. (A) Folded form constructed from minimized fragments of the NADH chemical structure under stereochemical rules borrowed from the DNA structure. (B) Structure adopted by NADH within the active site of lactate dehydrogenase in its ternary complex with oxamate, according to the x-ray crystallographic data of C. Abad-Zapatero, J. P. Griffith, J. L. Sussman, and M. G. Rossmann (1987) J. Mol. Biol. 198 445, entry 1LDM of the Protein Data Bank.

Acridine from Prolabo, used without further purification, was studied. Absorption spectra were recorded using a Cary 210 (Varian Inc.) spectrophotometer. Typically, a 0.1 cm or a 1 cm quartz optical cell was used. Its final concentration was 116 μM and 1.6 mM, giving an absorbance of about 0.5 at 350 nm and absorbance of about 1 at 363 nm, respectively, in the 0.1 cm path of a quartz cuvette.

The absolute intensity of a differential transient absorption spectrum $\Delta A(\lambda,t)$ is directly proportional to the population of the molecule in an excited state. Assuming that the pump beam interacts only via the transition $S_0\rightarrow S_1$, the saturation fluence is $F_S=1/\sigma_{\alpha0}(\lambda)$ where $\sigma_{a0}(\lambda)$ is the absorption cross section of the ground state (in units of cm^2) at wavelength λ. The pulse fluence of the pump should be of the same order as the saturation fluence in order to excite a large fraction of the molecules. The FEL power on the sample is limited to a maximum of 100 mW, which corresponds to energy of 12 nJ per pulse (i.e., 2×10^{10} photons/pulse). The pump beam is focused onto the sample to within a diameter of ~20 μm, leading to the possibility of fluence approximately equal to the saturation fluence. In the simplest situation, the pump/probe signal observed is proportional to the population that is not in the ground state. Thus, if the ground state is the only absorbing state, then the pump/probe observable is given by $S(t)=A\langle P_{\rm ex}(t)\rangle$ where A is a constant determined by experimental parameters such as the laser intensity and the probability that the system is found in the excited state $\langle P_{\rm ex}\rangle$. If the probe wavelength is in the spectral region of existing absorption of the ground state or of the stimulated emission, bleaching of the solution may be observed. This was the case in our investigation of acridine. The change in transient absorption shown in Fig. 40 displays decay of the transient at 430 nm. The lifetime of the first

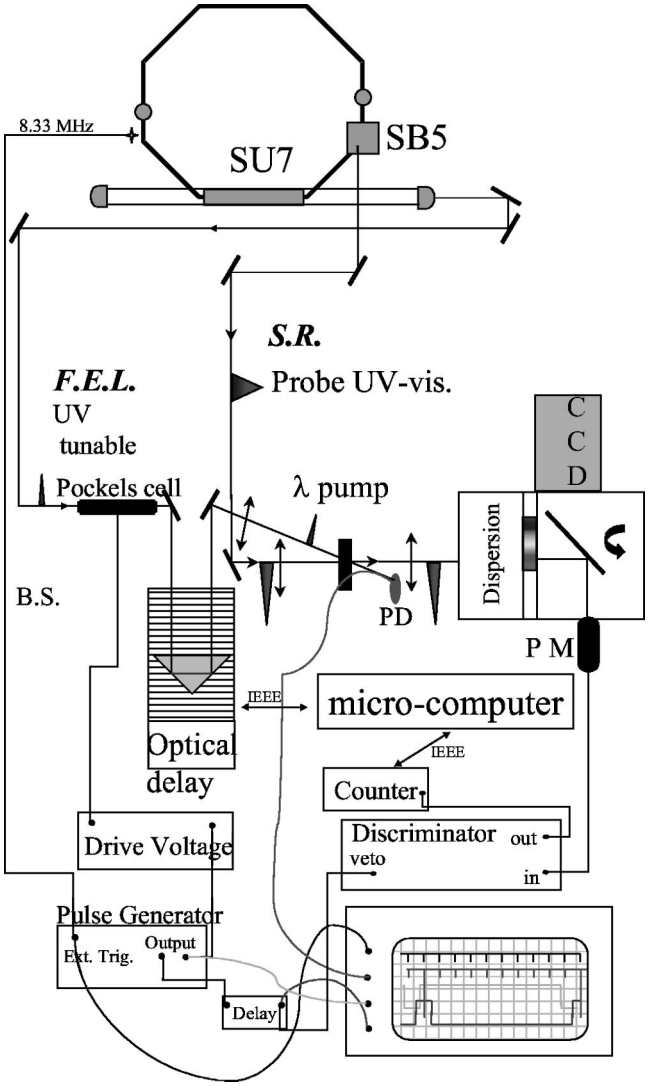

FIG. 39. Schematic diagram of the transient absorption experiment (SU7—undulator; SB5—bending magnet; PD—photodiode; PM—photomultiplier; BS—bunch signal). The UV-SR FEL pump was variably delayed by a computer-controlled translation stage, with accessible delay ranges from $+4.5$ to -3.5 ns (a positive delay corresponds to the UV-SR FEL pump pulse impinging on the sample before the probe pulse). The white light emitted by a bending magnet via the SB5 beamline is extracted to generate a white probe pulse in the 400–700 nm range. Both the pump and probe beams are focused onto the sample, and cross at a 7° angle in the sample, which flows through a 1 mm thick quartz cell. The entire white continuum pulse is sent to an imaging spectrometer (Princeton Instruments, Inc. model SpectraPro-750 monochromator) and detected by a thermoelectrically cooled CCD camera (TE/CCD-1752-PF/UV, chip size: 1752×532) in steady-state operation or by a photomultiplier (Hamamatsu RS928) in time-resolved operation.

singlet excited state determined by convolution is 1.1 (±0.2) ns. These results are consistent with those of Shapiro and Winn[82] (fluorescence lifetimes of 375 ± 50 and 817 ± 80 ps for excitations at 355 and 396 nm, respectively).

C. Future prospects

The energy per pulse of an advanced storage ring FEL such as the one proposed for the French Synchrotron Radiation facility SOLEIL will be sufficient (3–10 μJ) to carry out quasisaturation of the excited state in the active volume.

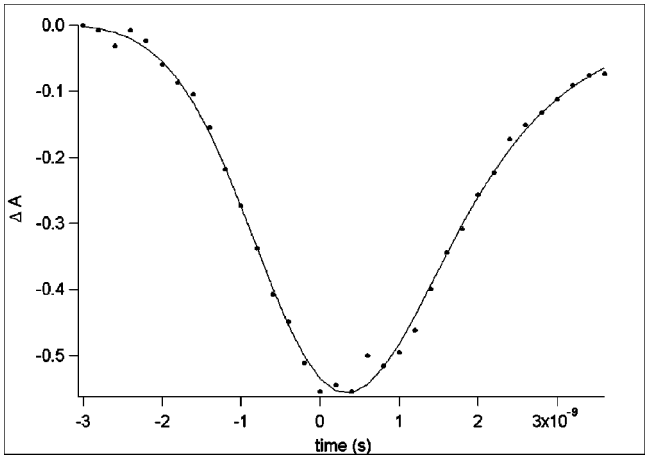

FIG. 40. Pump/probe data for the acridine in ethanol. The smooth line represents the fit of the data.

Moreover, this capability will allow operation to the edge of vacuum UV (200 nm or possibly shorter), which will open an entirely new spectroscopic field for transverse acoustic (TA) spectroscopy in the nanosecond and subnanosecond regimes. Thanks to the tunability of advanced storage ring FELs, it will be possible to study the excited states produced by UV irradiation of a wide variety of chromophores, indicated in Table III. Such photoreactions define the very first stages of certain processes of cytotoxicity.[84] Besides, the primary species that result from the excitation of trytophan are mainly the origin of the photodegradations induced by the irradiation of proteins. In addition, nonradiative relaxation is still poorly understood, i.e., specifically how it affects the intensity and the kinetics of tryptophan fluorescence, which is used extensively in the study of structural and dynamic properties of proteins *in vitro*.

The exact photophysical consequences of the excitation of the peptide bond ($\lambda_{exc}=200$ nm), present at very strong concentrations in proteins, are still poorly known. These mechanisms could be of great importance for the comprehension of complex evolutionary processes such as the aging of proteins. Oxidative condensation of catecholamines such

TABLE III. Intrinsic and extrinsic chromophores in biological systems. For a list of additional extrinsic chromophores (used in fluorescence) see, for example, Ref. 83.

Proteins
Tryptophan, tyrosin (280 nm), peptidic bond (200 nm)
Cystein (200 nm), histidin (230 nm), phenylalanin (250 nm)
Coenzymes and prosthetic systems
NADH, NADPH (350 nm), flavins (450 nm)
Hemes: 400 nm, 550 nm and porphyrins: 500–650 nm
Quinones: 260–280 nm, retinal: 280 and 500 nm
Pigments and neurotransmitters
Chlorophylles (360, 580, and 800 nm), carotenoids (400–500 nm)
Adrenalin (280 nm), adrenochrome (300 and 480 nm)
Nucleic acid
Purins and pyrimidins (260 nm), wybutine (310 nm)
Drugs
Radiosensitizer, psoralens, phenothiazins

as adrenalin ($\lambda_{exc}=280$ nm), implied by the formation of various forms of melanin, brings into play uncharacterized reactive species, which transient absorption spectroscopy promises to identify.

The nanosecond time scale constitutes a ''key'' field for comprehension of the primary photophysical processes. Taking into account the intensity of the electronic transitions $S_0\langle-\rangle S_1$, the intrinsic lifetime of the excited state for these chromophores is in general about a few tens of nanoseconds. The various decay processes of this excited state, which are the starting points of the various photochemical or photophysical pathways, must thus be on an equal scale or more rapid than the nanosecond. Thus accessing subnanosecond processes holds the promise of reaching the initial crossroads from which the evolution of the excited state will be determined.

XII. UV-PUMP, BROADBAND-IR-PROBE SPECTROSCOPY

The Duke storage ring, OK-4 FEL, is a pulsed source of coherent UV radiation, tunable from 193 to 400 nm.[85] In addition, the bending magnet downstream of the OK-4 FEL is a source of broadband infrared radiation. Because the same bunch of electrons emits both pulses, the timing between the UV and IR pulses is essentially jitter free and the time resolution attainable is thus limited only by the pulse width. The capability to excite systems with tunable ultraviolet radiation and then probe the relaxation processes throughout the mid infrared with a time resolution on the order of 100 ps is unique, and it opens the way to the study of photochemical and photobiological systems not previously accessible to time-resolved infrared spectroscopy. A beamline was commissioned to take advantage of these synchronized light sources, recognizing that the repetition rate of 2.79 MHz is ideal for rapid-scan, asynchronous sampling.[86]

A. Synchronized light sources for two-color, time-resolved spectroscopy

The OK-4 FEL has been operational since 1996 and in 1999 water-cooled copper disks were installed in the corners of the storage ring with optical flats that extract synchrotron radiation. The acceptance angles for the capture of synchrotron radiation are 57 mrad horizontally and 14 mrad vertically. While the vertical acceptance angle severely restricts the collection of the far infrared ($<500\ \mathrm{cm}^{-1}$), theoretical extraction of midinfrared radiation is comparable to that of beamlines at National Synchrotron Light Source at Brookhaven National Laboratory.[87]

Figure 41 shows the layout for the optical and vacuum systems to collect infrared synchrotron radiation, where the copper flat reflects radiation downward. A gold-coated plane mirror located 20 cm below the flat reflects the synchrotron radiation towards a 6 in. diam, $f/6$ spherical mirror. The spherical mirror directs the synchrotron radiation back past this plane mirror and focuses the light through a CaF_2 window that separates the ultrahigh vacuum (10^{-10} Torr) of the storage ring from the remainder of the beamline (10^{-7} Torr). The synchrotron radiation that emerges from the storage ring vacuum chamber is then collimated by a 90° off-axis parabolic mirror ($f_{\mathrm{eff}}=7.5$ in.). The collimated synchrotron radiation is then directed 20 m down the beamline by a pair of plane steering mirrors. The synchrotron radiation is brought out of the beamline vacuum system at the endstation through a second CaF_2 window. At this point, the synchrotron radiation (SR) encompasses wavelengths from $\sim$450 nm to 9 μm, limited at long wavelengths by the CaF_2 windows.

Once at the endstation, Fig. 42, the SR is directed through a N_2 purged path to the same level as that of the optical table by a steering mirror and focused by a 90° off-axis parabolic mirror ($f_{\mathrm{eff}}=5.5$ in.). The focal point serves as an effective point source for a Bruker IFS-66v FTIR spectrometer. We have measured the SR power with FTIR and compared it to theoretical expectations. Due to the effects of beam divergence over the 20 m between the collimating mirror and the endstation and reflection losses from each mirror and window, approximately 40% of the theoretically available synchrotron radiation power is delivered to the FTIR. Using a collimating mirror with a longer effective focal length could reduce divergence losses. However, the mirror currently in use has the longest f_{eff} available in a diamond-turned 90° off-axis paraboloid.

The storage ring current and consequently the synchrotron radiation power decrease exponentially during the course of a single injection cycle of the storage ring. This creates a drift problem for measuring pump–probe difference spectra, since the low light levels require 5 min of signal averaging to achieve a signal to noise ratio (SNR) of 1000 (i.e., the ability to detect pump-on versus pump-off difference signals of 0.001 absorbance units). Consequently, we have installed an electronic shutter to measure the pump-on and pump-off spectra as an interleaved set, thus avoiding untoward consequences of drift in optical power.

To perform the two-color pump–probe experiment we must also deliver the coherent UV output of the OK-4 free-electron laser to the sample, as shown in Fig. 42. This is accomplished by extracting the UV light from its evacuated beam tube that is mounted parallel to the vacuum tube that transmits the infrared radiation. Once the UV-pump pulse arrives at the optical table, it is directed through a delay line and then focused onto the sample in the FTIR spectrometer. We can vary the relative arrival times of the UV-pump and SR-probe pulses at the sample by >10 ns, at which the intensities of the two pulses have been shown to remain constant within 5% without any realignment of the optics as the optical path length is varied.

A Hamamatsu streak camera was used to measure the pulse width of the synchrotron radiation. The results of this measurement show that the SR pulse width increases as single-bunch current in the ring is increased, up to 360 ps at 10 mA. When these pulse width measurements are compared to those taken in 1998 over a lower current range (the two sets of measurements overlap near 3 mA), the pulse widths are now a factor of 2 higher than they were in the past.[88] By optimizing the electron orbit in the ring, this factor of 2 should be recovered. The lasing pulse widths of the OK-4

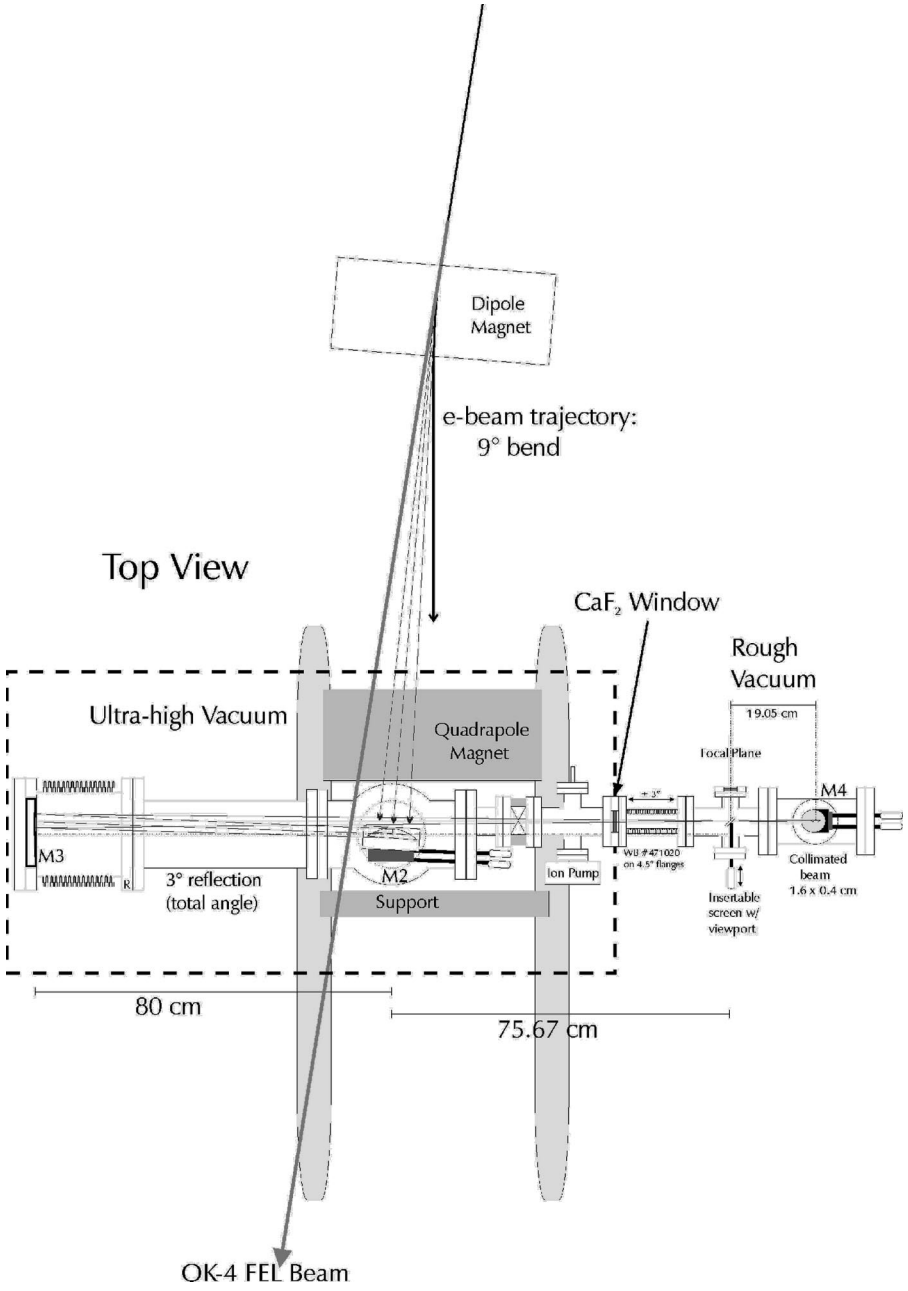

FIG. 41. Schematic diagram of the broadband IR collection optics of the synchrotron beamline.

will be a factor of ~5 smaller than the synchrotron radiation pulse widths.

We have commissioned this pump–probe beamline and performed initial characterization of both light sources. While the synchrotron radiation power level is only ~200 μW between 2 and 9 μm, we have maintained the intrinsic brightness of the SR throughout the beamline. The SR pulse width is 200–400 ps (FWHM) depending upon the amount of current stored in the electron bunch. Coherent radiation from the OK-4 that is used to excite the samples has a pulse width 2–5× shorter than the SR and approaches 5 mW of average power for single-bunch operation of the storage ring.

B. Asynchronous sampling

The high intrinsic repetition rate of this storage ring is compatible with the asynchronous sampling method.[89] For our applications, the broadband IR source probes a sample material that is resonantly pumped in the UV, as summarized in Fig. 43. The IR source can be viewed as a distribution of Fourier components. Part A represents an interferogram for a single Fourier component, i.e., one first modulated in intensity by the Michelson interferometer, then passing through an absorbing sample onto the detector. Part B represents perturbation to the probe signal due to repetitively pulsing with the UV pump. In part C, a pulsed IR probe is synchronized to the UV pump to interrogate the relaxation of the excited state due to UV absorption, where the traces in parts A and B are included for reference. Since neither the pump nor the probe pulses are synchronized to the scanning of the Michelson interferometer, over time all phases of the modulated intensity are measured. As shown in part D, the discrete interferogram of part C has been converted into a continuous inter-

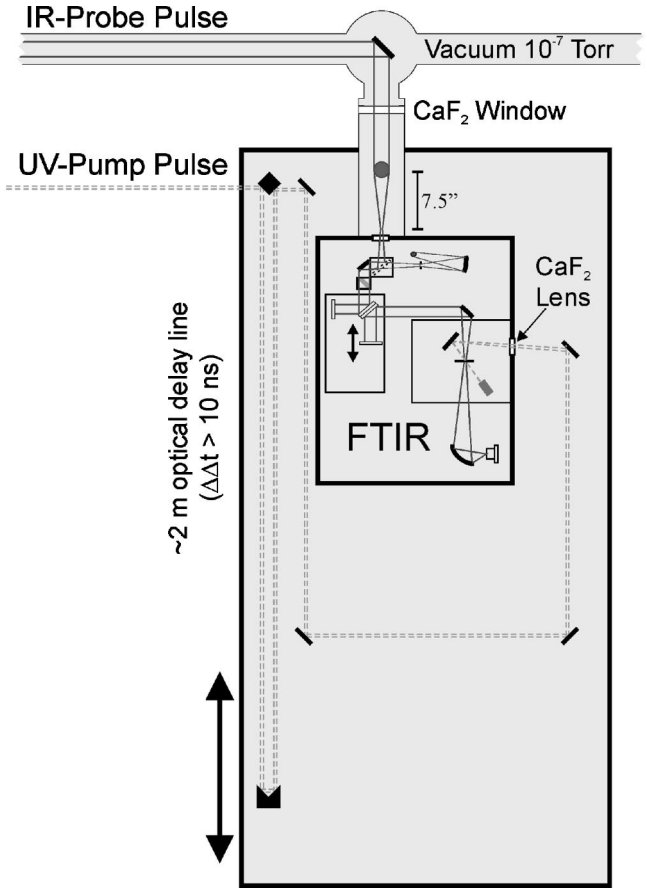

FIG. 42. Schematic diagram of the endstation for UV-pump, broad band IR-probe spectroscopy.

ferogram with a low pass electronic filter. Note the repetition rate must exceed the highest Fourier frequency by a factor of 2 (40 kHz in our case) to avoid aliasing, a sampling artifact. Fourier transforming the sum of the interferograms for all of the Fourier components results in a single-beam spectrum, which can be put into a ratio against the no-excitation spectrum to generate a differential absorption spectrum. By systematically varying the delay between the pump and probe, the overall relaxation processes are mapped. In single-bunch mode, the synchrotron radiation pulse repetition rate of the Duke storage ring is 2.7898 MHz, well in excess of that required for asynchronous sampling FTIR.

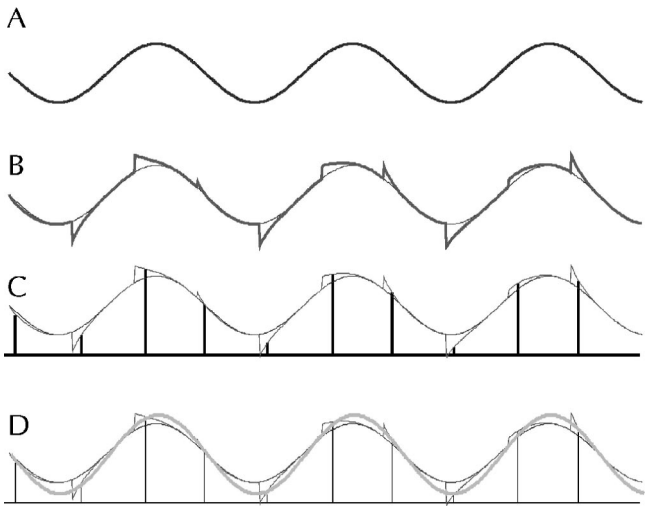

FIG. 43. Asynchronous sampling method for time-resolved FTIR that plots the intensity as a function of mirror retardation or, equivalently, of time. See the text for further explanation.

C. Future prospects

As an example of the type of experiments to be performed, consider the unanswered questions that surround the enzymatic mechanism of DNA photolyase. This protein binds to UV-induced lesions in DNA (specifically pyrimidine dimers) and then catalyzes the cleavage of the pyrimidine dimers when exposed to blue light.[90] All evidence points to the involvement of photoinduced electron transfer in the catalytic mechanism. However, time-resolved absorption spectroscopy in the UV–visible spectral region has not been able to identify the nature of the intermediates in this process.[91] Once the photoexcitation of the bound flavin chromophore was quenched, an unidentified intermediate arose within 2 ns of the flash ($\lambda_{max}=400$ nm). The remaining steps were silent in the visible spectral region. By extending the accessible spectral range to include the near and mid-IR, the electron transfer events in this photocycle should no longer remain spectrally silent. Vibrational frequencies in the mid-IR are extremely sensitive to changes in the spatial distribution of electron density. By simultaneously probing a broad range of mid-IR frequencies, we will be able to monitor the catalytic involvement of the flavin chromophore, residues of the enzyme, and the DNA bases of the pyrimidine dimer. In addition, the time-resolved FTIR spectra will contain information regarding conformational changes in the protein and DNA backbones that accompany the photocatalytic cycle.

It is instructive to estimate the minimum power necessary for the proposed investigation of DNA photolyase. Consider an optimized time-resolved pump–probe experiment with parameters that match the Duke OK-4 FEL and synchrotron beamline. Using the synchrotron radiation as the probe with a single electron bunch in the storage ring ($f_{rep}=2.79$ MHz), our sensitivity is limited to $\Delta A_{IR,min}=0.001$. For a strong vibrational band, e.g., an amide or carboxylate, we have $\varepsilon_{IR}=600\ M^{-1}\,cm^{-1}$. If we optimize the optical system to provide a diffraction limited spot in the Bruker IFS-66v sample compartment then $w=50\ \mu$m. The power required decreases as the wavelength increases, so we will calculate the power necessary at the upper end of the OK-4 tuning range, $\lambda=400$ nm. Furthermore, we will allow the sample to absorb all available light. Actual samples will only absorb between 50% and 90% of incident light, and thus increase power needed. Under these conditions, we find a threshold power of 109 mW for an excitation wavelength of 400 nm (i.e., 40 nJ per pulse at 2.79 MHz). Several hundred milliwatts on the sample is a judicious target threshold given this idealized assessment. One option is to consider an experimental system with more intense absorption, where $600\ M^{-1}\,cm^{-1}$ is about as strong as vibrational bands get. Alternatively, electronic transitions can exhibit molar absorbtivities 100× greater. In fact, a HgCdTe semiconductor

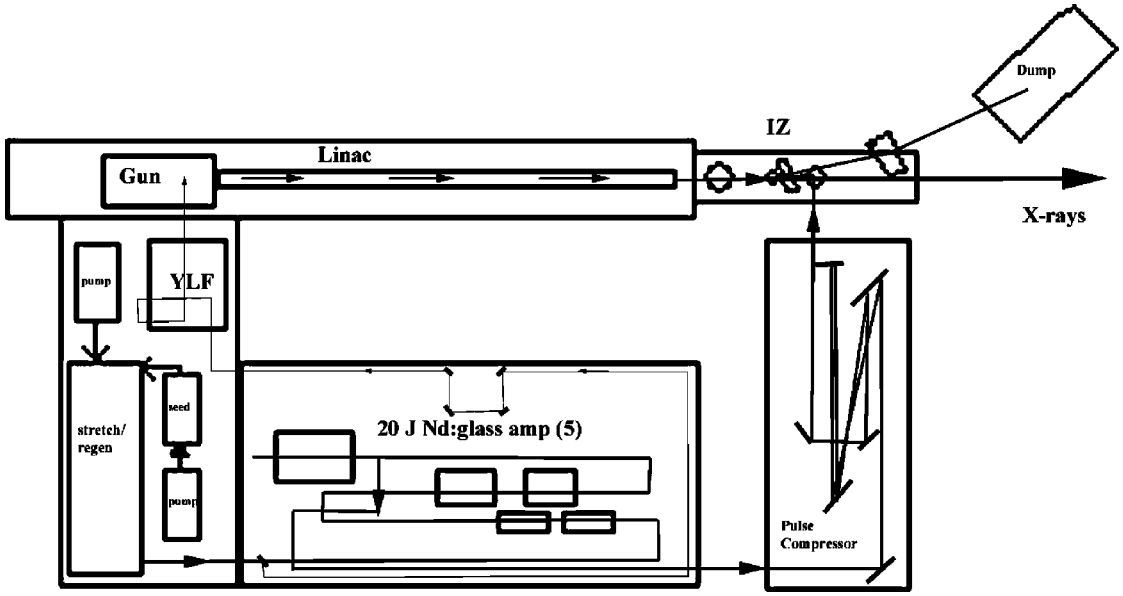

FIG. 44. Block diagram of the monochromatic x-ray source built and currently operating at the W. M. Keck FEL Center at Vanderbilt University. Gun—electron gun; linac—linear accelerator; IZ—interaction zone; Dump—electron beam dump; the tabletop terawatt laser consists of a pump, yttrium lithium fluoride, stretch/regen, seed, Nd:glass amplifier, and pulse compressor.

served as the experimental system for commissioning of the NSLS time-resolved IR beamline.[87]

XIII. IMAGING WITH PULSED, TUNABLE, MONOCHROMATIC X RAYS

Many individuals have long sought the means to produce pulsed, tunable, monochromatic x rays at high flux in a geometry suitable for human imaging, as well as for other purposes. While ''hard'' x rays are currently available from several sources, they have never before been available from a compact source that allows one to control the spectrum, timing, and flux of the x rays simultaneously.

The phenomenon of inverse Compton scattering lends itself well to the production of such a beam. In this process, a high-energy electron beam is tightly focused and counterpropagated against a powerful infrared laser beam. The IR photons scatter off the electrons and are shifted from the IR to x-ray frequencies in a direction almost collinear with the direction of travel of the electron beam. Since the Mark-III FEL produces a powerful IR beam and is driven by such an electron beam, it has shown promise as a vehicle for x-ray production using the Compton process.

In August 1998, the Mark-III FEL at Vanderbilt University successfully produced pulsed, tunable, near-monochromatic x rays.[92] That experiment yielded 10^4 x-ray photons/s, deemed impractical for the uses envisioned. The extreme radiation environment around the FEL, the loss of flux through a mosaic crystal transport system to an upstairs shirtsleeves imaging lab, the inaccessibility of the beamline components in a thick concrete shielded vault, the low number of photons per pulse, and the downwardly spiraling IR output of the FEL as electron beam parameters were optimized for the monochromatic beamline component of the x-ray source, all underscored the need for a better, more compact dedicated system.

To that end, a new monochromatic x-ray imaging system was designed and built. It consists of a rf linac running in ''single pulse'' mode, and a tabletop terawatt laser (Fig. 44). This source became operational in April 2001, and is currently used for applications research in pulsed, tunable, monochromatic x-ray imaging.

A. Monochromatic x-ray source

1. The accelerator

The electron gun is a copper photocathode, which is illuminated by a portion of the seed laser output (described below) that has been quadrupled. The linear accelerator is made of a single SLAC section driven by the 2856 MHz output of a standard klystron. Its energy can be tuned from 20 to 50 MeV. One superconducting solenoid magnet is used to focus the electron beam to a 50 μm spot at the interaction zone (IZ), which is defined as the point of interaction of the electron and IR beams.

2. The laser

The tabletop terawatt laser consists of a 200 fs Ti:sapphire seed laser running at 1052 nm which drives a combination stretcher/regenerative amplifier that produces a train of pulses stretched to about 1 ns, a Nd:YLF pulse compressor, and a frequency quadrupler that uses a small portion of light from the amplifier to drive the photocathode of the accelerator, with the rest of the light from the amplifier delivered to a multistage Nd:glass final amplifier to deliver 20 J of IR light to a pulse compressor and focusing optics. These in turn deliver the final 10 J pulse to the IZ. The current repetition rate of the laser is 0.01 Hz, limiting the x-ray pulses to one ''burst'' each 100 s.

3. The integrated x-ray source

The integrated x-ray source counter propagates a single 8 ps electron pulse containing 1 nC of charge and a single 8 ps 10 J pulse of 1052 nm IR light at the IZ to produce 10^{10} x-ray photons, tunable from 12 to 50 keV with a varying bandwidth of 1%–10%, also in 8 ps.

Alignment of the two beams is accomplished using conjoined perpendicular screens for serial visualization of the IR beam and transition radiation from the electron beam. Timing and phase adjustments bring the Rayleigh ranges of the two beams into an overlapping configuration at the IZ, making use of a newly developed phase corrector and an optical trombone. X-ray output emanates through a beryllium window on the end of the vacuum line. No x-ray optics are needed for deflection of the beam unless one desires to focus or deflect the beam for certain experiments. By altering the energy of the electron beam, the x-ray energy is made tunable. Focusing the electron beam to a smaller or larger focal spot size will vary the bandwidth. Since the machine is essentially self-shielded, it does not require the use of a concrete vault and may be run in an occupied room near personnel not required to wear radiation badges.

B. Medical applications

1. Mammography

Tunable, narrow bandwidth x rays can significantly reduce the radiation dose delivered to a patient in any type of x-ray procedure currently performed. This savings in radiation dose can vary by a factor of 2–50, depending on the study being performed and the imaging protocol being used.[93] An example of the utility of such a beam would be tunable, monochromatic x-ray mammography performed without breast compression to yield three-dimensional/volumetric CT images. Such studies would unravel the confusing overlap in structures now seen in plain film geometries. Diagnostic accuracy of this type of mammography should theoretically rise due to the higher linear attenuation characteristics of malignant tissues relative to normal breast structures.[94] An x-ray source, such as that described above, can be configured to service a large multiroom mammography facility.

Images of breast phantoms are currently being made with single 8 ps bursts of x rays, since each pulse contains more than enough photons to produce a complete image. Genetically engineered mice are also being imaged in an effort to discern the development of tumors of the breast over time and the potential for reversal of these growths using new types of drug therapy. The low radiation doses delivered using monochromatic x-ray beams allow the performance of longitudinal biological studies without ''frying'' the mouse with the high radiation doses now needed that utilize polychromatic beams.

2. K-edge imaging

K-edge imaging becomes possible with such a tunable beam as well. By tuning to the binding energy of the *k*-shell electron in a whole host of atoms, one can selectively enhance the visibility of currently used radiographic contrast agents, as well as tumor seeking drugs labeled with appropriate atoms within the 12–50 keV range of the beam. If one wished to lower the radiation dose to the patient even further, gadolinium containing magnetic resonance imaging contrast agents could be substituted for iodine containing ''dyes.'' The *k*-edge of iodine is 33 keV, while that of gadolinium is 50 keV. The human body is more transparent to the higher energy x-ray beam, but the *k*-edge effect can still be taken advantage of.

3. Phase contrast imaging

The x-ray output of the source is easily collimated, making it useful for the performance of phase contrast imaging. This type of imaging takes advantage of the inherent differences in refractive index of various body tissues and of diffractive edges at tissue planes. Because the body is made up of low atomic number elements, such as hydrogen, oxygen, carbon, and nitrogen, phase contrast effects (which are best seen in low *Z* elements) can offer as much as 100–1000 times the information than would be derived from such elements solely using the linear attenuation effects of standard absorption imaging.[95] This wealth of additional information offers some rather spectacular enhancements to images of animals, tissues, and potentially, it is hoped, humans. Tests using cancers in whole excised breasts have shown improvements in the conspicuity of some of the stellate fibrotic stranding around small tumors, making them more visible in the laboratory setting. In other words, the body reacts to many tumors by depositing fibrous tissue, which presents a characteristic starburst pattern in x-ray images. It is expected that this novel capability will be added to the clinical setting once some of the logistics of phase contrast imaging are worked out.[96]

4. Time-of-flight imaging

Since imaging fluxes are produced in 10 ps, time-of-flight imaging could be performed with this source. X-ray photons that traverse the imaged part without scattering are termed ballistic photons. These produce an image on a detector within picoseconds of the start of imaging. Scattered photons will not reach the detector before several hundred picoseconds, and can extend into the nanosecond regime. By using a detector that only records x rays for about 100 ps, one can ignore the delayed scattered photons. This affords one the opportunity of improving the signal-to-noise ratio in an image by six- to ninefold.[97] Alternatively, one could perform an image with the same S/N ratio with almost one order of magnitude fewer X rays.

5. Exceedingly high speed imaging

While an exceedingly high speed pulsed beam would be extremely useful in imaging rapid mechanical processes such as nondestructive testing of turbines, or explosive processes like the study of modes of armor failure with kinetic weapons, it can still find medical uses in the areas of small animal imaging or human imaging. Biological processes are exceedingly slow compared to the picosecond structure of the x-ray pulse. However, splitting the beam into a number of beams

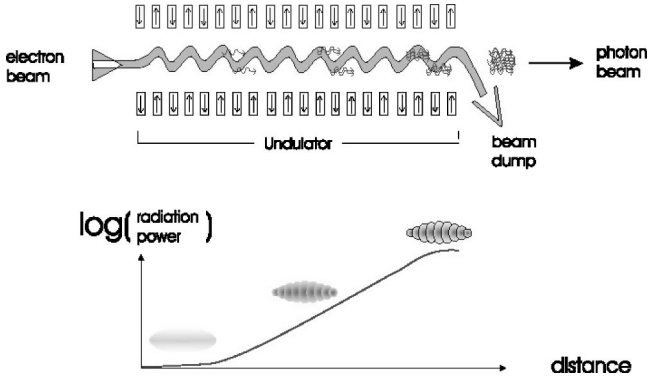

FIG. 45. Schematic diagram of a single pass FEL operating in SASE mode. The microbunching process that, develops in parallel with the radiation power is shown in the lower part. (Reproduced with permission from Ref. 104.)

and directing them through an animal from different directions at once opens the door to single pulse 10 ps CT. This would allow the study of these creatures without the necessity of anesthesia. Imaging equipment could be simplified, since gating studies to cardiac and respiratory cycles would no longer be needed. Tunable x rays would also cut the radiation dose needed to carry out these studies, so animals could be studied repeatedly over time to follow tumor growth, drug action, or other disease processes.

C. Protein crystallography

This integrated x-ray source can also be used to perform protein crystallography without the need to take protein crystals to synchrotron facilities. The beam can be focused to an exceptionally small spot and, when run in a high average power mode at 20 Hz, can deliver a photon flux only one to two orders of magnitude lower than that typically delivered to the crystal by the synchrotron source. Higher fluxes are available at synchrotrons but are frequently not used due to damage to the crystals. This device can deliver 8–50 keV with little modification at narrow bandwidth, making it possible to perform standard crystallography, multiwavelength anomalous dispersion (MAD), and Laue studies using multiple energies simultaneously.

D. Future prospects

While the current integrated x-ray source has been built to cover the x-ray spectrum from 12 to 50 keV, it is easily scalable to higher energies. The addition of a second SLAC section allows electron beam energies of 50–100 keV, and so on.

XIV. SASE FELS AND POTENTIAL APPLICATION TO BIOLOGY

A. Self-amplified spontaneous emission

When an electron bunch traverses an undulator (i.e., a periodic magnetic field), it emits electromagnetic radiation (Fig. 45) at wavelength $\lambda_r=\lambda_u\ (1+K^2/2)/2\gamma^2$, where λ_u is the undulator period, γmc^2 the electron beam energy, and K the dimensionless undulator strength parameter. Since the electrons are in a bunch much longer than the radiation

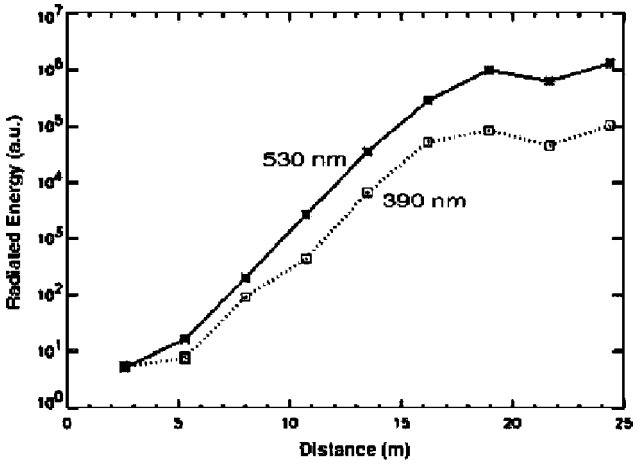

FIG. 46. Exponential gain and saturation of SASE FELs at wavelengths of 530 and 385 nm. The x axis shows the integrated radiated energy and the y axis the distance along the undulator system. (Reproduced with permission from Ref. 100.)

wavelength λ_r, the EM field emitted by different electrons has a random relative phase. The incoherent EM waves propagate through the undulator and interact with the electrons. The interaction makes the trajectory of electrons with larger (smaller) energy bend less (more) and the electrons within one radiation wavelength tend to get nearer to each other. This process produces microbunching of the electrons at the scale of λ_r. Electrons bunched within a wavelength emit coherent EM radiation, that is, the amplitude of the EM field is proportional to the number of electrons within the microbunch and the intensity proportional to the square of the electrons. The larger intensity leads to more microbunching. The result is that the EM field keeps gaining energy from the bunched electrons and the radiation intensity (I_r) grows exponentially with $I_r\sim e^{2z/L_G}$, where z is the undulator length. The gain length (L_G) is defined as $L_G=\lambda_u/(4\pi\sqrt{3}\rho)$, where ρ, the dimensionless FEL parameter, is of the order of 0.001 or less.[98] The radiation intensity eventually reaches saturation which occurs when the bunched electrons gain energy from the EM field balanced by losing energy to the EM field. The process, called self-amplified spontaneous emission,[98,99] is illustrated in Fig. 45. To observe the SASE process, a high quality and high bright-

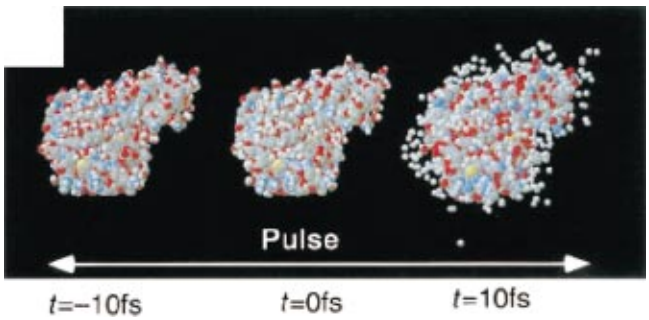

FIG. 47. (Color) Radiation damage to a lysozyme molecule as a function of time. The simulated x-ray FEL intensity was 3×1012 photons (12 keV) per 100 nm diam spot with the FWHM of the pulse 10 fs. The images show the molecule at the beginning, in the middle, and near the end of the x-ray pulse. (Reproduced with permission from Ref. 103.)

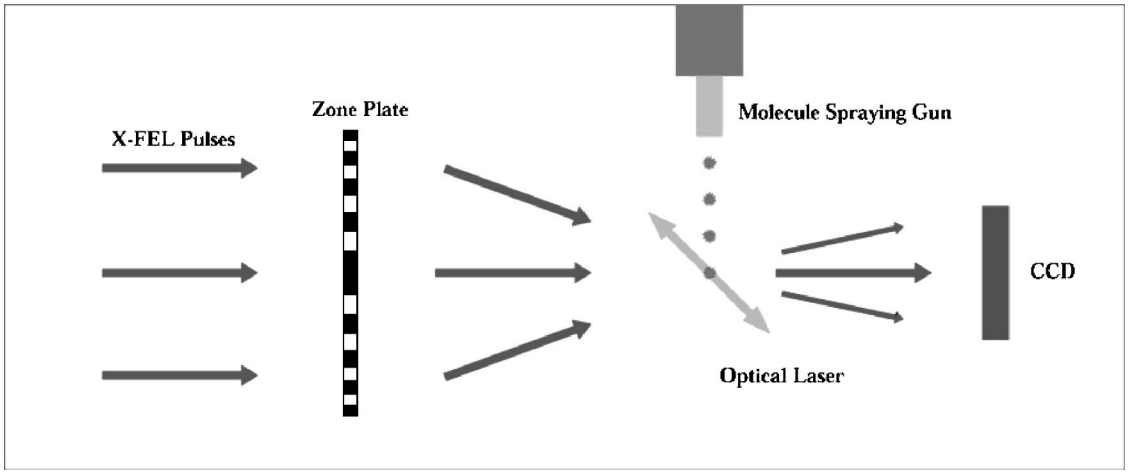

FIG. 48. Possible schematic layout for an experiment for imaging single biomolecules using x-ray FELs.

ness electron beam is required. With the development of photocathode radio-frequency electron guns and long, high quality undulators, SASE FELs operating at infrared, visible, and ultraviolet wavelengths were experimentally observed in the late 1990s.[100] More recently, a group at Argonne National Laboratory has demonstrated the exponential gain and saturation of SASE FELs at wavelengths of 530 and 385 nm (shown in Fig. 46),[101] and a group at Deutsche Elektronen Synchrotron (DESY), operating the TESLA test facility SASE FEL, has obtained exponential gain down to 80 nm, the shortest wavelength obtained up to now for a FEL.[102]

B. Future prospects

The demonstration of SASE FELs at visible and ultraviolet wavelengths paves the way for future x-ray FELs based on the SASE process. Tunable hard x-ray FELs have already been proposed worldwide including the Linac Coherent Light Source at the Stanford Linear Accelerator Center and TESLA at DESY.[103,104] Due to the extremely high flux and ultrashort pulses, x-ray FELs conceivably will open many new opportunities in biology and biomedical sciences. Here we illustrated one important application, i.e., the potential for imaging single biomolecules using x-ray FELs. Currently, x-ray crystallography is the primary methodology by which to determine the three-dimensional (3D) structure of protein molecules at near-atomic or atomic resolution, which requires obtaining sizable good quality protein crystals. However, somewhere around 20%–40% of protein molecules including most of the important membrane proteins are difficult or impossible to crystallize. One possible way to overcome the crystallization difficulty is to extend x-ray crystallography to noncrystals, which has recently been dem-

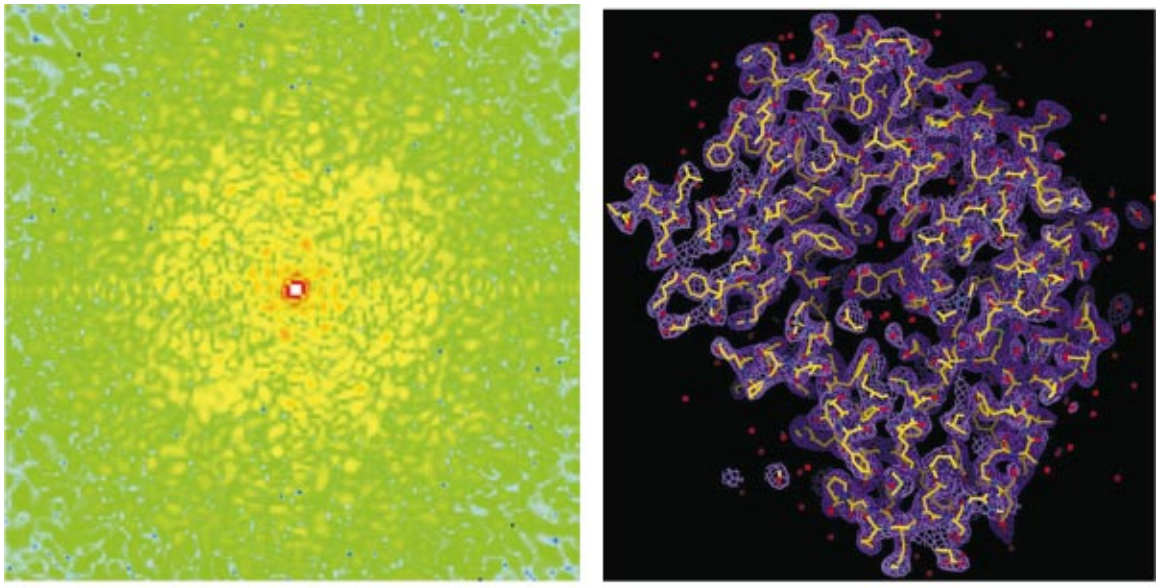

FIG. 49. (Color) (a) One section of a 3D diffraction pattern processed from 10^6 identical copies of rubisco molecules with Poisson noise added and $3\times3\times3$ center pixel intensity removed. The edge of the diffraction pattern corresponds to 2.5 Å resolution. (b) Stereoview of the reconstructed 3D electron density map of the rubisco molecule (contoured at 2σ) on which an atomic model obtained from the Protein Data Bank is superimposed. (Reproduced with permission from Ref. 110.)

onstrated by combining the coherent diffraction and the oversampling phasing method.[105] This novel approach can in principle be applied to imaging single biomolecules, but imposes very high radiation damage to biomolecules due to the loss of crystallinity. With the prospects for x-ray FELs, the radiation damage problem may be circumvented. Theoretical simulations show that, within about 10 fs, biomolecules can withstand x-ray intensity of $\sim 3.8\times 10^6$ photons/Å^2 with minimal structural change (as shown in Fig. 47).[106] In a combination of x-ray FELs and the novel approach of imaging noncrystalline specimens, a possible experimental setup is outlined here, shown in Fig. 48. X-ray FEL pulses will first be focused downward to a 100 nm spot by a Fresnel zone plate.[107] Using a mass spectrometer, identical biomolecules can be selected and sprayed one by one in random orientation into the focused spot.[108] Before scattering by a focused x-ray FEL pulse, each molecule will be orientated by a polarized nonresonant optical laser field.[109] The diffraction patterns will be recorded by an x-ray CCD with fast readout. The experiment will be carried out in high vacuum to eliminate unwanted scattering. Two-dimensional (2D) diffraction patterns from single molecules will be characterized and assembled into a 3D diffraction pattern. By employing the oversampling phasing method, it has been shown that a simulated 3D molecular diffraction pattern at 2.5 Å resolution can be successfully phased and transformed into an accurate electron density map comparable to that obtained by more conventional methods (Fig. 49).[110] The powerful combination of the x-ray FEL and the new imaging approach could therefore have a tremendous impact on structural biology.

XV. DISCUSSION

A wide range of biophysical and biomedical applications research has been accomplished by taking advantage of the unique light source capabilities of FELs. These capabilities include combinations of wavelength ranges, pulse structures, and peak and average power. A broad research and development program resulted in human surgical applications using the midinfrared Mark-III FEL. The operating parameters for an IR laser dedicated to surgical applications were specified. The inhomogeneous buildup of heat that is key to controlled degradation of material components seen in tissue ablation and mass spectrometry can confound spectroscopic measurements with infrared, linac-based FELs. A microbeam for investigating tissue dynamics using multiple light sources holds the promise of understanding at cellular length scales, i.e., a molecular description of cell physiology and biomedical processes.

The midinfrared SCA FEL and UV FELs based on storage rings are particularly useful for one- and two-color spectroscopic investigations of biophysical processes. These FELs enable spectroscopic techniques that access novel wavelength and dynamic ranges not probed by complementary techniques using conventional ultrafast lasers. While the repetition rates of these FELs are high enough to support novel sampling techniques and keep the measurement times manageable, they are low enough to limit the confounding effects of sample heating.

The THz-BRIDGE project currently supported by the European Union includes the development of compact FEL technology operating in the THz (far-infrared) range. The goals for applications of these THz sources include biological and diagnostic biomedical imaging.[111]

A source for pulsed, tunable, monochromatic x-rays produced by inverse Compton scattering is now operational, having benefited from a proof-of-principle demonstration using the midinfrared Mark-III FEL. This source should enable novel protocols in medical imaging as well as serve as a compact source for studies of time-resolved structural biology. Furthermore, the next generation SASE light source promises extremely high flux and ultrashort pulses and conceivably will open many new opportunities in biological and biomedical science.

[1] H. Motz *et al.*, J. Appl. Phys. **24**, 826 (1953); J. M. J. Madey, *ibid.* **42**, 1906 (1971); V. L. Granatstein *et al.*, Appl. Phys. Lett. **30**, 384 (1977).

[2] C. A. Brau, Science **239**, 1115 (1988); *Free-Electron Lasers* (Academic, Boston, 1990); H. P. Freund and T. M. Antonsen, Jr., *Principles of Free-Electron Lasers*, 2nd ed. (Chapman & Hall, London, 1996); P. O. Shea and H. P. Freund, Science **292**, 1853 (2001).

[3] W. B. Colson, E. D. Johnson, M. J. Kelley, and H. A. Schwettman, Phys. Today **55**, 35 (2002) and references therein; National Research Council, *Report of the Committee on Free Electron Lasers* (National Academy, Washington, DC, 1994).

[4] R. Srinivasan, Science **234**, 559 (1986); IEEE J. Quantum Electron. **QE-20**, 1342 (1984); C. A. Puliafito, R. F. Steinert, and T. F. Duetsch, Ophthalmology **92**, 741 (1985); R. V. Jeffreys, in *Lasers in Neurosurgery*, edited by R. V. Jeffreys (Wiley–Liss, 1992), p. 79.

[5] R. R. Anderson and J. A. Parrish, Science **220**, 524 (1983); M. L. Wolbarsht, IEEE J. Quantum Electron. **QE-20**, 1427 (1984); D. Stern, C. A. Puliafito, E. T. Dobi, and W. T. Reidy, Ophthalmology **95**, 1434 (1988); J. T. Walsh, T. J. Flotte, and T. F. Deutsch, Lasers Surg. Med. **9**, 314 (1989); B. Zysset, J. G. Fujimoto, C. A. Puliafito, C. A. Birngruber, and T. F. Deutsch, *ibid.* **9**, 193 (1989).

[6] C. A. Brau and M. H. Mendenhall, Nucl. Instrum. Methods Phys. Res. A **331**, ABS4 (1993).

[7] G. S. Edwards, B. Johnson, J. Kozub, J. Tribble, and K. Wagner, Opt. Eng. (Bellingham) **32**, 314 (1993).

[8] G. Edwards *et al.*, Nature (London) **371**, 416 (1994).

[9] G. M. Peavy, L. Reinisch, J. T. Payne, and V. Venugopalan, Lasers Surg. Med. **25**, 421 (1999); J. T. Payne, G. M. Peavy, L. Reinisch, and D. C. Van Sickle, *ibid.* **29**, 38 (2001).

[10] M. Ostertag, R. Walker, H. Weber, A. F. G. van der Meer, J. McKinley, N. Tolk, and B. Jean, Proc. SPIE **2672**, 181 (1996); E. J. Swift, Jr., G. S. Edwards, J. Perdigao, J. Y. Thompson, M. F. Nunes, D. E. Ruddell, and A. Negishi, J. Dent. **29**, 347 (2001).

[11] M. Speyer, J. Joe, J. M. Davidson, R. H. Ossoff, and L. Reinisch, Laryngoscope **106**, 845 (1996); B. Jean, Nucl. Instrum. Methods Phys. Res. A **393**, 540 (1997); G. L. Bryant, Jr., C. F. Lano, Jr., L. Reinisch *et al.*, Ann. Otol. Rhinol. Laryngol. **107**, 269 (1998); G. L. Bryant, J. M. Davidson, R. H. Ossoff *et al.*, Laryngoscope **108**, 13 (1998); D. S. Fortune, S. Huang, G. L. Bryant *et al.*, in *Lasers in Surgery: Advanced Characterization, Therapeutics, and Systems VIII*, edited by R. R. Anderson (1998), BIOS/SPIE Vol. 3245, pp. 191–199; K. Awazu, A. Nagai, T. Tomimasu *et al.*, Nucl. Instrum. Methods Phys. Res. B **144**, 255 (1998); D. L. Ellis, N. K. Weisberg, J. S. Chen *et al.*, Lasers Surg. Med. **25**, 1 (1999); S. R. Uhlhorn, S. Harrison, H. S. Pratisto *et al.*, in *Laser–Tissue Interaction X*, edited by S. L. Jacques (1999), BIOS/SPIE Vol. 3601, p. 3601.

[12] K. Becker, J. B. Johnson, and G. Edwards, Rev. Sci. Instrum. **65**, 1496 (1994).

[13] J. Tribble, D. Lamb, L. Reinisch, and G. Edwards, Phys. Rev. E **55**, 7385 (1997).

[14] J. Auerhammer, R. Walker, A. F. G. van der Meer, B. Jean, Book of Abstracts, 18th FEL Conference and 3rd FEL User Workshop, Rome, 1996.

[15] E. Sobol, A. Sviridov, M. Kitai, J. Gilligan, N. Tolk, and G. Edwards, J. Biomed. Opt. **8**, 216 (2003).
[16] G. S. Edwards, M. S. Hutson, S. Hauger, J. Kozub, J. Shen, C. Shieh, K. Topadze, and K. Joos, Proc. SPIE **4633**, 194 (2002).
[17] M. S. Hutson, S. A. Hauger, and G. Edwards, Phys. Rev. E **65**, 061906 (2002).
[18] D. C. Lamb, L. Reinisch, J. Tribble, R. H. Ossoff, T. J. Flotte, and A. G. Doukas, Proc. SPIE **2391**, 192 (1995).
[19] G. Edwards, Opt. Eng. (Bellingham) **34**, 1524 (1995).
[20] G. Edwards *et al.*, IEEE J. Quantum Electron. **QE-2**, 810 (1996).
[21] S. Grafström *et al.*, Opt. Commun. **65**, 121 (1988).
[22] H. S. Pratisto *et al.*, in *Specialty Fiber Optics for Medical Applications*, edited by A. Katzir and J. A. Harrington (1999), BIOS/SPIE Vol. 3596, p. 55.
[23] I. Gannot, A. Inberg, M. Oksman *et al.*, IEEE J. Quantum Electron. **QE-2**, 880 (1996); I. Gannot *et al.*, Appl. Opt. **36**, 6289 (1997).
[24] H. S. Pratisto, S. R. Uhlhorn, and E. D. Jansen, Fiber Integr. Opt. **20**, 83 (2000).
[25] Y. Matsuura, T. Abel, and J. A. Harrington, Appl. Opt. **34**, 6842 (1995); Y. Matsuura *et al.*, Electron. Lett. **32**, 1096 (1996).
[26] Y. Matsuura, K. Matsuura, and J. A. Harrington, Appl. Opt. **35**, 5395 (1996).
[27] G. P. Cram and M. L. Copeland, Nucl. Instrum. Methods Phys. Res. B **144**, 256 (1998).
[28] M. L. Copeland, R. J. Maciunas, and G. S. Edwards, *Use of the Free-Electron Laser for Metastatic Brain Tumors in Neurosurgical Topics: Advanced Techniques in Central Nervous System Metastases*, edited by R. J. Maciunas (The American Association of Neurological Surgeons, Park Ridge, II 1998), p. 113.
[29] J. E. Boggan *et al.*, Neurosurgery **11**, 609 (1982); J. E. Boggan, in *Lasers in Neurosurgery*, Ref. 10, p. 21.
[30] J. H. Shen, J. A. Harrington, G. S. Edwards, and K. M. Joos, Appl. Opt. **40**, 583 (2001).
[31] K. Matsuura, Y. Matsuura, and J. A. Harrington, Opt. Eng. (Bellingham) , 3418 (1996).
[32] E. A. J. Marcatili and R. A. Schmeltzer, Bell Syst. Tech. J. **43**, 1783 (1964).
[33] M. Miyagi and S. Karasawa, Appl. Opt. **29**, 367 (1990).
[34] J. J. Corbet, J. A. Nerad, D. T. Tse, and R. L. Anderson, Arch. Ophthalmol. (Chicago) **106**, 1391 (1988).
[35] K. M. Joos, J. H. Shen, D. J. Shetlar, and V. A. Casagrande, Lasers Surg. Med. **27**, 191 (2000).
[36] K. M. Joos, J. H. Shen, G. S. Edwards, D. J. Shetlar, J. Khoury, and R. D. Robinson, Invest. Ophthalmol. Visual Sci. **37**, S431 (1996).
[37] D. R. Anderson, Trans. Am. Ophthalmol. Soc. **79**, 458 (1981).
[38] W. Sun, J. H. Shen, D. J. Shetlar, and K. M. Joos, J. Glaucoma **9**, 325 (2000).
[39] C. A. Puliafito, R. F. Steinert, T. F. Deutsch, F. Hillenkamp, E. J. Dehm, and C. M. Alder, Ophthalmology **92**, 741 (1985).
[40] J. P. Cummings and J. T. Walsh, Jr., Appl. Phys. Lett. **62**, 1988 (1993).
[41] B. A. Hooper, C. Lin, Y. Domankevitz, and R. R. Anderson, *Therapeutic Laser Applications, Technical Digest* (Optical Society of America, Washington, DC, 1998), p. 41.
[42] B. A. Hooper, Y. Domankevitz, C. Lin, and R. R. Anderson, Appl. Opt. **38**, 5511 (1999).
[43] A. J. Welch, M. Motamedi, S. Rastegar, G. L. Le Carpentier, and E. D. Jansen, Photochem. Photobiol. **53**, 815 (1991).
[44] E. D. Jansen, T. G. van Leeuwen, M. Motamedi, C. Borst, and A. J. Welch, J. Appl. Phys. **78**, 564 (1995).
[45] J. T. Walsh, Jr., T. H. Flotte, R. R. Anderson, and T. F. Deutsch, Lasers Surg. Med. **8**, 108 (1988).
[46] E. Hecht and A. Zajac, *Optics* (Addison–Wesley, Reading, MA, 1974), p. 81.
[47] F. Mirabella, *Internal Reflection Spectroscopy*, Practical Spectroscopy Series, Vol. 15 (Dekker, New York, 1992).
[48] R. Simhi, Y. Gotshal, D. Bunimovich, A. Sela, and A. Katzir, Appl. Opt. **39**, 3421 (1996); for near-field imaging with an IR FEL see, for example, M. K. Hong, A. Jeung, P. Huie, and S. Erramilli, Proc. SPIE **3153**, 115 (1996).
[49] H. D. Downing and D. Williams, J. Geophys. Res. **80**, 1656 (1975); G. M. Hale and M. R. Querry, Appl. Opt. **12**, 555 (1973).
[50] B. A. Hooper, C. Lin, Y. Domankevitz, and R. R. Anderson, Appl. Phys. Lett. **78**, 2381 (2001).
[51] B. A. Hooper, G. C. LaVerde, and O. T. von Ramm, Nucl. Instrum. Methods Phys. Res. A **475**, 645 (2001).
[52] P. E. Young, A. M. Richman, A. S. Ketchum, and D. P. Kiehart, Genes Dev. **7**, 29 (1993); F. Agnes and S. Noselli, C R. Acad. Sci. III **322**, 5 (1999); A. Jacinto, S. Woolner, and P. Martin, Devel. Cell **3**, 9 (2002); N. Harden, M. Ricos, Y. M. Ong, W. Chia, and L. Lim, J. Cell. Sci. **112**, 273 (1999); Q. J. Li, T. M. Pazdera, and J. S. Minden, Development (Cambridge, U.K.) **126**, 2299 (1999); H. Liu, Y. C. Su, E. Becker, J. Treisman, and E. Y. Skolnik, Curr. Biol. **9**, 101 (1999); Y. Lu and J. Settleman, Genes Dev. **13**, 1168 (1999); M. G. Ricos, N. Harden, K. P. Sem, L. Lim, and W. Chia, J. Cell. Sci. **112**, 1225 (1999); K. Sawamoto *et al.*, J. Cell Biol. **146**, 361 (1999); V. Zecchini, K. Brennan, and A. Martinez-Arias, Curr. Biol. **9**, 460 (1999).
[53] M. W. Berns *et al.*, Science **213**, 507 (1981).
[54] D. P. Kiehart, C. G. Galbraith, K. A. Edwards, W. L. Rickoll, and R. A. Montague, J. Cell Biol. **149**, 471 (2000).
[55] M. S. Hutson, Y. Tokutake, M.-S. Chang, J. W. Bloor, S. Venakides, D. P. Kiehart, and G. S. Edwards, Science **300**, 145 (2003).
[56] M. C. Halloran, M. Sato-Maeda, J. T. Warren, F. Y. Su, Z. Lele, P. H. Krone, J. Y. Kuwada, and W. Shoji, Development (Cambridge, U.K.) **127**, 1953 (2000).
[57] A. E. Jeung, P. Huie, S. Erramilli, M. K. Hong, and H. A. Schwettmann, in Ref. 14.
[58] *Handbook of Biological Confocal Microscopy*, edited by J. B. Pawley (Plenum, New York, 1990).
[59] IMAGEJ, Ver. 1.24 (available for free at http://rsb.info.nih.gov/ij/).
[60] For a broad overview of the state of the art, see for example, Chem. Rev. (Washington, D.C.) **209–606**, 101 (2001).
[61] J. B. Fenn, M. Mann, C. K. Meng, S. F. Wong, and C. M. Whitehouse, Science **246**, 64 (1989).
[62] M. Karas, D. Bachmann, U. Bahr, and F. Hillenkamp, Int. J. Mass Spectrom. Ion Processes **78**, 53 (1987).
[63] R. Cramer, R. F. Haglund, Jr., and F. Hillenkamp, Int. J. Mass Spectrom. Ion Processes **169/170**, 51 (1997).
[64] M. R. Papantonakis, J. Kim, W. P. Hess, and R. F. Haglund, Jr., J. Mass Spectrom. **37**, 639 (2002).
[65] R. Cramer, K. Becker, R. F. Haglund, Jr., and F. Hillenkamp, J. Am. Soc. Mass Spectrom. **7**, 1187 (1996).
[66] For a review of time-of-flight mass spectrometry instrumentation, see, for example, A. Vertes, R. Gijbels, and F. Adams, *Laser Ionization Mass Analysis*, Chemical Analysis series Vol. 124 (Wiley, New York, 1993).
[67] M. L. Baltz-Knorr, D. R. Ermer, K. E. Schriver, and R. F. Haglund, Jr., J. Mass Spectrom. **37**, 254 (2002).
[68] M. L. Baltz-Knorr, K. E. Schriver, and R. F. Haglund, Jr., Appl. Surf. Sci. **197/198C**, 19 (2002).
[69] See, for example, S. Berkenkamp, F. Kirpekar, and F. Hillenkamp, Science **281**, 260 (1998).
[70] C. Menzel, K. Dreisewerd, S. Berkenkamp, and F. Hillenkamp, Int. J. Mass. Spectrom. **207**, 73 (2001); Z. Knochenmuss, R. Knochenmuss, and R. Knochenmuss, Mass Spectrom. Rev. **17**, 337 (1998).
[71] D. R. Ermer, M. Baltz-Knorr, and R. F. Haglund, Jr., J. Mass Spectrom. **36**, 538 (2001).
[72] A. Xie, A. van der Meer, W. Hoff, and R. H. Austin, Phys. Rev. Lett. **84**, 5435 (2000).
[73] A. Xie, A. van der Meer, and R. H. Austin, Phys. Rev. Lett. **88**, 018102 (2002).
[74] D. Dlott and M. Fayer, J. Opt. Soc. Am. B **6**, 977 (1989); R. H. Austin, M. W. Roberson, and P. Mansky, Phys. Rev. Lett. **62**, 1912 (1989).
[75] R. H. Austin and A. Xie, Nucl. Instrum. Methods Phys. Res. A, 504 (1998).
[76] D. J. Segelstein, M.S. thesis, University of Missouri–Kansas City, Kansas City, MO, 1981; a plot of these data can be found at http://omlc.ogi.edu/spectra/water/gif/segelstein81.gif.
[77] M. E. Couprie, G. De Ninno, G. Moneron, D. Nutarelli, M. Hirsch, D. Garzella, E. Renault, R. Roux, and C. Thomas, Nucl. Instrum. Methods Phys. Res. A **475**, 617 (2001).
[78] M. E. Couprie, P. Tauc, F. Merola, A. Delboulbé, D. Garzella, T. Hara, and M. Billardon, Rev. Sci. Instrum. **65**, 1485 (1994).
[79] E. Renault, L. Nahon, D. Nutarelli, D. Garzella, M. E. Couprie, and F. Mérola, Proc. SPIE **3925**, 29 (2000); E. Renault, L. Nahon, D. Garzella, D. Nutarelli, G. De Ninno, M. Hirsch, and M. E. Couprie, Nucl. Instrum. Methods Phys. Res. A **475**, 617 (2001).
[80] T. G. Scott, R. D. Spencer, N. J. Leonard, and G. Weber, J. Am. Chem. Soc. **92**, 687 (1970); A. J. W. G. Visser and A. van Hoek, Photochem.

Photobiol. **33**, 35 (1981); G. Krishnamoorthy, N. Periasamy, and B. Venkataraman, Biochem. Biophys. Res. Commun. **144**, 387 (1987); A. Gafni and L. Brand, Biochemistry **15**, 3165 (1976); D. W. Miles and D. W. Urry, J. Biol. Chem. **243**, 4181 (1968).
[81] O. Jardetzky and N. G. Wade-Jardetzky, J. Biol. Chem. **241**, 85 (1966).
[82] S. L. Shapiro and K. R. Winn, J. Chem. Phys. **73**, 5958 (1980).
[83] R. P. Haugland, *Handbook of Fluorescent Probes* (Molecular Probes, Eugene, OR 1996).
[84] M. F. Goodman, Nature (London) **378**, 237 (1995); A. Douhal, S. K. Kim, and A. H. Zewail, *ibid.* **378**, 260 (1995).
[85] V. N. Litvinenko, S. H. Park, I. V. Pinayev, and Y. Wu, Nucl. Instrum. Methods Phys. Res. A **470**, 66 (2001).
[86] M. S. Hutson, R. A. Palmer, A. Gillikin, M.-S. Chang, V. N. Litvinenko, and G. S. Edwards, Proc. SPIE **4633**, 225 (2002).
[87] G. L. Carr, R. P. S. M. Lobo, C. J. Hirschmugl, J. LaVeigne, D. H. Reitze, and D. B. Tanner, Proc. SPIE **3153**, 80 (1997); R. P. S. M. Lobo, J. LaVeigne, D. H. Reitze, D. B. Tanner, and G. L. Carr, Rev. Sci. Instrum. **70**, 2899 (1999).
[88] A. H. Lumpkin, B. X. Yang, V. Litvinenko, B. Burnham, S. Park, P. Wang, and Y. Wu, Nucl. Instrum. Methods Phys. Res. A **47**, 338 (1998).
[89] K. Masutani, H. Sugisawa, A. Yokota, Y. Furukawa, and M. Tasumi, Appl. Spectrosc. **46**, 560 (1992).
[90] A. Sancar, Biochemistry **33**, 2 (1994).
[91] T. Okamura, A. Sancar, P. F. Heelis, T. P. Begley, Y. Hirata, and N. J. Mataga, J. Am. Chem. Soc. **113**, 3143 (1991).
[92] F. E. Carroll, J. W. Waters, R. H. Traeger *et al.*, Proc. SPIE **3614**, 139 (1999).
[93] J. M. Boone, Radiology **213**, 23 (1999).
[94] P. C. Johns and M. J. Yaffe, Phys. Med. Biol. **32**, 675 (1987); F. E. Carroll, J. W. Waters, W. W. Andrews *et al.*, Invest. Radiol. **29**, 266 (1994).
[95] T. Takeda, A. Momose, and Y. Itai *et al.*, Acad. Radiol. **2**, 799 (1995).
[96] D. Chapman, W. Thomlinson, R. E. Johnston *et al.*, Phys. Med. Biol. **42**, 2015 (1997).
[97] C. L. Gordon, Y. Yin, B. E. Lemof *et al.*, Opt. Lett. **20**, 9 (1995).
[98] R. Bonifacio, C. Pellegrini, and L. M. Narducci, Opt. Commun. **50**, 373 (1984).
[99] M. Kondratenko and E. L. Saldin, Sov. Phys. Dokl. **24**, 986 (1979).
[100] M. J. Hogan *et al.*, Phys. Rev. Lett. **81**, 4867 (1998); M. Babzien *et al.*, Phys. Rev. E **57**, 6093 (1998); S. V. Milton *et al.*, Phys. Rev. Lett. **85**, 988 (2000).
[101] S. V. Milton *et al.*, Science **292**, 2037 (2001).
[102] J. Andruszkow *et al.*, Phys. Rev. Lett. **85**, 3825 (2000).
[103] M. Cornacchia *et al.*, Report SLAC-R-521, Stanford Linear Accelerator Center, Stanford, CA (1998).
[104] DESY Report DESY97-048, edited by R. Brinkmann, G. Materlik, J. Rossbach, and A. Wagner, Deutsches Elektronen Synchrotron, Hamburg (1997).
[105] J. Miao, P. Charalambous, J. Kirz, and D. Sayre, Nature (London) **400**, 342 (1999).
[106] R. Neutze, R. Wouts, D. Spoel, E. Weckert, and J. Hajdu, Nature (London) **406**, 752 (2000).
[107] R. Tatchyn, LCLS Optics: Technological Issues and Scientific Opportunities in Proceedings of the Workshop on Scientific Applications of Short Wavelength Coherent Light Sources, SLAC, Stanford, 1993.
[108] M. A. Tito, K. Tars, K. Valegard, J. Hajdu, and C. V. Robinson, J. Am. Chem. Soc. **122**, 3550 (2000).
[109] J. J. Larsen, K. Hald, N. Bjerre, H. Stapelfeldt, and T. Seideman, Phys. Rev. Lett. **85**, 2470 (2000).
[110] J. Miao, K. Hodgson, and D. Sayre, Proceedings of the National Academy of Sciences 98, 6641 (2001).
[111] Proceedings of the THz-Bridge Workshop, Capri, 2002, J. Biol. Phys. (to be published).
[112] C. Abad-Zapatero, J. P. Griffith, J. L. Sussman, and M. G. Rossmann, J. Mol. Biol. **198**, 445 (1987), entry 1LDM of the Protein Data Bank.